FABRICATION AND MODELING OF FUNCTIONALLY GRADED POROUS POLYMER MATERIALS

A Dissertation

by

YING ZHANG

Submitted to the Office of Graduate and Professional Studies of
Texas A&M University
in partial fulfillment of the requirements for the degree of

DOCTOR OF PHILOSOPHY

Chair of Committee,	Jyhwen Wang
Committee Members,	Terry Creasy
	Hong Liang
	Bruce Tai
Head of Department,	Andreas A. Polycarpou

August 2016

Major Subject: Mechanical Engineering

ABSTRACT

Functionally graded porous materials (FGPMs) are porous materials with porosity gradient distributed over the volume. They have many applications in aerospace, biomedical, and other engineering fields. Despite a lot of effort being made to fabricate FGPMs, the manufacturing processes are either complex, expensive, unable to control exact porosity distribution, or unable to create closed cell structures.

This work presents a new approach to manufacturing polymer FGPMs with both closed cell and open cell structures using the thermo-bonding lamination process. Under applied compressive load, controlled heating temperature, and appropriate holding time, it was shown that this thermally-induced bonding technique can bond layers of polymer sheets to create porous three-dimensional objects. An investigation on effects of different factors on the bonding shear strength was performed. It was found that the bonding shear strength can be controlled by properly setting the pressure, temperature, and time.

The fabricated FGPMs specimens with different porosity configurations were characterized using the compression test in the normal direction and transverse direction, and the effective moduli were obtained.

An analytical model for predicting the elastic properties of the FGPMs was derived. The model is based on Mori-Tanaka's approach while extended to *graded* and *porous* cases. A more generalized case – the polynomial varying strain field – was assumed and the Eshelby's tensor for polynomial varying eigenstrain was obtained to facilitate the derivation. In addition, an analytical model for FGPMs with open cell structure was also developed. A solution to the overall eigenstrain of the interconnected voids was provided by considering the disturbed stress field outside of the voids. It was shown that the models can accurately predict the mechanical response of closed cell and open cell FGPMs.

Numerical model based on representative volume element (RVE) with the periodic boundary condition applied was also developed for FGPMs to investigate the mechanical response of the material and to obtain the corresponding effective modulus. It was shown that the results from the numerical model agree well with experimental and analytical results, indicating that the developed model can predict the material response accurately.

In summary, the developed fabrication technique is an effective method to produce 3-D graded porous objects for practical applications. The proposed analytical and numerical models can be adopted directly by researchers in the fields of micromechanics and mechanics of composite.

DEDICATION

To my family

ACKNOWLEDGEMENTS

I would like to gratefully acknowledge my supervisor, Dr. Jyhwen Wang, for his great advices, guidance, and continual support throughout my Ph. D study. I would also like to thank my committee members, Dr. Creasy, Dr. Liang, and Dr. Tai, for their guidance and support throughout the course of this research.

I would like to express warm thanks to Dr. Fang for providing CARVER hydraulic heating compression machine. I am very grateful to all the workshop staff at Mechanical Engineering 3D printing lab and Materials and Structures lab. In particular, I would like to thank Rodney and Troy for their technical advices. Thanks also go to my friends and colleagues and the department faculty and staff for making my time at Texas A&M University a great experience.

Finally, thanks to my mother, father, and sister for their encouragement, support and love.

TABLE OF CONTENTS

Page

LIST OF FIGURES

Page

LIST OF TABLES

Page

1. INTRODUCTION

1.1 Overview

Functionally graded materials (FGMs) are composite materials which consist of two or more compositions with the variation in compositions or structures gradually over volume. As such, their material properties are also gradually changed over volume [1]. FGMs have received extensive attention since they possess a number of advantages. For example, FGMs can be designed and fabricated for specific applications due to their certain desired features of each individual phases [2]. i.e. the aerospace and aircraft industry is interested in the material's capability of withstanding high thermal gradient, which can be achieved by using one layer of ceramic and one layer of metal material. The materials are widely used in aviation and aerospace, optoelectronic, and energy applications.

Functionally graded porous materials (FGPMs) can be considered as hollow members, which have also been extensively investigated due to their wide applications in space, biomedical, and aeronautical engineering [3]. In the FGPMs, the pores are distributed throughout the material with the variation in porosity over volume. The variation of porosity may be due to the density change of pores as shown in Figure 1.1 or

the size change of pores as shown in Figure 1.2 or both. The weight of FGPMs are reduced with the involvement of pores compared to non-FGPMs. In addition, the gradual change of porosity can impart desirable properties such as excellent damping capacity and the ability to withstand high thermal gradient [4]. The nature FGPMs include bamboo with density gradients along radial direction in its cross section [5], human cancellous bone which is sponge-like cellular structure [6], banana peel [7], and elk antler [8], etc. Other FGPMs, such as biomedical implants [9, 10], cushioning materials [11], filtration material, drug delivery device [12], and permeable interlocking pavement, etc, are also widely used in industries and daily lives.

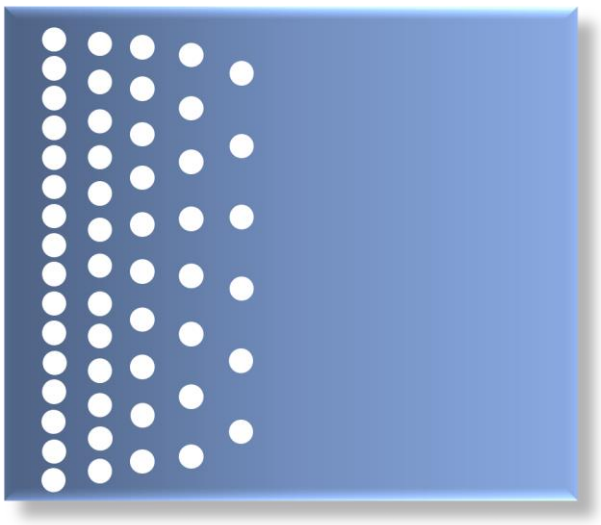

Figure 1. 1 FGPMs with density of pores changed [6]

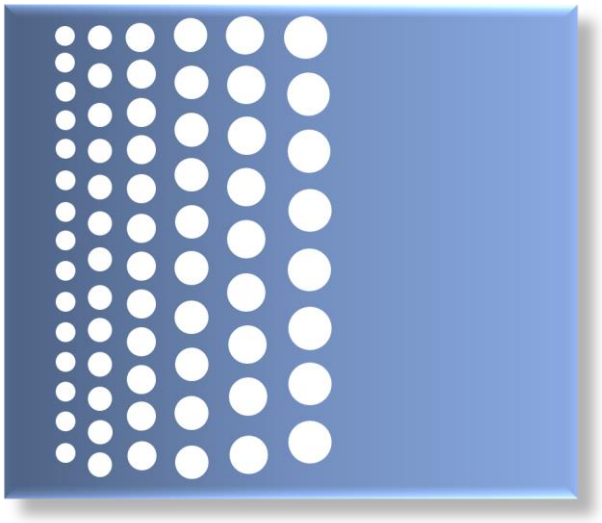

Figure 1. 2 FGPMs with pores size changed [6]

Depending on the pore structures, porous materials can be divided into open cell and closed cell structures. In open cell porous materials, the pores are interconnected, while in closed cell structures, each pore is enclosed and isolated by the base material. Significant efforts in the past have been made to fabricate porous materials. For open cell porous metal, powder sintering [13], space holder method [14], replication [15], and plasma spraying are the common manufacturing methods. In order to fabricate functionally graded material, electro discharge compaction approach has been used [16]. Closed cell structures are commonly processed by random foaming processes, with the dimension, shape, and locations of pores are affected by the processing parameters [17]. Closed cell graded porous metal material can also be fabricated by gas injection or

foaming agents injection into the molten metals in order to introduce “gradient” [18]. Plasma spraying is another alternative approach to manufacture closed cell FGPMs. A variety of processing techniques were used to fabricate polymer porous materials, including particulate leaching [19, 20], thermally induced phase separation[15, 21], supercritical fluid-gassing [22], solvent-free process [23], and solvent/non-solvent sintering [24] . These methods are relatively complicated since they require either molds or foaming agents. More importantly, the exact pore size, overall porosity, and the gradient are hard to control.

Another approach to fabricating FGPMs is to use Additive Manufacturing (AM) techniques. In recent years, AM becomes a popular technology that have received extensive attention. The AM processes are able to produce almost any freeform parts using .stl file format as the geometric input [25]. They can also be used to fabricate porous materials for aerospace, electronics, and biomedical applications. While common AM processes such as Fused Deposition Modeling (FDM) [10], Selective Laser Sintering (SLS) [12, 26], , Stereolithography (SLA) [27, 28], freeze form extrusion fabrication [29] have been used to produce porous materials, supporting material is needed in order to create the porous structures. For example, FDM processes adopt supporting materials to fill in the empty space during part fabrications. An additional operation is required to remove the support material after the process. For printed parts

with small pores, e.g. a few hundred microns, it would take laborious effort to remove the supporting material.

Another approach to deal with supporting material issue is to selectively fuse liquid or powder material layer by layer [30], such as SLA and SLS processes. While removing liquid or powder is not a concern for creating open cell porous structures, for closed cell porous structure, the base material, liquid or powder, is trapped inside the pore and cannot be removed after the fabrication process. It was also reported that some supporting materials might be hazardous during use and disposal since harmful chemicals might be involved, e.g. some thermoplastic acrylic polymers consist of phenyl phosphates which are toxic [31]. Furthermore, comparing to the base material usage for part fabrication, supporting material consumption could be greater in volume and in cost, which would also result in longer part construction time and high costs.

An alternative to the aforementioned AM technique for manufacturing porous materials of both closed cell and open cell structure without support material is lamination. With lamination, objects are fabricated in multiple layers, and the process is generally achieved by welding, adhesive bonding or thermal bonding. Lamination technology has been used in automotive, aerospace, appliances, medical and hygiene, constructions, electronics, and pharmaceutical. It can be also used in manufacturing molding tools [32, 33] and solar cell panels. Typically, adhesives alone or in combined

with heat or pressure are utilized. Based on the bonding techniques, lamination processes can be divided into flame lamination, aqueous based-adhesive lamination, solvent based-adhesive lamination, heat lamination, and hot melt-adhesive based lamination [34, 35]. In addition, the thermo-compression bonding technique has been used for bonding metals [36, 37], nonwoven fabrics [38], and thermoplastic polymer microfluidics [39, 40].

More specifically, Laminated Object Manufacturing (LOM), one of the AM techniques, uses adhesive or binder to bond layers and build up objects. Each single layer represents the cross-sectional profile at certain location of the specimen [41-43]. Parts made by LOM are inexpensive, consistent, and with no chemical reaction involved. This technology works best for conceptual prototyping, scaled model or casting-mold fabrication. Selective Deposition Lamination (SDL) was invented to laminate the selectively-cut paper layers with adhesive and pressure in order to build up parts [44]. This method is commonly used by teachers, artists, and architects to build objects.

As some materials can achieve self-adhesion, the phenomenon can be utilized as a bonding strategy in lamination process. Self-adhesion of materials generally requires heat or diffusion; thus, thermal bonding or diffusion bonding can be considered as an alternative lamination technique. Some efforts have been made to investigate the polymer self-adhesion, and it was found that the phenomenon is due to inter-diffusion of

macromolecules [45-47]. A new phenomenon was reported that under about 60 K below glass transition temperature (Tg), solid-state condition, certain polymeric layers can be bonded on the order of a second when subjected to plastic deformation [48]. This is because the molecular-level rearrangement is triggered under sub-Tg and plastic deformation condition, and it results in inter-diffusion of polymer chains to cross the interface of layers and leads to bonding. The finding is very useful since it provides a convenient and quick way to bond polymer. However, from the mechanical perspective, the plastic deformation changes the original geometry of the specimen, and gives rise to issues when processing specimens to meet certain desired dimension tolerances.

In addition to the fabrication of FGPMs, it is often of great interest to investigate their mechanical properties, as well as to predict their behaviors under different loading conditions. Previous approaches on deriving analytical models for composite material including rule of mixture, self-consistent model, Mori-Tanaka model, method of cell, and homogenization method. The first three methods provide analytical solutions. Rule of mixture method gives the upper bound and lower bound of effective elastic modulus. The self-consistent model is known for providing a good prediction for skeletal microstructure with a wide transition range between the two phases, and Mori-Tanaka model is proven to have accurate predictions for the mechanical property of composites with discontinuous inclusions embedded in a “well-defined” continuous matrix [49, 50].

It is known, however, that Mori-Tanaka method has no solution for the interconnected cavity problem [51], and it has not been applied to model graded porous composite materials. In addition, the method assumes incompressible matrix and inclusion; while for porous materials, the volume of pores changes during deformation. Treating voids as inclusions could lead to inaccurate predictions. Therefore, further investigation of applying Mori-Tanaka's scheme to model closed cell and open cell FGPMs is needed.

1.2 Motivations

Functionally graded porous materials widely exist in nature, and engineered FGPMs have broad applications in industry. As a porous material, FGPM has high stiffness to mass ratio that is favorable in transportation and aeronautics industries. As a graded material, it has material property gradient over the volume which can be used as damping, thermal gradient, biomedical, and building materials. Based on these applications, it is of great interest to fabricate FGPMs with precisely controlled geometrical structure and mechanical properties. It is also necessary to develop a cost-effective manufacturing technique so that mass production can be achieved and the fabrication approach can be widely adopted by industries. In this research, a novel

fabrication approach that is able to produce both open cell and closed cell FGPMs with precise part geometry is investigated.

Analytical model can be a powerful tool to predict material behavior under different loading conditions. It also enables the evaluation and selection of the base material and geometry when designing a desired material structure. Since there is no available model for FGPMs, in this research, an analytical approach for modeling porous graded material based on Mori-Tanaka's scheme is proposed. The model is expected to deliver accurate prediction results.

1.3 Research Objectives

There are two main objectives in this dissertation research. The first objective is to develop a new fabrication method to manufacture FGPMs based on lamination processes. In addition to the commonly-used adhesive bonding technique, this research will focus on thermal bonding method. Thermal bonding process involves heating the polymer close to Tg (or between Tg and melting temperature Tm) to bond polymer layers through self-adhesion. With the controlled pressure, temperature, and heating time, polymeric FGPMs can be fabricated with no or little plastic deformation. This

lamination technique is simple, convenient, and cost-effective. In addition, the technique can provide high resolution and accurate geometry.

The second objective is to develop analytical models to predict mechanical behaviors of FGPMs with known base material properties and geometric structures. To achieve this objective, the Mori-Tanaka method will be adopted to model the constitutive behavior of porous material layers. The work will then be extended to consider graded fields and interconnected pores. The mechanical properties of the fabricated FGPMs will be characterized and compared to the model predictions.

In this dissertation, literature reviews including various approaches to fabricating FGMs, previous work on lamination, and mathematical modeling of the mechanical behavior of composite and porous materials are presented in Section 2. In Section 3, the thermo-bonding lamination process and the evaluation of bonding shear strength through lap-shear test is discussed, the fabrication of FGPMs and the material characterization through the compression test are presented. Analytical model derivation dealing with graded porous material and interconnected open cell structure, and numerical model of FGPMs based on RVE with periodic boundary condition (PBC) are described in Section 4. Section 5 presents the comparison of modeling and experimental results. A discussion about prediction accuracy of analytical model will be also presented. The conclusions and future work are summarized in Section 6.

2. LITERATURE REVIEW

To provide the background of this research, the review of previous literatures consists of three parts, i.e., fabrication of functionally graded porous materials (FGPMs), lamination processes and bonding techniques, and modeling of mechanical behavior of composite and porous materials. In Section 2.1, common methods for fabricating metallic and non-metallic FGPMs with open and closed cells are reviewed. The review of existing lamination technology and their applications is presented in Section 2.2. Section 2.3 examines methodologies of modeling mechanical property of composite and porous material. In Section 2.4, the approach to numerically model the composite materials is discussed.

2.1 Fabrication Methods for Functionally Graded Porous Materials

Functionally graded materials (FGMs) are composites materials consist of two or more phases with a graded changing composition over the volume [1, 2]. The material can have certain desirable property of each constituent phase, sometimes even contradictory properties, such as both high hardness and high toughness [52]. FGMs are usually associated with particulate composites and their thermo-mechanical

performances are excellent. It has wide applications in automobile, aerospace, energy, and optoelectronics [53] .

Functionally graded porous materials (FGPMs) are porous materials with porosity gradually changing throughout the volume. As a porous material, it has high stiffness to weight ratio, and can be used for impact energy adsorption, construction, water permeability, acoustic absorption, and sound absorption. As a graded material, its porosity is gradually changing, and can be potentially used as damping, cushioning, filtration, and biomedical materials. Based on the cell structure, FGPMs can be open cell or closed cell structures. In open cell porous material, the pores are interconnected; in contrast, each cell is enclosed and isolated by base material in closed cell structure.

Section 2.1.1 lists the approaches used for fabricating open cell structures, and Section 2.1.2 demonstrates the methods for the fabrication of closed cell structures. Section 2.1.3 deals specifically with techniques used for fabricating polymeric porous materials. In Section 2.1.4, a discussion about manufacturing porous materials using additive manufacturing techniques were provided.

2.1.1 Methods for Fabrication of Open Cell Structures

A variety of methods were developed in order to fabricate open cell porous materials. In order to manufacture open cell materials where pores are interconnected, powder sintering is a commonly used approach, which refers to the process of compacting and forming powder by heating and applying pressure without melting it [54]. This relatively high temperature treatment process involves the bonding of powder particles without much change of the particle shape. Both metal powder and polymer powder can be used in this technology. For metal powder, Pure Ti [13, 55], Ti alloys [56, 57], bronze [58], and Co alloys [59, 60] are commonly used materials, and the resulting porosity can range from 5% to 40%. For example, Thieme *et al.* [9] fabricated FGPMs for orthopedic implants using titanium powder sintering and the resulting Young's modulus can cover the typical range of cortical bone. For polymer sintering, different materials were used, e.g. high density polyethylene (HDPE) [58], nylon [61], polypropylene copolymer [62], and acrylonitrile butadiene styrene (ABS) [63]. To create hollow structures, a rotational mold are sometimes used. Besides powder sintering, fiber sintering is also used in order to achieve high strength and ductility [64].

Other powder based technologies for making open cell structures include the space holder technique [14], replication [15], and plasma spraying method. In the space

holder method, high porosity can be achieved by compaction of the mix of powder and space holder material, and removal of space holder after a well-controlled heat treatment. To ensure the removal of the space holder material, the melting temperature of the powder should be higher than that of the space holder material. Li. *et al*. [65] used replication method to create porous titanium alloy up to 88% of porosity. Instead of polymer space holder, a polymer foam was added into a slurry consists of powder, pure water, and ammonia solution. Drying process, the removal of polymer foam, and sintering were followed step by step before the final product is obtained [17]. Freeze-casting of porous metallic and ceramic materials has also been received some attention. Like replication method, the resulting porous material is a replica of the frozen solvent crystals. In freeze-casting, the slurry is added and then solidifies in the mold. The freezing solvent would sublime before sintering of the desired material. The process can create micro-pores with pore size ranging between 2 to 200 μm[66, 67]. Besides, plasma spraying [68] and combustion synthesis [69] were also used to create open cell structures. In addition, electro discharge compaction approach was proven to be a viable method to fabricate functionally graded materials [16].

2.1.2 Methods for Fabrication of Closed Cell Structures

Comparing to open cell structures that are generally made from powder, closed cell materials are mostly created from liquid or melt. Casting is one of the most frequently used techniques to fabricate closed cell FGPMs. Foaming process is used with casting for creating porous structure with a desired part shape. The gas source can be divided into two types: blowing agent which decomposes after certain time, and dissolved gas which causes foaming instantaneously [18]. Gas, e.g. argon, air, and nitrogen gas, is injected into molten materials with a rotating mixer can result in uniform porosity distribution. An alternative approach is to add blowing agent since the decomposition of blowing agent under heating will release gas. This process can generate porous materials with high porosity ranging from 60 to 97%. The Gasar process is based on gas-eutectic reaction, which occurs during solidification of materials saturated with hydrogen. When the material solidifies, gas precipitates and is entrapped in the material to create porous structure [70, 71]. The Gasar process can be used for a wide range of metals, including nickel, copper, aluminum, titanium, and iron. Lost foam casting is able to produce metallic foam with the evaporation of mold made from organic foam. The porosity can be achieved as high as 95%.

2.1.3 Methods for Fabrication of Polymeric Porous Materials

This subsection specifically reviews the fabrication methods for polymeric porous materials. These fabrication approaches includes: (1) gas foaming, (2) phase separation, (3) solvent casting and particle leaching, (4) emulsion freeze drying, (5) templating, (6) molecular imprinting [72, 73].

As discussed above, gas foaming is not only widely used to produce polymer foams, but also applied to make scaffolds, with supercritical fluid as a blowing agent. Phase separation technique adopts porogen where solidification is used to fix the shape. Based on the separation mechanism, three different methods were developed, e.g. immersion precipitation, thermal – induced phase separation, and chemically induced phase separation. Immersion precipitation refers to the process to immerse polymer-solvent mixture into a coagulation bath containing nonsolvent. Young *et al.* [74] formed thin membrane of PVDF by immerse precipitation in harsh and soft nonsolvents, and achieved a uniform microporous structure with spherical particles about 1.5 μm in diameter. Anisotropic microporous membranes were also developed [75]. Thermally induced phase separation refers to polymer-rich and polymer-poor phases separation when cooling down a high temperature-homogeneous polymer solution. Nam and Park

[21] made biodegradable polymeric microcellular foam with different pore geometries and reached an average diameter of about 15 μm.

Solvent casting and particle leaching is commonly used to make scaffold where the solvent is evaporated followed by particle leaching when the material is immersed in solution to create porous polymeric materials [73]. Zhu and Chen [76] successfully fabricated scaffolds with porosity of about 93%. The material can be used as cancellous bone scaffold. Same efforts include using the same method to fabricate polyurethane biomaterial to support vascular cell and control the scaffold morphology [77, 78].

In addition, emulsion freeze drying, templating, and molecular imprinting were also used to make porous polymer material. However, these methods are relatively complicated since they require mold, machine, and/or foaming agents. More importantly, the exact pore size, overall porosity, morphology, and the gradient are hard to control when using these processes.

2.1.4 Fabrication of Porous Materials based on Additive Manufacturing Techniques

Additive Manufacturing (AM) is a powerful technology and it fabricates parts through a layer-by-layer fashion. Based on 3-D models generated from computer software, the porous material can be fabricated with a better control of microstructure,

e.g. dimension, size of pore, porosity, morphology, and overall shape, compared to conventional technologies discussed above. As such, it is popular to produce porous materials with the available AM technologies. According to the way that layers are processed and deposited, AM technology consists of powder-based techniques, e.g. Selective Laser Sintering (SLS), Selective Laser Melting (SLM), Electron-beam Melting (EBM); light polymerized-based method, e.g. Stereolithography (SLA); extrusion-based approaches, e.g. Fused Deposition Modeling (FDM); and Laminating approach, e.g. Laminated Object Manufacturing (LOM) [79].

SLS sinters powder material using a laser as a point source as shown in Figure 2.1 (a). Metals, ceramics, and polymers all can be processed using SLS. Jande *et al.* [26] prepared polyamide epoxy material with uniform and graded porous structures using SLS. The graded porosity can be well controlled in the range of 5 to 29%. Polymeric matrix drug delivery devices were developed by Leong *et al*. [12], and the work focused on studying the effects of SLS process parameters, e.g. the power of laser beam and scanning speed, on the resulting porosity and drug release rate. Bioresorbable and biodegradable polymer materials such as polycaprolactone were adopted in order to potentially apply to bone and cartilage scaffolds [80, 81]. Other efforts include studying the effects of laser processing parameters and thermal control conditions on the material

properties [82], exploration and investigation for more available and suitable materials [83].

SLA builds parts layer by layer using lithographic methods, e.g. curing a photo-reactive resin with a UV light through photopolymerization as shown in Figure 2.1 (b). The materials used are mostly polymers, wax or wax compounds which have to be reactive resins. Liebschner [27] optimized the bone scaffold for load bearing application, and Yu [28] used SLA to fabricate functionally graded shape memory polymer which is able to response quickly to an external stimulus, and will return back to a certain structure or shape in a well-controlled varying fashion. The approach was proved to be cost-effective for rapid and mass production and is ready for engineering applications. Other applications include using biodegradable material for customized bone repair [84], live cell-scaffold [85], and heart valves [86]. The SLS technology greatly helps the fabrication of patient specific models and aids for complex surgery.

FDM as shown in Figure 2.1(c), one of the most popular AM techniques due to its low cost and easy-operation, is widely used for almost all kinds of part fabrication. In this process, the material is melted and then extruded through a nozzle and deposited onto a platen in a strand by strand and layer by layer fashion. Kalita *et al.* [10] used FDM to process polymer-ceramic scaffolds with a well-controlled porosity. The porous structure was proved to be a good bone graft with its biological, mechanical, and

physical properties aligned well with requirements. Yu *et al.* [87] proposed a hybrid bioprinting system to process scaffold-free cellular constructs for tissues and organ models using two micro-nozzles. Even the approach is still at proof-of-concept study stage, it demonstrated the potential for therapeutic purpose.

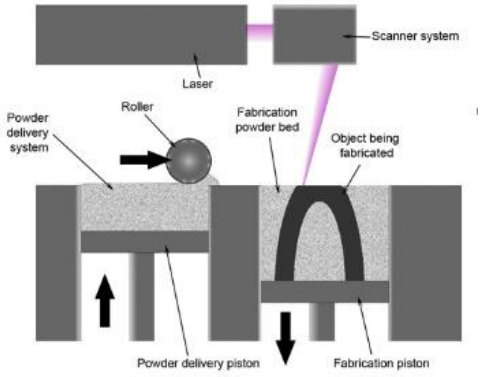

(a) SLS

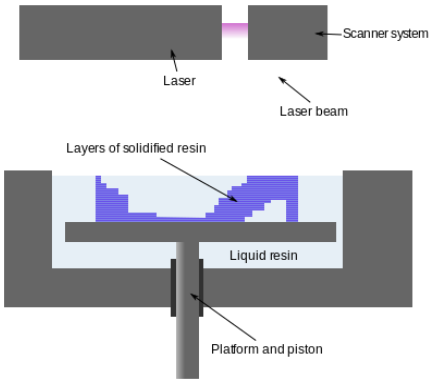

(b) SLA

Figure 2. 1 AM technologies (a) SLS (b) SLA (c) FDM [88-90]

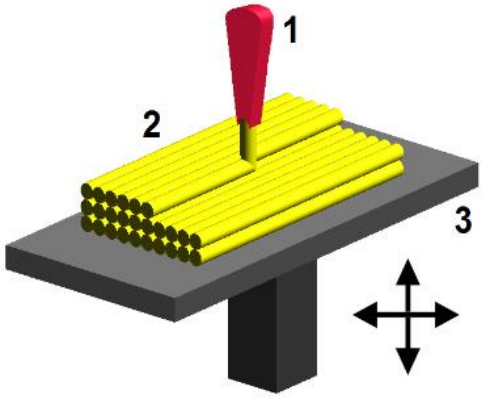

(c) FDM

Figure 2.1 Continued

Other available AM techniques such as freeze form extrusion fabrication [29], direct metal laser sintering (DMLS), and electron beam melting (EBM) [91] were also received extensive attention. However, an inevitable issue involved in all these AM techniques is that it relies either a different supporting material (in FDM) or the constituent/part materials (in SLS and SLA) to fill in space when fabricating porous parts. Some of the filler materials are hazardous or contain harmful chemical when disposal. It is also reported that the material consumption for the purpose of filling in space can be greater in volume and in cost than the actual part. More importantly, it is time-consuming to clean the filler material especially when the pore size is small. In addition, the AM technologies discussed above cannot be used for fabricating closed cell

porous structure, since the filler materials, no matter they are solid, liquid or powder, will be trapped in the cell and cannot be removed to create porous structure.

An alternate approach that can be used to fabricate porous materials without dealing with the filler material issues is lamination process.

2.2 Lamination of Porous Materials

Lamination is a process that fabricates materials in multiple layers in which the materials for each layer could be the same or different. The bonding process is generally achieved by adhesive, heat, pressure, and/or welding. Lamination technology has a variety of applications in biomedical, pharmaceutical, electronics, and automotive.

Section 2.2.1 discusses the existing lamination techniques. In particular, in Section 2.2.2, the thermo-compression bonding is reviewed. Polymer self-adhesion and its mechanism is discussed in Section 2.2.3.

2.2.1 Existing Lamination Techniques

One of the most commonly used methods to laminate materials is to apply adhesives. Based on the lamination techniques, it can be divided into flame lamination,

aqueous-based adhesive lamination, solvent-based adhesive lamination, pressure sensitive adhesive-based lamination, and hot melt-adhesive-based lamination [34, 35]. In flame lamination, the material is melted by flame and then pressed into contact with the substrate. To demonstrate the process, Singha showed that Polyurethane foam can be laminated to textile material by passing over a gas flame through a rolling system [35]. Aqueous based pressure sensitive adhesive can be used for bonding foams, fabrics, and porous substrates. It is either from nature polymer, e.g. vegetable sources, protein sources, or animal; or from soluble synthetic polymers, e.g. cellulose ethers, methylcellulose, polyvinyl alcohol, etc. [92]. In solvent-based adhesive, the performance for bonding micro-porous materials is determined by the polymer system in the formula. The solvent-based adhesive consists of two different types: wet bonding type where the bond is effective through the evaporation of the solvent, and contact type where pressure must be applied in order to form strong bonding. Unlike aqueous or solvent-based adhesive, pressure sensitive adhesive does not solidify but will keep viscous and tacky. Adequate pressure must be applied to ensure a strong bonding. The pressure sensitive adhesives are generally obtained from natural rubber, polyacrylates, and synthetic rubbers. Hot melt adhesives are thermoplastic polymers and would melt and bond material when subjected to elevated temperature. It can be reheated and re-solidified in

order to rebond once debonding occurs [93]. Thus, it is widely used in package, textile, automotive, and electronics industry.

Laminated Object Manufacturing (LOM) (as shown in Figure 2.2) is also a rapid prototyping process where layers of plastic, paper or metal are successively bind together and cut into the desired geometry [41-43]. It is actually a combination of additive and subtractive technologies in which the layers are built up together by heat and pressure with an adhesive, followed by laser cutting to the desired shape for each layer [94]. Griffin *et al.* [95] used LOM to fabricate functional ceramic components and obtained high purity and density alumina ceramic components. It was also successfully proved that material prepared by LOM has almost the same physical and mechanical properties as those produced by conventional pressing process [96]. Mueller and Kochan showed that LOM is an ideal approach for rapid tooling and patternmaking due to its low costs, low shrinking, high durability, and capability to produce large part [97]. Other efforts include process studies such as thermomechanical analysis [98], investigations on effects of different parameters, e.g. layer thickness and orientation angle on product quality [99].

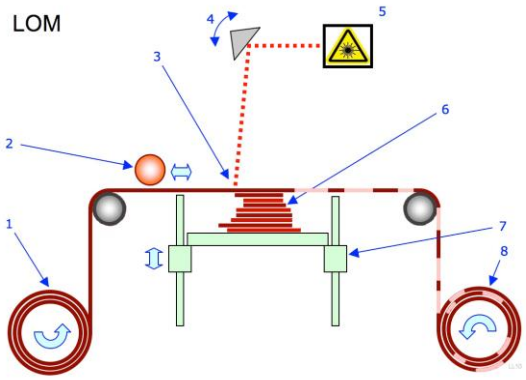

Figure 2. 2 LOM process [100]

Selective Deposition Lamination (SDL) (as shown in Figure 2.3) was invented to laminate the selectively cut paper layers with adhesive to build up parts [44]. One of the difference between LOM and SDL is that, in SDL the densities of adhesive drops are different in the part area and in the surround area, while in LOM process, the adhesive is applied in equal amount across the entire surface of the material. The fabricated objects can be used for architect models, classroom teaching materials, and other proof of concept models.

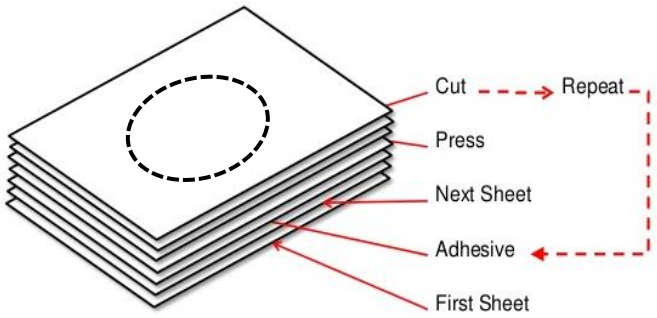

Figure 2. 3 SDL process [44]

Using lamination process to fabricate porous material is cost-effective, requires no supporting material and no post-processing. It solves the supporting problem in FDM, SLS, and SLA, and is able to build large parts. Thus, in this research, lamination will be used to manufacture the FGPMs.

2.2.2 Thermo-compression Bonding

An alternative to adhesive bonding in lamination process is the thermo-compression bonding. The bonding between two materials is generated when the materials are brought into contact with properly applied force and heat. The bonding is due to diffusion caused by atomic or molecular motion. It is widely used for metal bonding, e.g. wafer bonding, and is an ideal bonding technique for integrated circuits,

nanocrystalline metal film [36, 37], nonwoven fabrics [38], and thermoplastic polymer microfluidics [39, 40].

2.2.3 Polymer Self-adhesion

The thermo-compression bonding can also be used for polymer-polymer bonding. The polymer self-adhesion phenomenon is due to inter-diffusion of macromolecules and has attracted great attention since it can be used as a convenient binding process. According to McLaren, there are two stages for self-adhesive bonding [45]. In the first stage, the micro-Brownian motion drives polymer molecular to migrate to the interface of materials. As the polar groups of both materials approach to each other, the chain segments also approach to the inter-surface. In the second stage, intermolecular force is effective as the polymer molecules become close enough, and the force is ranging from 10^2 cal./mol to 10^4 cal./mol, which eventually lead to bonding. This process was further investigated to measure the self-diffusion coefficient and to develop mathematical model [46, 47].

A new phenomenon was reported that under sub-Tg (around 60 K below Tg), solid-state condition, a particular polymeric film can be bonded on the order of a second when subjected to plastic deformation [48]. This is because the molecular-level

rearrangement is triggered under sub-Tg and plastic deformation conditions, and it results in interdiffusion of polymer chains to cross the interface and thus leads to bonding as shown in Figure 2.4. This convenient and quick way to generate bonding in polymer layers is being considered in pharmaceutical manufacturing. However, from the mechanical perspective, the plastic deformation changes the geometry of the specimen, and gives rise to issues when processing the specimen and modeling its mechanical behavior.

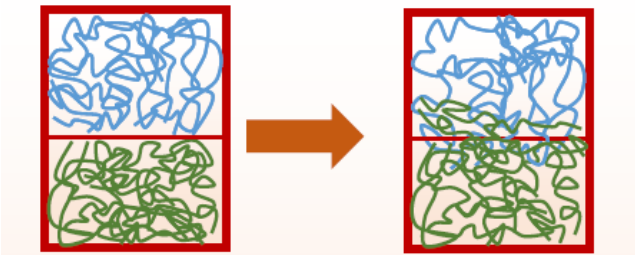

Figure 2. 4 Interdiffusion of polymer chain [48]

An alternative approach is to heat the polymer close to Tg (sometimes higher than Tg but lower than Tm), and the polymer layers would bond without being subjected to large plastic deformation. This bonding approach is effective and can be applied to a variety of polymers. With the controlled-temperature thermal bonding, polymeric FGPMs can be fabricated without applying large plastic deformation or using the

supporting material as in other AM technologies. This lamination technique is convenient, easy, and inexpensive. Besides, it can produce parts with good resolution and accurate geometry.

2.3 Modeling Mechanical Behavior of Composite and Porous Material

Composite and porous materials are intensively used in automobile, space, aeronautical, biomedical, electronics industries. The composite porous materials with different manufacturing methods, dimensions, geometries, and porosity have very different mechanical behaviors. From the review of previous work in mechanical modeling of composite porous material, the major modeling methods fall into two categories: (1) analytical approaches to derive models to predict mechanical behavior; (2) finite element method to simulate the mechanical performance of the materials. The reviews of analytical modeling methods and finite element methods are presented in Section 2.3 and Section 2.4, respectively.

Section 2.3.1 summarizes the analytical models for composite materials. Analytical models dealing with FGM without and with porous structures are discussed in Section 2.3.2 and Section 2.3.3, respectively.

2.3.1 Analytical Modeling for Composite Materials

Significant efforts have been taken into developing material models for composite materials. Micromechanics approach is one of the most frequently used methods. It is a homogenization process which involves deriving the mechanical behavior of the composite material based on the mechanical property and geometry of each individual constituent [101]. The representative volume element (RVE) is generally used in micromechanics. The RVE is defined as a sub-volume of the composite whose size is sufficient large enough for representing all the geometry information but also the smallest unit that can be used to study in order to yield a result representative of whole structure.

The rule of mixture approach developed by Voigt [102] and Reuss [103] are widely used since it yields the upper bound and lower bound of the overall mechanical property. Hashin investigated transversally isotropic composites and macroscopically isotropic composites, and also provided bounds on the elastic moduli [104, 105].

Eshelby [106] investigated the stress and eigenstrain field inside an ellipsoid inclusion which is embedded an infinite matrix. He concluded that the Eshelby's tensor S_{ijkl} is a constant tensor in the case of an ellipsoidal inclusion embedded in a homogeneous infinite medium, and it only depends on the dimension of the inclusion,

and the eigenstrain inside the inclusion are uniform. A series of analytical models were developed based on Eshelby's tensor. The self-consistent scheme [107, 108] is an effective medium approximation based on Eshelby's tensor, and it uses the material properties of the composite as the infinite medium. Christensen improved the self-consistent model by developing the generalized self-consistent model [109] that was further investigated by Nemat-Nasser [110, 111]. In this model, the Eshelby's tensor is not a constant, rather, it is a periodically fluctuating function. Mori-Tanaka method [112, 113] is an effective field approximation method with a fourth order strain concentration tensor that relates the volume average macroscopic strain to the volume average eigenstrain in the inclusion. Other methods, including the Chamis model [114], the Halpin-Tsai model [115], and the Differential scheme [116, 117] were also derived to model the mechanical property of composites.

2.3.2 Analytical Modeling for FGM without Porous Structures

In order to derive the mechanical model of FGM, the variation of volume fraction of each constituent in the graded direction can be assumed, e.g. variation according to a power law [118] and variation of volume fraction as a function of coordinate [119]. Other investigations studied FGMs on the basis of the graded field

relative to the size of RVE. If the volume fraction changes relatively slow with respect to spatial coordinates, the material can be considered as homogeneous at RVE scale, but globally heterogeneous on the macro scale. Standard homogenization methods such as dilute model, self-consistent schemes, and Mori-Tanaka model can still be applied to study its mechanical response. Zuiker [41] applied Mori-Tanaka model, self-consistent model, and Tamura's model to predict the effective stiffness of FGMs and compared the results with experiments, and commented that the former two methods are more reliable. Reiter [50, 120] did similar work by investigating the mechanical property of graded composites using different micromechanical models. Four models were developed by Pal [121] using a differential approach to solve the problem of an incompressible medium with a dilute concentration of ellipsoidal particles. Zuiker [122] extended Mori-Tanaka model to linearly variable local fields in order to yield better prediction for functionally graded materials with a variable density of reinforcement or a large overall stress density.

2.3.3 Analytical Models for Porous Materials

Efforts have been made on predicting the effective elastic properties of porous materials. Zhao *et al.* [123, 124] derived the effective moduli for a variety of porous

materials by setting the inclusions stiffness to zero, and they proved that when the matrix has lower elastic property, the effective moduli of overall material obtained from the Mori-Tanaka's method agreed well with Hill and Hashin's lower bounds; and coincided with the upper bounds when the matrix is the harder constituent. The compressibility of 2-D pores of various shapes under hydrostatic stress were studied by Zimmerman [125], who used a technique of mapping a pore onto a unit circle. Later on Zimmerman further investigated the volume change of a single ellipsoidal cavity in 3-D case. Walsh [126] also investigated the effect of porosity on the compressibility of different materials. Efforts were made to obtain the stiffness of solids with non-interacting pores, and a fourth rank tensor called cavity compliance tensor were proposed to facilitate the derivation, and the expressions were derived for different shapes of cavities [127]. For interacting defects, differential scheme, self-consistent scheme, generalized self-consistent scheme, and Mori-Tanaka' scheme [128] were generalized and applied.

2.4 Finite Element Study for Composite Materials

Finite element method (FEA) is a numerical approach for obtaining approximate solution to boundary value problems for mathematical models. The method subdivides the whole model into simpler, smaller geometry called finite elements. The solution for

each small finite element is then assembled over the whole model to achieve the solution. This method is widely used in material performance modeling.

In Section 2.4.1, numerical models developed for composite material are discussed. Section 2.4.2 demonstrates the periodic boundary conditions for RVEs.

2.4.1 Numerical Models for Composite Materials

FEA is an efficient way to obtain the effective stiffness of composite materials. Some of the models assume periodic arrangement of the material. The homogenization theory was first used by Babuska [129] and Keller [130] for studying effective behavior of heterogeneous material, and then was applied to study the composite materials [131]. Hollister and Kikuchi [132] used an asymptotic expansion to approximate the field variables and provided a clear description of this theory. Method of cell was developed by Aboudi *et al*. [133, 134]. It explicitly considered reinforcement and matrix subcell from periodic unit cell, and was later generalized to model FGMs. The method first assumed displacement field in the subcells and then applied displacement and traction continuity between the neighboring subcells and cells. Investigations related to FEA study of FGMs were also carried out [91, 135-137] for designing porous structure and studying its behavior under different conditions.

2.4.2 Periodic Boundary Conditions

To numerically model the mechanical behavior of composites using the RVE approach, periodic boundary condition (PBC) should be applied to ensure the deformation compatibility. To satisfy PBC, the shape and displacement of two opposite edges should be identical during the deformation [138]. Figure 2.5 shows a typical 2-D unit cell, the lengths of edge in y_1, y_2 direction are a_1 and a_2, respectively. Based on periodicity assumption, it follows Eq. (2.1) [139]:

$$\begin{aligned} u_{\Gamma_{12}} - u_{v_4} &= u_{\Gamma_{11}} - u_{v_1} \\ u_{\Gamma_{22}} - u_{v_1} &= u_{\Gamma_{21}} - u_{v_2} \end{aligned} \tag{2.1}$$

where $u_{\Gamma_{ij}}$ denotes the displacement vector for points on edge Γ_{ij}; and u_{v_1} denotes the displacement vector for each vertex v_i. It can be also written in the form of Eq. (2.2):

$$\begin{aligned} u_{\Gamma_{12}} - u_{\Gamma_{11}} &= \begin{bmatrix} \varepsilon_{11} & \varepsilon_{12} \\ \varepsilon_{21} & \varepsilon_{22} \end{bmatrix} \begin{bmatrix} 0 \\ a_2 \end{bmatrix} \\ u_{\Gamma_{22}} - u_{\Gamma_{21}} &= \begin{bmatrix} \varepsilon_{11} & \varepsilon_{12} \\ \varepsilon_{21} & \varepsilon_{22} \end{bmatrix} \begin{bmatrix} a_1 \\ 0 \end{bmatrix} \end{aligned} \tag{2.2}$$

where ε_{ij} denotes the strain tensor of the unit cell.

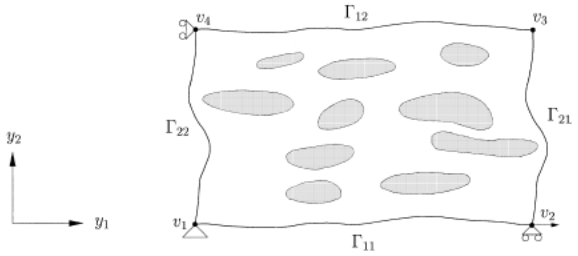

Figure 2. 5 Unit cell with PBC [139]

3. EXPERIMENTS

Material bonding has always been important for lamination process. Applying adhesive is one of the most commonly used methods to generate bonding between layers. However, polymer self-adhesion is also a very promising approach that has the potential to attract a lot of attention due to its low-cost and effectiveness. The aim of this section is to show the feasibility of applying thermal bonding technique to laminate polymer sheets to create three-dimensional objects, and to investigate the material behavior of the laminated FGPMs experimentally. The FGPMs are also built up by using adhesive as an alternative. Lap shear tests were conducted to investigate the shear strength of the thermally bonded specimens, while the effects of applied pressure, heating temperature, and holding time on the shear strength were studied. The compression tests were carried out to characterize the elastic compressive behavior of the porous structure under normal and transverse loading conditions.

In Section 3.1, it is demonstrated that the thermo-bonding process can be used to laminate polymer layers to build-up specimen. Lap-shear tests were carried out to study the shear strength of the bonding. In Section 3.2, FGPMs with different configurations, i.e. different geometries, constant porosity and graded porosity, closed cell and open cell

structures, were fabricated using either the thermo-bonding or the adhesive bonding techniques. The materials were also characterized using mechanical testing.

3.1 Lamination Using Thermo-bonding

In this section, the feasibility of thermally-induced lamination process is demonstrated by bonding two layers of polymer sheets through the thermo-bonding process. The single-layer made from polymeric material was first fabricated by Fused Deposition Modeling (FDM), and then processed to form specimens. In Section 3.1.1, the material properties of base material and the preparation of single-layer samples are described. Section 3.1.2 presents the experimental procedure for lamination. Various thermo-bonding conditions, i.e. different applied pressure, heating temperature, and holding time, were used to bond the single-layers in order to achieve different bonding shear strength. Lap-shear testing of specimens, presented in Section 3.1.3, was carried out in order to investigate the shear strength of bonding. The effects of different process parameters on shear strength are discussed.

3.1.1 Base Material Property and Preparation of Single-layers

In order to perform the lamination process, single-layers of material need to be fabricated first. The geometry of these single-layers depends on the final product – the final product is a build-up of the multiple thin layers, or the final product is considered to be "sliced" into multiple layers, and each layer has specific geometry and porosity. In this experiment, single-layers were fabricated by 3-D printing machine FlashForge Dreamer. Polylactic acid (PLA) was selected as the base material in this work due to its low glass transition and melting temperatures as well as its low shrinkage after cooling. In 3–D printing of PLA, the layer thickness of printing was set at 0.1 mm, and the infill percentage was set as 100% for all the printing process in this work. For the consistency, HATCHBOX PLA 3D printer filament with 1.75 mm in diameter and dimensional accuracy $\pm$ 0.05 mm was used in this work. The layer thickness and width of filament was selected in order to maintain the dimensional accuracy of printing parts. The glass transition temperature and melting temperature of PLA filament are 60-65^{o}C and 150-160 ^{o}C, respectively. The elastic modulus of PLA is 3.5 GPa. The individual layers were first designed and drawn by Solidworks, and the .stl files were sent to Simplify 3D software which prepares the 3D model ready for printing by slicing the model in the printing direction and generating G code for the trajectory of nozzle.

3.1.2 Thermo-bonding Process

In this section, the thermo-bonding mechanism will be explained and the bonding approach will be elaborated. Lamination of the single-layers will be conducted in order to show the bonding process.

The mechanism of the thermo-bonding process

The thermo-bonding is caused by polymer self-adhesion due to the interdiffusion of polymer chains. Below Tg, even if the material is still in glassy and solid state, a certain amount of mobility of the polymer polar groups and chains can be triggered under proper conditions, and interdiffusion between polymer chains across the interfaces can occur [40]. Given time, as more and more polymer chains cross the interfaces, the interdiffusion would eventually lead to bonding as shown in Figure 3.1.

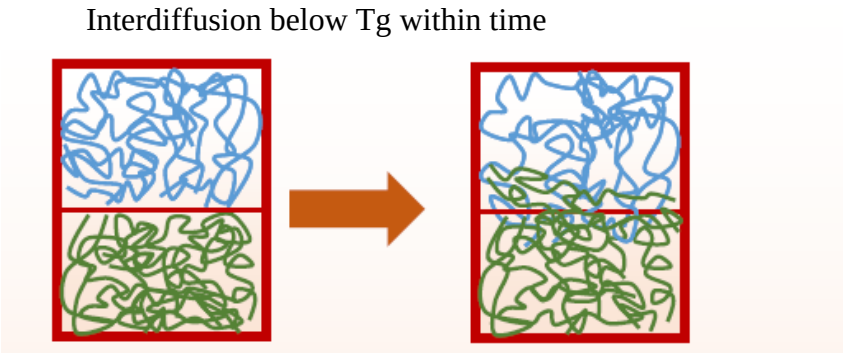

Figure 3. 1 Interdiffusion across the polymer chains [48]

Experimental procedure for the thermo-bonding process

In order to investigate the thermal bonding lamination process and improve the bonding, the surface of the single layer sample should be carefully cleaned. This was achieved by degreasing the surface using CSM Degreaser. The surfaces were then carefully dried with a gauze sponge. In addition, any burs due to 3-D printing would be removed to ensure the surface-surface contact when thermal bonding. In order to avoid surface contamination, the cleaned single layer samples were bonded within 30 min after the surface cleaning.

During the thermo-bonding lamination process, the single-layers were carefully aligned and built up according to the desired geometry of the final product. A CARVER

hydraulic unit model #3925 heating compression machine was used to heat the polymer layers. The heating temperature is up to 10 to 20 Celsius degree below the glass transition temperature (Tg) for some polymers, such as Acrylonitrile Butadiene Styrene (ABS), Polycarbonate (PC), etc.; or between Tg and melting temperature (Tm) for other polymers, such as PLA, Polypropylene (PP), Polyethylene (PE), etc. An “L” shaped fixture was made in order to ensure the alignment of layers. The height of the fixture was properly controlled to make sure the upper die can fully compress the built-up layers. Figure 3.2 shows the experimental setup for the thermal bonding process.

The thermo-bonding process was then held for sufficient time to allow enough interdiffusion. The heating temperature was carefully chosen through several trials to make sure that a strong bonding can be achieved. During the thermal bonding process, a compressive load was applied in order to make sure that each layer is in close contact with the neighboring layers. This thermal bonding lamination processes were carried out on PLA specimens.

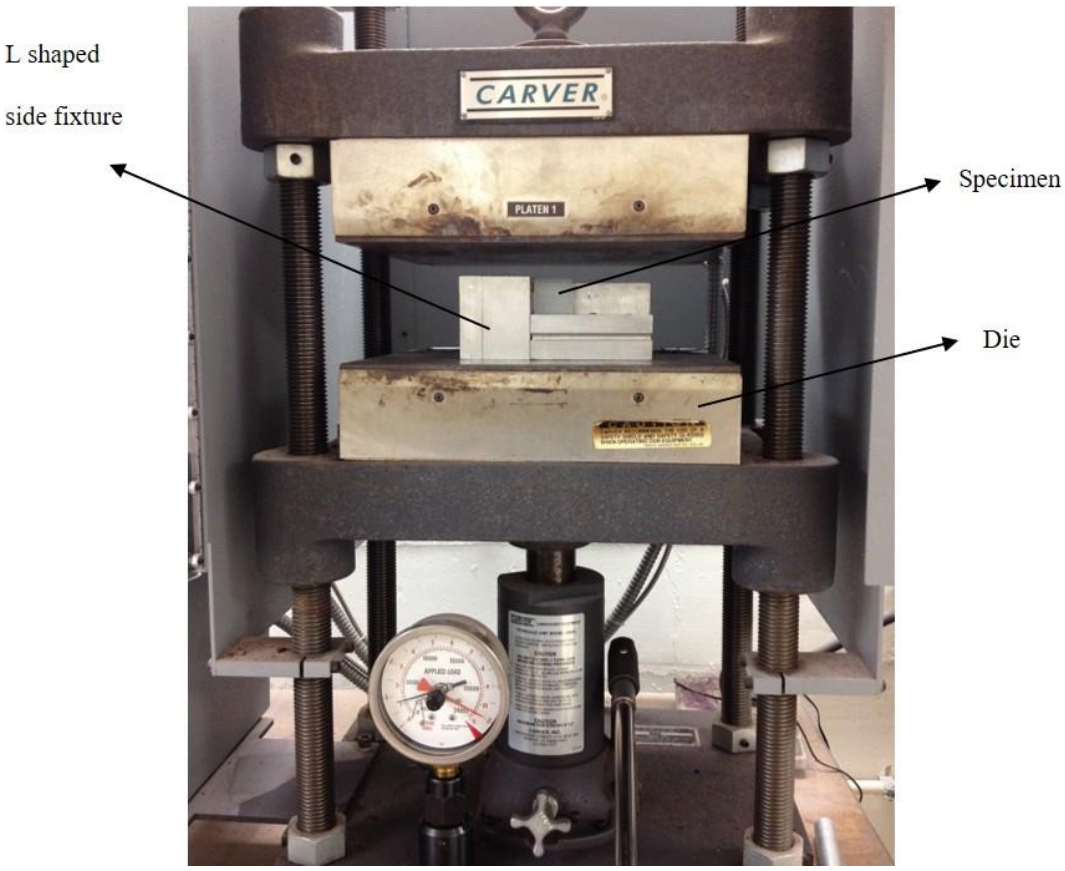

Figure 3. 2 Experimental setup for the thermal bonding process

Investigations on factors which influence bonding shear strength

The shear strength of bonding can be affected by different process parameters. From diffusion theory, it is known that time, temperature, and pressure are critical factors that strongly influence diffusion. Therefore, different pressure, heating

temperature, and holding time were used to study their effects on polymer interdiffusion and bonding strength. Three different parameters were chosen for each factor.

To minimize the dimension change caused by applied pressure, the first set of experiment is to study the pressure effect and determine how much pressure is needed. Three different pressure, i.e. 0.5 MPa, 1.0 MPa, and 1.5 MPa were used to do the investigation. The heating temperature and holding time were set at Tm-10C and 75 min, respectively. Table 3.1 lists the condition applied for studying the effects of pressure. It was then found out that 0.5 MPa of pressure is high enough to develop very strong bonding and also result in plastic deformation which will cause dimensional change. Therefore, pressure was kept as a constant and low when investigating the effects of heating temperature and holding time on bonding shear strength. The constant pressure was achieved by using an aluminum spacer which has high elastic modulus compared to PLA, and can prevent the upper die from moving down to deform the layered FGPMs further.

The testing matrix for temperature and time investigation is shown in Table 3.2. The heating time listed includes the time used for heating up the upper and lower dies. As can be seen from Table 3.2, there are 5 different trials since the experiment under the condition of “Tm – 10C” and 75 min is in both temperature and time studies. For each condition, three samples were tested.

Table 3. 1 Conditions applied for studying the effects of pressure

	Pressure	Heating Temperature	Time
Investigation for pressure	0.5 MPa	Tm-10C	75 min
	1.0 MPa		
	1.5 MPa		

Table 3. 2 Experimental testing matrix for temperature and time evaluation

	Heating Temperature	Time
Investigation for heating temperature	Tm	75 min
	Tm-10C	
	Tm-20C	
Investigation for time	Tm-10C	45 min
		75 min
		105 min

3.1.3 Lap-shear Test

Experimental procedure for lap-shear tests

Lap-shear tests were conducted in order to investigate the effects of different pressure, heating temperature, and time on the shear strength of thermally bonded specimens. The lap-shear specimens were prepared using Flashforge Dreamer 3-D printing machine as described in Section 3.1.1 and thermally bonded as described in Section 3.1.2. Figure 3.3 depicts the lap-shear sample. The right and left sides of the sample is designed for gripping purpose in lap-shear tests. The overlapping area in the middle is the bonding area.

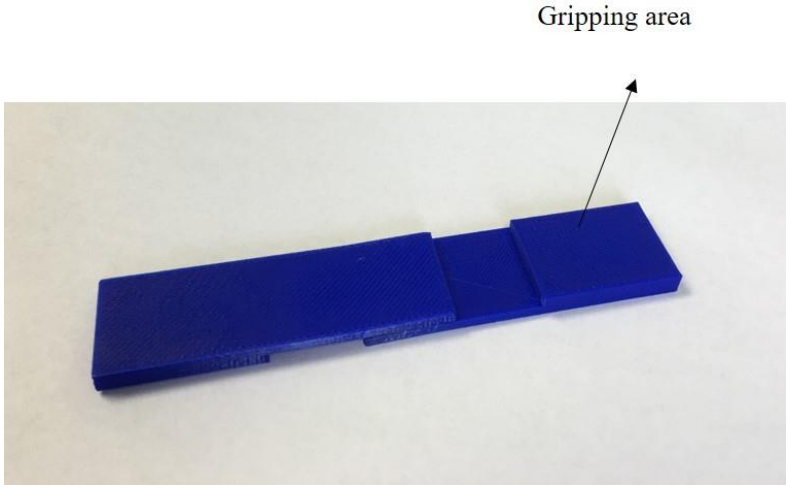

Figure 3. 3 Lap-shear sample

Lap-shear tests were performed using MTS Insight® Electromechancial testing systems with load capacity of 30 KN. The capacity of the load cell used is 2.5 KN, in order to ensure the accuracy of load measurement. The testing speed of cross head was kept at 0.1 mm/min. The overlapping area was measured and calculated before and after each test. An experimental set-up for the lap-shear test is demonstrated in Figure 3.4. The testing parameters, are listed in Tables 3.1 and 3.2. Three repetitive tests were conducted for each condition.

After each test, the load-displacement data is exported, and the lap-shear strength is calculated as the maximum load before failure divided by the bonding area.

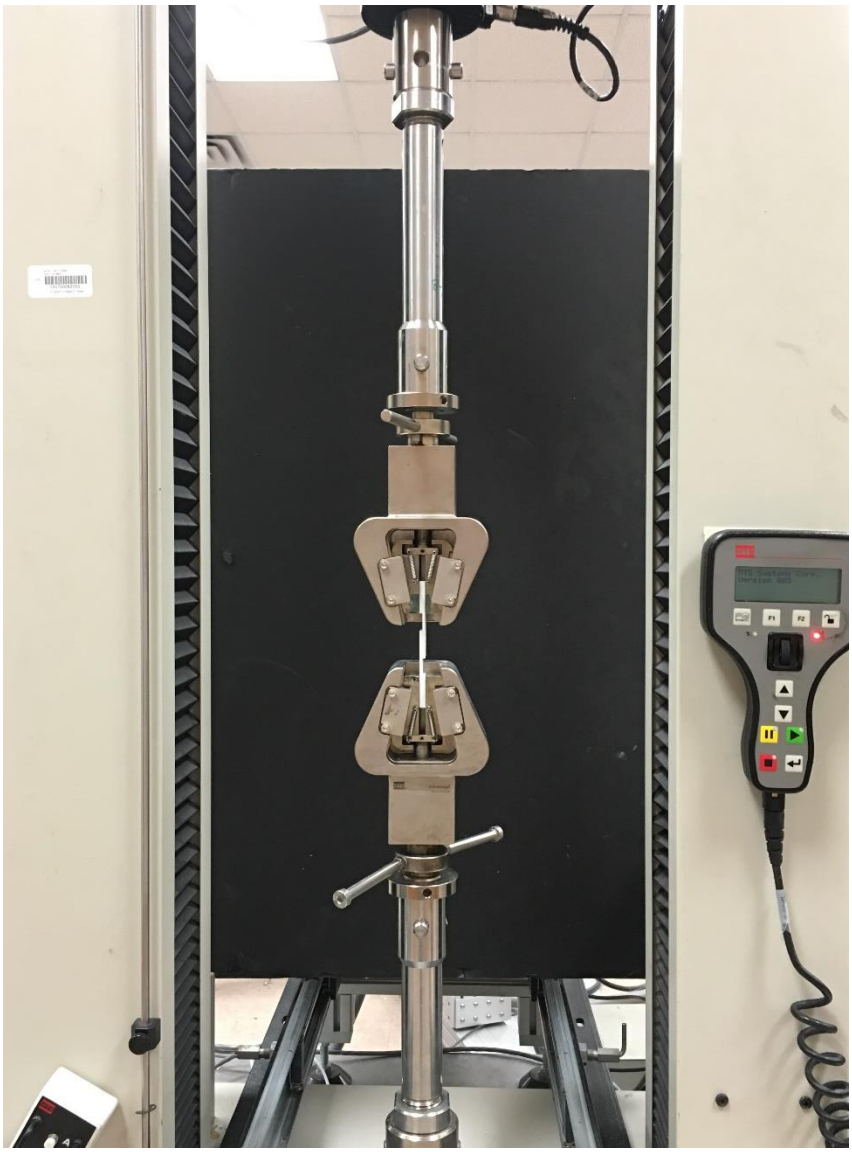

Figure 3. 4 Experimental set-up for Lap-shear tests

Experimental results for lap-shear test

Lap-shear tests were used to measure shear strength of thermally bonded specimens and investigate the effects of heating temperature and time on shear strength of bonding. The variations of load-displacement curves under different pressure are shown in Figure 3.5. It should be also noted that pressure has significant influence on shear strength of bonding, these specimens fail at where the stress concentrated and there is no obvious debonding occurs in the bonding area. More importantly, this indicates that 0.5 MPa (or above) of applied pressure is high enough to develop strong bonding under Tm-10C while holding for 75 min.

Tables 3.3 shows the shear strength data, and it was observed that with an increase in applied pressure, the shear strength also increases since it is 0.997 MPa under the pressure of 0.5 MPa, 1.531 MPa under the pressure of 1.0 MPa, and 2.041 MPa when the applied pressure is 1.5 MPa.

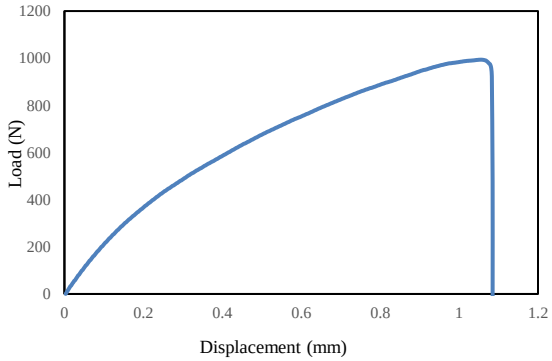

(a) 1.5 MPa

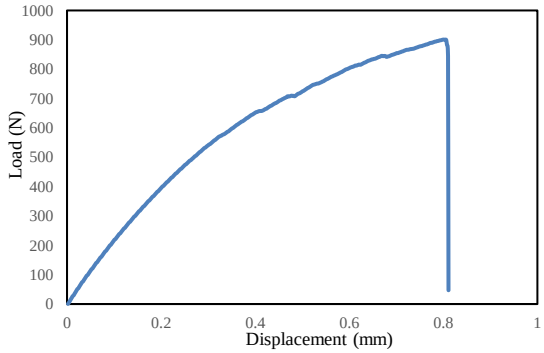

(b) 1.0 MPa

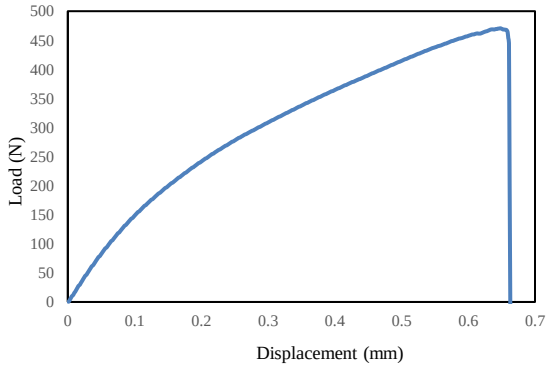

(c) 0.5 MPa

Figure 3. 5 Load versus displacement plot for lap-shear specimen under different pressures heated at 140 C held for 75 min

Table 3. 3 Variation of shear strength under different pressure

at heat temperature and time of 140 C and 75 min

Pressure applied	0.5 MPa	1 MPa	1.5 MPa
Shear strength (MPa)	0.997	1.531	2.041

As mentioned above, low pressure applied, i.e. 0.5 MPa, is high enough to cause plastic deformation. As such, in order to eliminate dimensional change, pressure was kept as a constant during the fabrication of specimens, and the pressure was applied only for densifying the build-up layers. The load-displacement curves for lap-shear specimens under different heating temperatures and constant pressure held for 75 min are depicts in Figure 3.6. It is observed that heating temperature has significant effects on shear strength since closer to Tm, the shear strength is much higher than that heated under Tm-20C. It is reasonable since the molecular mobility is triggered and chain movement is speeded up under higher temperature. In Figure 3.6 (b), the slope of the curve dropped at about displacement x=0.55 mm, this is because the specimen is slightly debonded, but still can carry further loading. However, the load and displacement at first debonding in Figure 3.6 (b) are higher than that in Figure 3.6 (c) (where load and displacement at debonding is about 325 N and 0.31 mm, respectively), indicating that shear strength of

specimen bonded at a higher temperature is much stronger than that bonded at a lower temperature.

Table 3.4 lists the bonding shear strength under different temperatures, as can be seen that the shear strength is 0.617 MPa when the heating temperature is 130 C, and 0.931 MPa and 1.037 MPa for 140 C and 150 C, respectively.

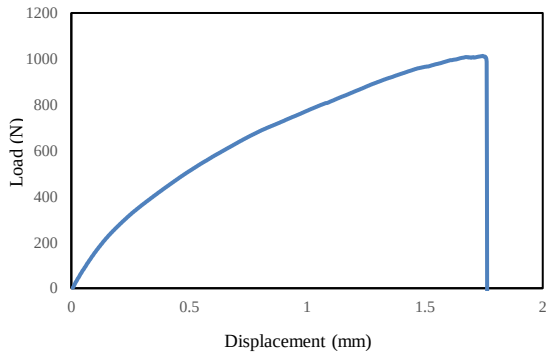

(a) Heating temperature 150 C

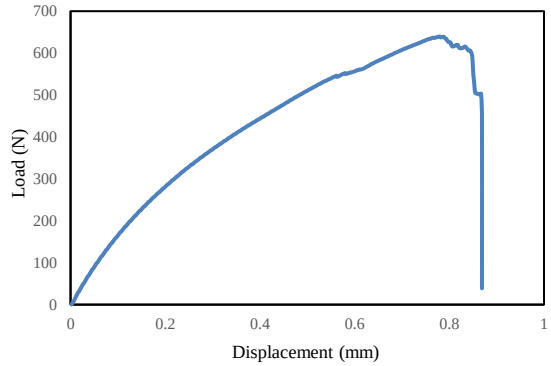

(b) Heating temperature 140 C

Figure 3. 6 Load versus displacement plot for lap-shear specimen under (a) 150 C (b) 140 C (c) 130 C held for 75 min

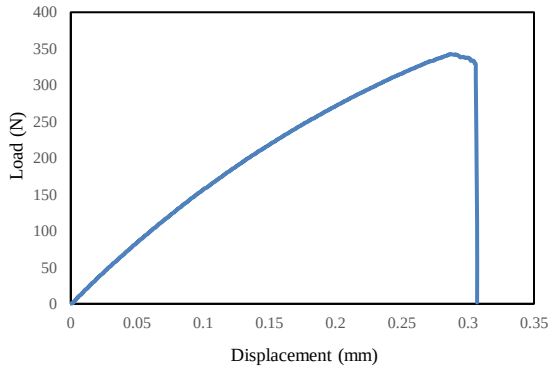

(c) Heating temperature 130 C

Figure 3.6 Continued

Table 3. 4 Variation of shear strength under different heating temperatures at holding time of 75 min and constant pressure

Heating temperature (Celsius）	130 C	140 C	150 C
Shear strength (MPa)	0.617	0.931	1.037

Figure 3.7 demonstrates the load-displacement curve for lap-shear specimens at 140 C and constant pressure held for different time. It can be observed that with a decrease of heating time, the shear strength also decreases due to the less diffusion of polymer chains. It can be also seen that debonding occurs gradually as the load drops

gradually before the specimen is fully debonded. Table 3.5 demonstrates the shear strength increases with the increase of holding time, as the shear strength is 0.768 MPa when the holding time is 45 min, 0.931 MPa for 75 min, and 1.027 MPa for 105 min.

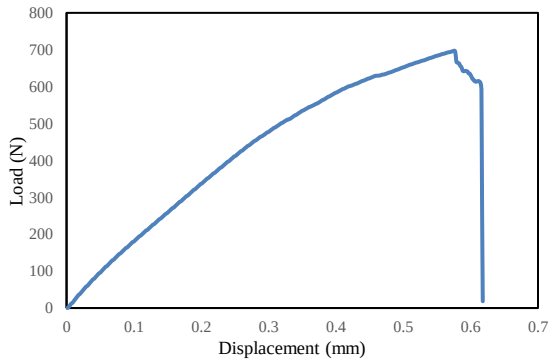

(a) Held for 105 min

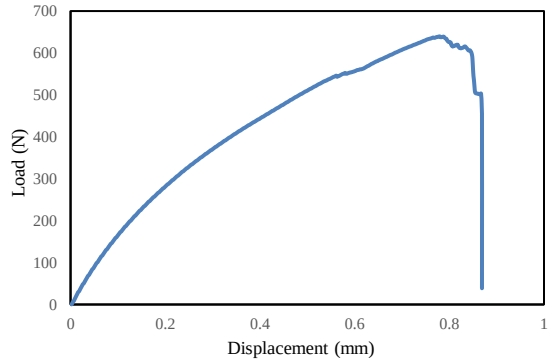

(b) Held for 75 min

Figure 3. 7 Load versus displacement plot for lap-shear specimen under 140 C held for (a) 105 min (b) 75 min (c) 45 min

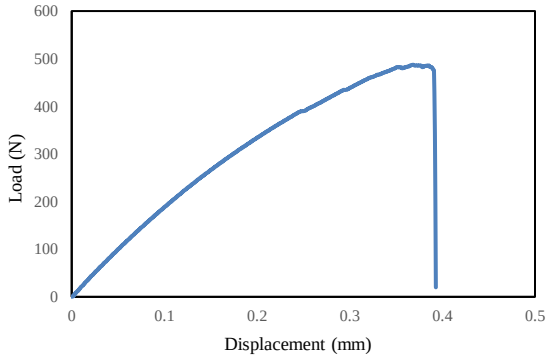

(c) Held for 45 min

Figure 3.7 Continued

Table 3. 5 Variation of shear strength under different heating time

at heat temperature of 140 C and constant pressure

Heating time (min)	45 min	75 min	105 min
Shear strength (MPa)	0.768	0.931	1.027

3.2 Fabrication and Characterization of FGPMs

The fabrication of FGPMs with different configurations using the thermo-bonding process and adhesive bonding process is presented in this section. In Section 3.2.1, specimen configurations are described. The configurations were chosen properly

not only for demonstrating the feasibility of lamination process in fabricating different structures, but also for validating the analytical and numerical models derived in Section 4. The detailed lamination process is presented and the processed samples are shown in Section 3.2.2. In Section 3.2.3, characterization of laminated FGPMs through the compression tests are presented, and the experimental results and summary are also provided.

3.2.1 Specimen Configurations

In order to fully investigate the mechanical properties of FGPMs and demonstrate the feasibility of thermal-induced lamination process, eight different configurations of specimens were fabricated, including the combination of open cell and closed cell structure with different void geometries and porosity gradient, i.e. constant porosity, and gradient porosity. The specimen matrix is demonstrated in Table 3.6. As can be seen, Configurations 1-4 deal with the closed cell problem, while the rest of the configurations were designed as open cell structures. Odd layers were designed for closed cell structures in order to ensure that the voids are all enclosed as can be seen in Configurations 1-4. Round disk void and square disk void were selected in order to study the effects of different pore geometries on the mechanical property of FGPMs. As a

comparison to gradient structure, materials with constant porosity were also fabricated and their mechanical responses were studied. The overall porosity of all the specimen configurations was kept below 40% as this work is mainly focused on fabrication and modeling of FGPMs with low-to-medium porosity.

Table 3. 6 Specimen matrix for different configurations

	Geometry			# of layer	Overall porosity	Void arrangement
Configuration 1	Closed cell	Round disk void	Constant porosity	9	12.60%	void alignment
Configuration 2	Closed cell	Square disk void	Constant Porosity	9	12.64%	void alignment
Configuration 3	Closed cell	Round disk void	Graded porosity	9	12.15%	void alignment
Configuration 4	Closed cell	Square disk void	Graded porosity	17	11.73%	void alignment
Configuration 5	Open cell	Round disk void	Constant Porosity	8	32.71%	half diameter shift
Configuration 6	Open cell	Square disk void	Constant Porosity	8	35.67%	half diameter shift
Configuration 7	Open cell	Round disk void	Graded porosity	8	24.20%	void alignment
Configuration 8	Open cell	Square disk void	Graded porosity	16	24.92%	void alignment

Figures 3.8 and 3.9 demonstrate the single-layers with round disk void and square disk void for Configurations 1 and 2, respectively. The detailed geometrical

information for closed cell configurations are shown in Tables 3.7– 3.10. For Configuration 1 as shown in Table 3.7, since it is a closed cell structure, Layer #1, #3, #5, #7, and #9 are all solid layers while Layer #2, #4, #6 and #8 are identical porous layers. Each layer contains 5×5 round disk with a pore diameter of ∅3.4 mm. Similar to Configuration 1, Configuration 2 has the same layer setting except the pores are square disk void with side length of 3.2 mm as shown in Table 3.8. Configuration 3 is associated with closed cell graded round disk, where Layer #2, #4, #6, and #8 have different pore diameters and porosities as shown in Table 3.9. As can be observed from Table 3.10, Configuration 4 contains 17 layers with 8 different porosities. In each layer, 6×6 square disk voids are included.

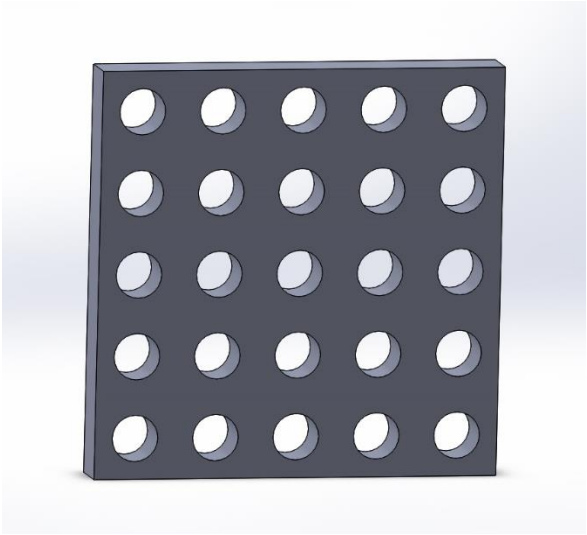

Figure 3. 8 Porous single layer for Configuration 1

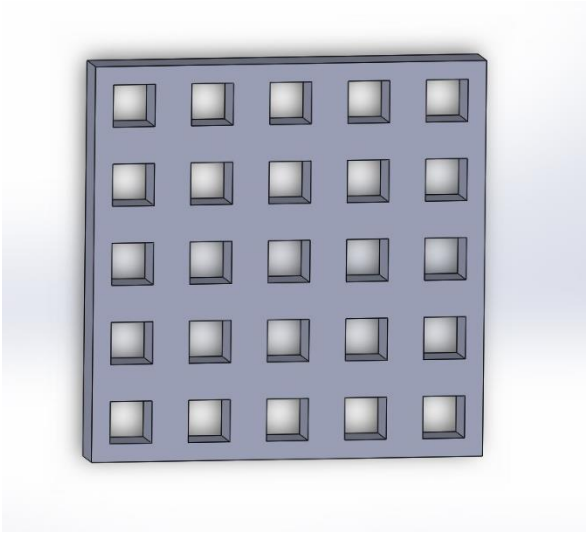

Figure 3. 9 Porous single layer for Configuration 2

Table 3. 7 Geometrical information for Configuration 1

	Description	Porosity	Layer size (mm)	Pore size (mm)
Layer #1, #3, #5, #7, #9	Solid layer	0.00%	6×6×3.5	N/A
Layer #2, #4, #6, #8	Porous layer	25.20%	6×6×3.5	∅ 3.4×3.5

Table 3. 8 Geometrical information for Configuration 2

	Description	Porosity	Layer size (mm)	Pore size (mm)
Layer #1, #3, #5, #7, #9	Solid layer	0.00%	6×6×3.5	N/A
Layer #2, #4, #6, #8	Porous layer	28.44%	6×6×3.5	3.2×3.2×3.5

Table 3. 9 Geometrical information for Configuration 3

	Description	Porosity	Layer size (mm)	Pore size (mm)
Layer #1, #3, #5, #7, #9	Solid layer	0.00%	6×6×3.5	N/A
Layer #2	Porous layer	14.74%	6×6×3.5	∅ 2.6×3.5
Layer #4	Porous layer	28.26%	6×6×3.5	∅ 3.6×3.5
Layer #6	Porous layer	31.48%	6×6×3.5	∅ 3.8×3.5
Layer #8	Porous layer	34.89%	6×6×3.5	∅ 4.0×3.5

Table 3. 10 Geometrical information for Configuration 4

	Description	Porosity	Layer size (mm)	Pore size (mm)
Layer #1, #3, #5, #7,#9, #11, #13, #15, #17	Solid layer	0.00%	4×4×1.5	N/A
Layer #2	Porous layer	5.06%	4×4×1.5	0.9×0.9×1.5
Layer #4	Porous layer	10.56%	4×4×1.5	1.3×1.3×1.5
Layer #6	Porous layer	16.00%	4×4×1.5	1.6×1.6×1.5
Layer #8	Porous layer	22.56%	4×4×1.5	1.9×1.9×1.5
Layer #10	Porous layer	27.56%	4×4×1.5	2.1×2.1×1.5
Layer #12	Porous layer	33.06%	4×4×1.5	2.3×2.3×1.5
Layer #14	Porous layer	39.06%	4×4×1.5	2.5*2.5*1.5
Layer #16	Porous layer	45.56%	4×4×1.5	2.7*2.7*1.5

Configurations 5-8 are designed as open cell structures. Configurations 5 and 7 contain round disk voids, while Configurations 6 and 8 deal with square disk void. Tables 3.11 and 3.12 show the geometrical information for Configurations 5 and 6. Note that in order to maintain the interconnected open cell structure, Layers #2, #4, #6, and #8 were designed to shift a half diameter to the right compared to Layer #1, #3, #5, and #7, respectively. Configurations 7 and 8 have eight different layers with different porosity through the graded direction as shown in Tables 3.13-3.15.

The individual single layers were carefully examined and measured after 3-D printing to make sure that the dimensional accuracy is within the tolerance of 0.4 mm.

Table 3. 11 Geometrical information for Configuration 5

	Description	Porosity	Layer size (mm)	Pore size (mm)
Layer #1, #3, #5, #7	Porous layer	32.71%	6×6×4	∅ 4×4
Layer #2, #4, #6, #8	Porous layer, pores shift a half diameter to the right	32.71%	6×6×4	∅ 4×4

Table 3. 12 Geometrical information for Configuration 6

	Description	Porosity	Layer size (mm)	Pore size (mm)
Layer #1, #3, #5, #7	Porous layer	35.67%	6.5×6.5×4	4×4×4
Layer #2, #4, #6, #8	Porous layer, pores shift a half diameter to the right	35.67%	6.5×6.5×4	4×4×4

Table 3. 13 Geometrical information for Configuration 7

	Description	Porosity	Layer size (mm)	Pore size (mm)
Layer #1	Porous layer	14.74%	6×6×3.5	∅2.6×3.5
Layer #2	Porous layer	17.10%	6×6×3.5	∅2.8×3.5
Layer #3	Porous layer	19.63%	6×6×3.5	∅3.0×3.5
Layer #4	Porous layer	22.33%	6×6×3.5	∅3.2×3.5
Layer #5	Porous layer	25.21%	6×6×3.5	∅3.4×3.5
Layer #6	Porous layer	28.26%	6×6×3.5	∅3.6×3.5
Layer #7	Porous layer	31.49%	6×6×3.5	∅3.8×3.5
Layer #8	Porous layer	34.89%	6×6×3.5	∅4.0×3.5

Table 3. 14 Geometrical information for Configuration 8

	Description	Porosity	Layer size (mm)	Pore size (mm)
Layer #1	Porous layer	5.06%	4×4×3	0.9×0.9×3
Layer #2	Porous layer	10.56%	4×4×3	1.3×1.3×3
Layer #3	Porous layer	16.00%	4×4×3	1.6×1.6×3
Layer #4	Porous layer	22.56%	4×4×3	1.9×1.9×3
Layer #5	Porous layer	27.56%	4×4×3	2.1×2.1×3
Layer #6	Porous layer	33.06%	4×4×3	2.3×2.3×3
Layer #7	Porous layer	39.06%	4×4×3	2.5×2.5×3
Layer #8	Porous layer	45.56%	4×4×3	2.7×2.7×3

3.2.2 Lamination Processes

Thermally induced lamination process

As mentioned previously, FGPMs samples were prepared under the thermo-compression process. In order to ensure the best mechanical properties as well as strong shear strength of bonding, heating temperature of Tm-10 C with holding time 75 min under constant pressure was chosen. As mention above, the constant pressure was achieved by using an aluminum spacer which has high elastic modulus compared to

PLA, and can prevent the upper die from moving down to deform the layered FGPMs further; thus, the constant pressure during the experiment can be maintained.

Adhesive bonding process

As an alternative, adhesive bonding was also used to laminate the FGPMs. In this work, Loctite® Super Glue Liquids was chosen to create bond between the layers. The adhesive is a fast acting cyanoacrylate which is ideal for quickly forming of strong bonds between non-absorbent materials in harsh conditions with pinpoint accuracy [140]. The cyanoacrylate adhesive is formulated with additives such as rubber or fumed silica in order to increase shear strength and generate impact resistant bond. The material has low viscosity and can be easily applied evenly on the surface of samples to form a very thin adhesive layer.

Before the application of adhesive, the surfaces of samples were carefully cleaned with CSM Degreaser in order to remove any oil or contaminant. The surfaces were then carefully dried with a gauze sponge. In addition, any burs due to 3-D printing would be removed to ensure the surface-surface contact when applying the adhesion. In order to avoid surface contamination, the cleaned single layer samples were bonded within 30 min after the surface cleaning.

After evenly applying the adhesive on the surface of single layer, the bonded layers are pressed together and held in place for 20 seconds. For full bond strength, the parts would be left for 24 hours to cure before being tested for mechanical property.

Laminated samples

Specimens were obtained for each configuration using the above lamination processes. The open cell FGPMs for Configuration 8 obtained through the thermo-bonding at 10 C below Tm of PLA and were held for 75 min is shown in Figure 3.10 (a) and (b). The sizes of pores are gradually changed in the layer built-up direction, as can be observed that the square disk voids in the top layer (Figure 3.10 (a)) are smaller than that in bottom layer (Figure 3.10 (b)). Due to the preloading condition in the thermo-bonding process, the layers are in close contact with the neighboring layers. It is also observed that the original pore sizes are maintained since the material were kept in solid-state, and there was no plastic deformation occurred during the lamination process.

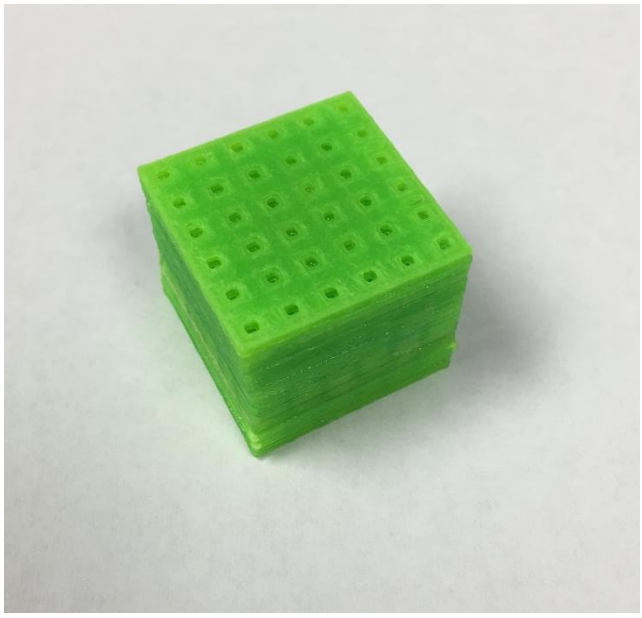

(a) FGPM sample view from the top layer

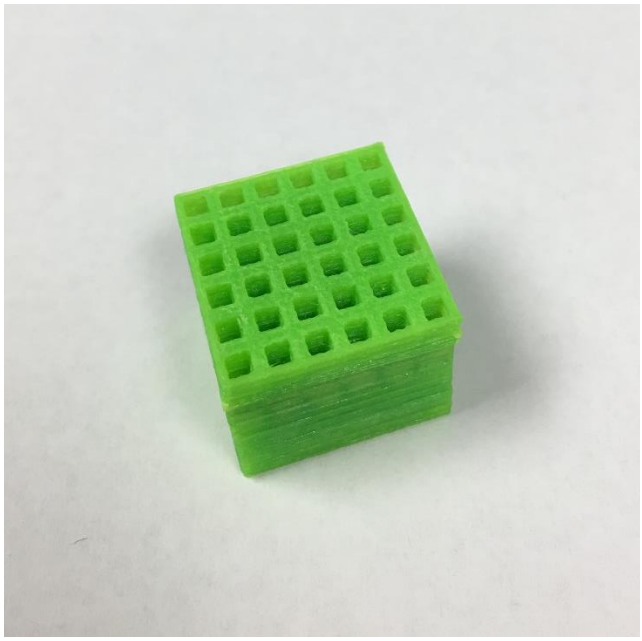

(b) FGPM sample view from the bottom layer

Figure 3. 10 FGPM sample prepared from thermal bonding process

Figure 3.11 shows the closed cell FGPMs for Configuration 3 obtained through adhesive bonding process. Since it is a closed cell structure, the sample was laminated as one layer solid and one layer porous alternatively, and all the round disk voids were enclosed inside. During the lamination process, the adhesive dwells on the surface of the single-layers, thus, the material property of 3-D printed PLA was maintained.

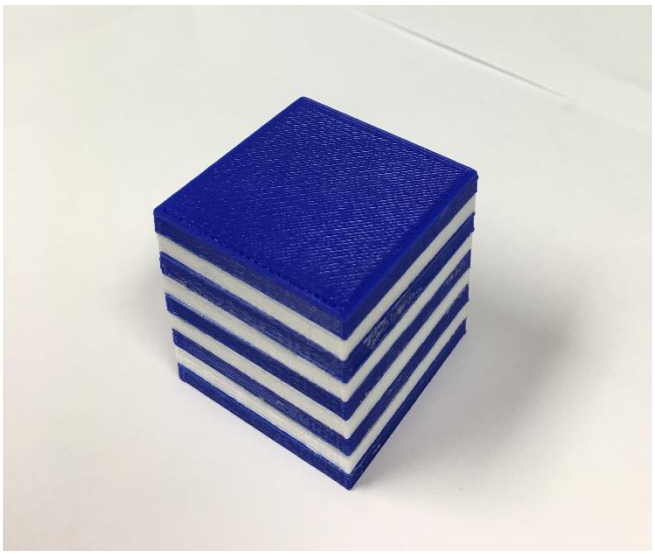

Figure 3. 11 FGPM sample prepared from adhesive bonding process

Once the samples were prepared, mechanical tests are performed in order to characterize the mechanical property of fabricated FGPMs.

3.2.3 Characterization of Laminated FGPMs

The laminated FGPMs specimens were characterized using the compression tests in the layer built-up direction (Direction 3) and transverse direction (Direction 1 and Direction 2, directions perpendicular to the built-up direction). As can be seen from Tables 3.7 to 3.14, the specimens can be considered as pseudo – transversely isotropic material where the compressive properties are equal in Direction 1 and Direction 2 ($E_{11} = E_{22}$). The compression tests were aimed at evaluating the compression behavior and measuring the effective modulus of the FGPMs, as well as at validating the analytical and numerical models developed in the following section.

Experimental procedure for compression test

The compression tests were carried out using MTS Insight® Electromechancial testing systems with load capacity of 30 KN. The experiments were performed at room temperature at a constant speed of the crosshead at 0.5 mm/min for all the tests. Strain endpoint of the specimen was set as 9% before tests stop to ensure the elastic behavior is fully covered. Four repetitive tests were conducted per condition, as such, for each configuration listed in Table 3.6, eight samples were tested in normal and transverse

compression tests. Solid 3-D printed specimens are also tested in order to acquire the material property of base material, since the 3-D printed material may have different mechanical response from raw material [141]. Figure 3.12 demonstrates the experimental set-up for the compression tests. The specimen geometry and porosity are depicts in Tables 3.7 to 3.14. The load-displacement data were exported after the experiments, and the stress-strain relations are calculated.

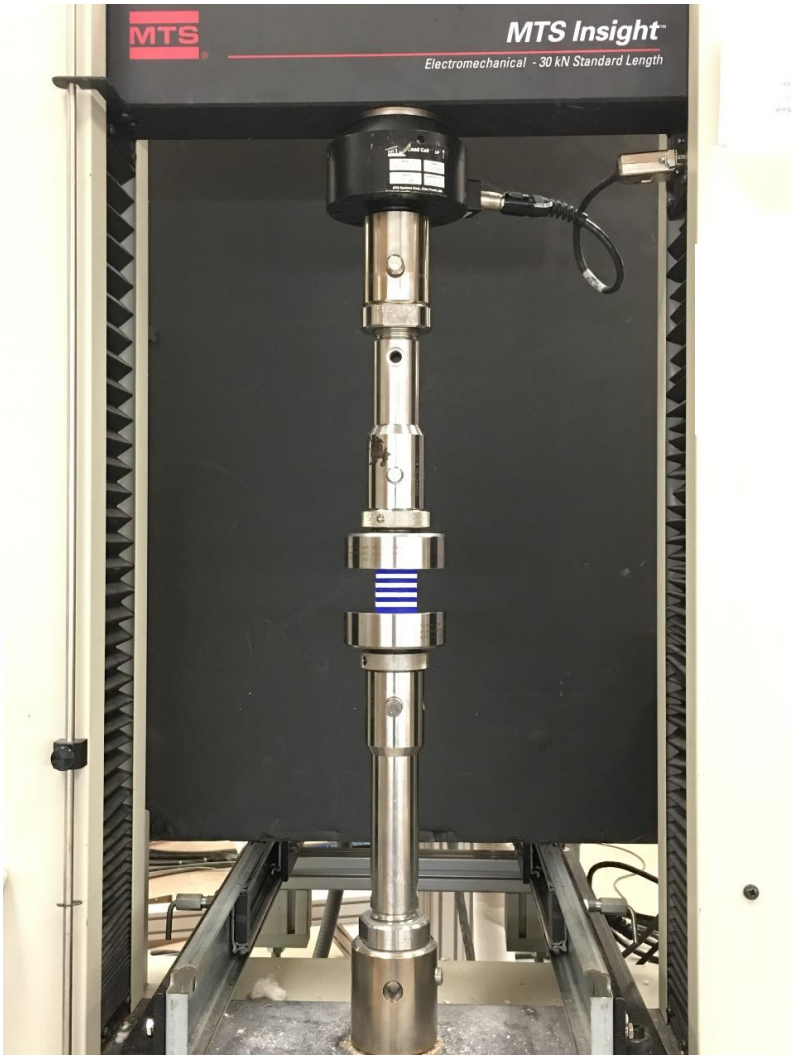

Figure 3. 12 Experimental set-up for the compression test

Experimental results for compression test

The mechanical response of the 3-D printed PLA was first characterized using the compression tests as shown in Figure 3.13. The elastic modulus of 3-D printed PLA

was found to be 986.27 MPa. Compared to the elastic modulus of raw (filament) PLA of 3.5 GPa, it can be seen that there is a significant difference in material property between 3-D printed material and raw material, and the former strongly depends on printing parameters, such as the percentage of infill, the width of filament, layer thickness, etc.

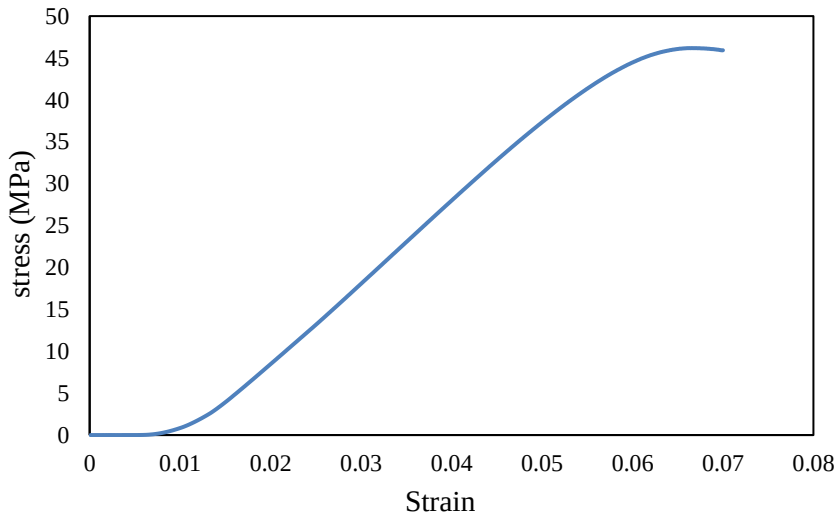

Figure 3. 13 Stress-strain behavior of 3-D printed PLA in compression test

Figures 3.14 to 3.17 demonstrate the compression engineering stress versus strain plots for a specimen with square disk voids, i.e. Configurations 2,4,6,8, in build-up direction and transverse direction. The strain was calculated by the displacement of cross head divided by initial specimen thickness. It is observed that the initial slopes of the stress-strain curve are small, indicating that the materials are densified by compressive

load. The curve is linear in the elastic deformation in all the curves, and the effective moduli were calculated as the slopes of linear part of the stress-strain curves.

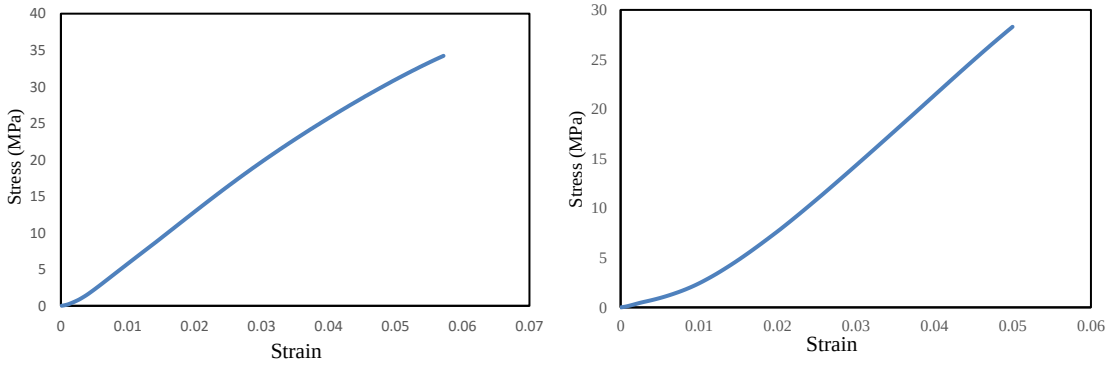

(a) (b)

Figure 3. 14 Stress versus strain plot for closed cell constant square disk void in (a) normal direction (b) transverse direction

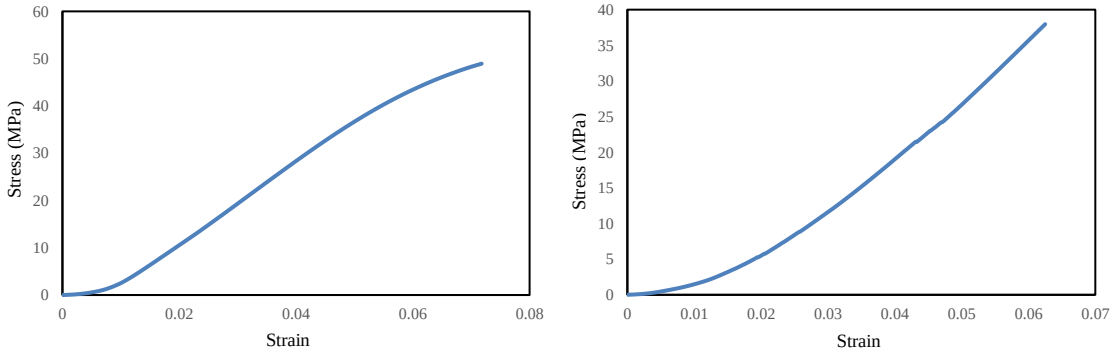

(a) (b)

Figure 3. 15 Stress versus strain plot for closed cell graded square disk void in the (a) normal direction (b) transverse direction

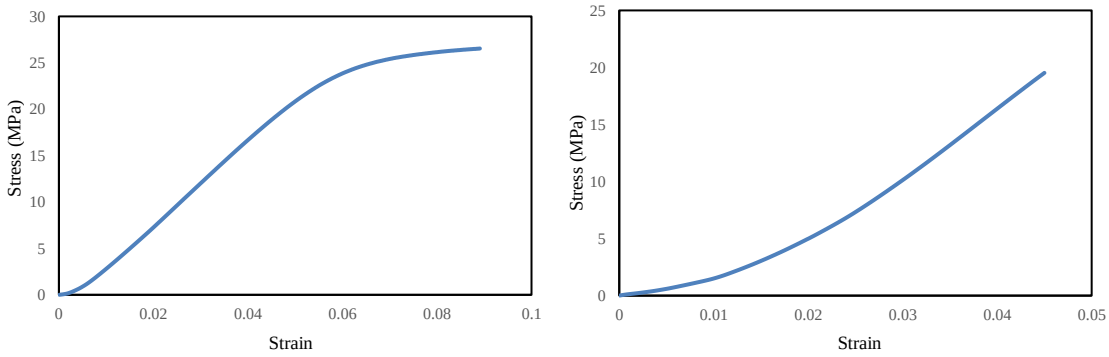

(a) (b)

Figure 3. 16 Stress versus strain plot for open cell constant square disk void in the

(a) normal direction (b) transverse direction

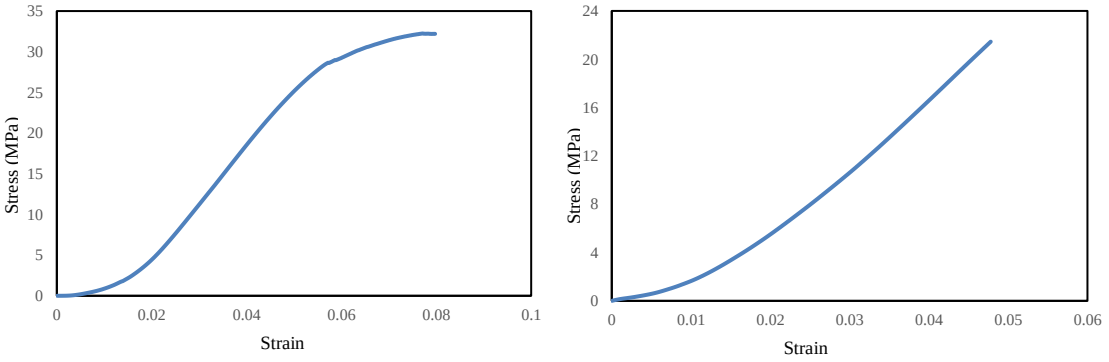

(a) (b)

Figure 3. 17 Stress versus strain plot for open cell graded square disk void in the

(a) normal direction (b) transverse direction

Tables 3.15 to 3.18 show the effective moduli for each configuration. Each value is calculated from the average of four repetitive tests. E_{33} denotes the modulus in the layer built-up direction, and E_{11} denotes the modulus in the direction perpendicular to the E_{33} direction. Normalized effective moduli were calculated as the effective stiffness divided by the elastic modulus of the base material, which is 986.27 MPa in this case. ν_2 indicates the overall porosity of each configuration. It is observed that the effective modulus is related to the porosity. Overall, an increase of the porosity will result in a decrease of the effective modulus. However, the relationship might not be necessarily linear. The shape and the location of the voids and the porosity distribution also affect the effective modulus as will be shown in the next section. The experimental data are later used to verify the prediction accuracy of the developed analytical and numerical model.

Table 3. 15 Effective moduli for closed cell round disk voids

	Round disk void_constant (Configuration 1) ν_2=12.6%		Round disk void_graded (Configuration 3) ν_2=12.15%	
	Effective stiffness data (MPa)	Normalized effective stiffness	Effective stiffness data (MPa)	Normalized effective stiffness
E33	593.298	0.602	721.160	0.731
E11	571.156	0.579	759.170	0.770

Table 3. 16 Effective moduli for closed cell square disk voids

	Square disk void_constant (Configuration 2) ν_2=12.64%		Square disk void_graded (Configuration 4) ν_2=11.73%	
	Effective stiffness data (MPa)	Normalized effective stiffness	Effective stiffness data (MPa)	Normalized effective stiffness
E33	698.366	0.708	859.310	0.871
E11	721.235	0.731	788.952	0.800

Table 3. 17 Effective moduli for open cell round disk voids

	Round disk void_constant (Configuration 5) ν_2=32.71%		Round disk void_graded (Configuration 7) ν_2=24.2%	
	Effective stiffness data (MPa)	Normalized effective stiffness	Effective stiffness data (MPa)	Normalized effective stiffness
E33	571.385	0.579	551.488	0.559
E11	469.948	0.477	583.844	0.592

Table 3. 18 Effective moduli for open cell square disk voids

	Square disk void_constant (Configuration 6) ν_2=35.67%		Square disk void_graded (Configuration 8) ν_2=24.92%	
	Effective stiffness data (MPa)	Normalized effective stiffness	Effective stiffness data (MPa)	Normalized effective stiffness
E33	472.926	0.480	711.312	0.721
E11	634.676	0.644	614.837	0.623

4. ANALYTICAL AND NUMERICAL MODELING OF FUNCTIONALLY GRADED POROUS MATERIALS

In Section 4, analytical model and numerical model are established for functionally graded porous materials (FGPMs). The model are then implemented and the predictions are compared with experimental results from Section 3. Section 4.1 describes the existing analytical models for obtaining the material properties of composites, and their accuracy in predicting the mechanical behavior of FGPMs is examined.

In Section 4.2, analytical model derivation for FGPMs based on Mori-Tanaka scheme is elaborated. The Mori-Tanaka's model is extended to graded and porous materials with the consideration of volume change of pores.

Section 4.3 deals with open-cell structure, and an application of Mori-Tanaka's model to open-cell structure is presented. The disturbed stress fields outside the cavity for isotropic and anisotropic material are used to deliver analytical solutions for open-cell structure.

Section 4.4 demonstrates the application of the derived analytical model to obtain mechanical properties of FGPMs. The model is used to predict both open cell and closed cell structures with different pore shapes.

Numerical modeling of FGPMs is discussed in Section 4.5. In the model, representative volume element (RVE) is used and periodic boundary condition (PBC) is applied on RVE.

4.1 Overview of Analytical Models of Composite Materials

Efforts have been taken to develop analytical models for composite materials, and overview of available analytical models using micromechanics approach is provided in this section.

In Section 4.1.1, Eshelby's inclusion problem and Eshelby's equivalent inclusion problem are elaborated. In Section 4.1.2, the response of RVE under homogeneous boundary conditions is discussed. The stress-strain relationship for elastic materials is briefly described in Section 4.1.3. In Section 4.1.4, the averaging stress and strain theorem is presented, followed by a description of effective elastic moduli in Section 4.1.5. Section 4.1.6 presents the well-known Mori-Tanaka's model, which is an effective field approximation based on Eshelby's equivalent inclusion model. An evaluation of Mori-Tanaka's model in predicting the effective stiffness of FGPMs is conducted in Section 4.1.7.

4.1.1 Eshelby's Tensor for Composite Materials

Significant efforts have been made to study and predict the effective properties of composite materials. Most of the developed analytical models are based on micromechanics methods. Homogenization process is generally employed to analyze the mechanical behavior of composite material based on the geometries and properties of individual constituents [122]. Some of the most commonly used models include: rule of mixture, Chamis model, Halpin-Tsai model, Differential scheme, self-consistent model/generalized self-consistent model, and Mori-Tanaka method.

It is reported that each model has its specific applicability and limitations. Self-consistent model and Mori-Tanaka model are two models that consider the interactions between the inclusions. It was shown that the self-consistent scheme yields more accurate prediction results for skeletal microstructure with a relatively wide matrix-inclusion transition zone, while Mori-Tanaka method is a better prediction scheme for obtaining the effective properties with a "well-defined" continuous medium and discontinuous inclusions [1]. Both models are based on Eshelby's equivalent inclusion method that provides the stress and strain relationship inside and outside of the inhomogeneity.

In Eshelby's inclusion problem, an infinite linear elastic solid body with volume

V contains an inclusion with a sub-volume V_0 and surface area S_0 is considered as shown in Figure 4.1. The material inside V_0 is called an inclusion with its elastic properties L_{ijkl} the same as the outside matrix. Now the inclusion is subjected to a permanent deformation with a uniform eigenstrain ε_{ij}^{*}, which caused by thermal expansion or phase transformation. Here the eigenstrain ε_{ij}^{*} refers to the strain under stress free state. Eshelby solved this problem through a "thought experiment" [142]. The first step is to assume the removal of the inclusion out from the matrix. Both the matrix and inclusion undergo stress free state, while inclusion subjects to eigenstrain ε_{ij}^{*} as shown in Figure 4.2 (a) and Table 4.1(a). The second step involved straining the inclusion back to its original shape by applying surface traction T to it, which also means that the eigenstrain is cancelled exactly by the reshaping strain ε_{ij}^{re} in this step. Now the stress of inclusion is $\sigma_{ij} = L_{ijkl}\varepsilon_{ij}^{re}$. The stress and strain state in the matrix and inclusion is shown in Figure 4.2 (b) and Table 4.1(b). In the third step, simply put the inclusion back to the matrix without releasing applied force, thus the stress and strain state stays the same as the third step as shown in Figure 4.2 (c) and Table 4.1 (c). The applied surface traction is then removed in the fourth step in which become the same condition as the original problem. The process is obtained by applying a surface traction F to the inclusion which cancels the stress T applied in step (2) and step (3). The material responses to the surface traction F by forming equal displacement or strain ε_{ij}^{p} in the

matrix and inclusion. ε_{ij}^{p} is also called perturbation strain which refers to the perturbation of the inclusion compared to a pure linear elastic body without inclusion. Therefore, the stress inside of the inclusion is $\sigma_{ij} = L_{ijkl}(\varepsilon_{kl}^{p} - \varepsilon_{kl}^{*})$ as shown in Figure 4.2 (d) and Table 4.1 (d).

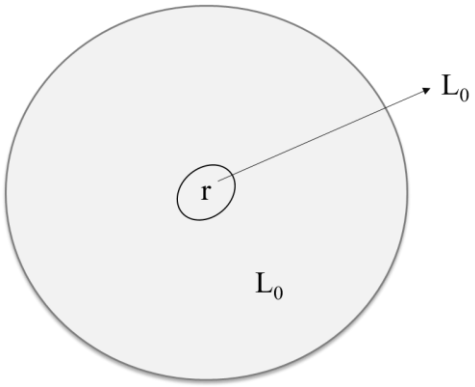

Figure 4. 1 Eshelby's inclusion problem

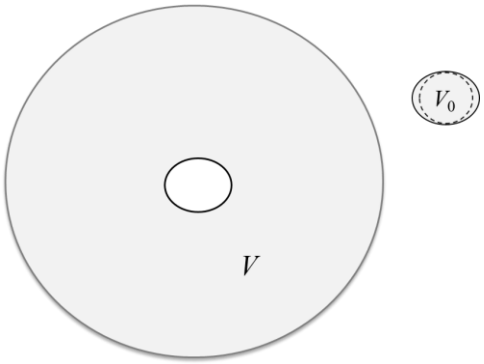

(a) Eshelby's inclusion problem – step 1

Figure 4. 2 Solution steps for Eshelby's inclusion problem [142]

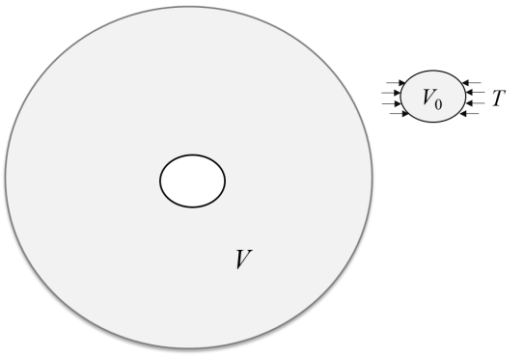

(b) Eshelby's inclusion problem – step 2

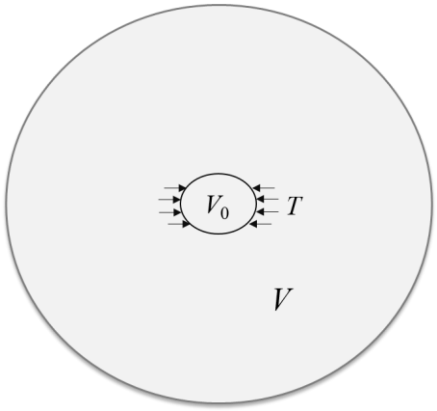

(c) Eshelby's inclusion problem – step 3

Figure 4.2 Continued

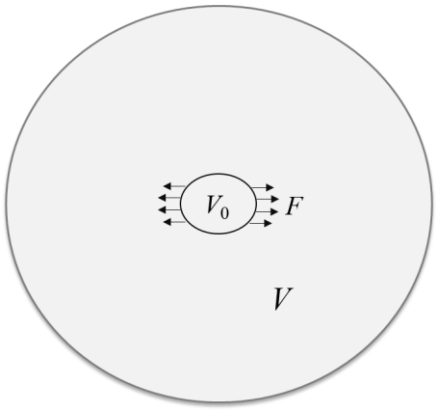

(d) Eshelby's inclusion problem – step 4

Figure 4.2 Continued

Table 4. 1 Stress and strain in matrix and inclusion for Eshelby's inclusion problem

Matrix	Inclusion
$\varepsilon_{ij} = 0$	$\varepsilon_{ij} = \varepsilon_{ij}^{*}$
$\sigma_{ij} = 0$	$\sigma_{ij} = 0$

(a) Stress and strain in matrix and inclusion for step 1

Matrix	Inclusion
$\varepsilon_{ij} = 0$	$\varepsilon_{ij} = \varepsilon_{ij}^{re} + \varepsilon_{ij}^{*} = 0$
$\sigma_{ij} = 0$	$\sigma_{ij} = L_{ijkl}\varepsilon_{ij}^{re} = -L_{ijkl}\varepsilon_{ij}^{*} = -\sigma_{ij}^{*}$

(b) Stress and strain in matrix and inclusion for step 2

Table 4.1 Continued

Matrix	Inclusion
$\varepsilon_{ij} = 0$	$\varepsilon_{ij} = \varepsilon_{ij}^{re} + \varepsilon_{ij}^{*} = 0$
$\sigma_{ij} = 0$	$\sigma_{ij} = L_{ijkl}\varepsilon_{ij}^{re} = -L_{ijkl}\varepsilon_{ij}^{*} = -\sigma_{ij}^{*}$

(c) Stress and strain in matrix and inclusion for step 3

Matrix	Inclusion
$\varepsilon_{ij} = \varepsilon_{ij}^{p}$	$\varepsilon_{ij} = \varepsilon_{ij}^{p}$
$\sigma_{ij} = \sigma_{ij}^{p}$	$\sigma_{ij} = \sigma_{ij}^{p} - \sigma_{ij}^{*} = L_{ijkl}(\varepsilon_{kl}^{p} - \varepsilon_{kl}^{*})$

(d) Stress and strain in matrix and inclusion for step 4

Eshelby [106] showed that the perturbed strain of the inclusion ε_{ij}^{p} can be directly related to its eigenstrain ε_{ij}^{*} by introducing a fourth order tensor S_{ijkl}, where

$$\varepsilon_{ij}^{p} = S_{ijkl}\varepsilon_{kl}^{*} \tag{4. 1}$$

The tensor S_{ijkl} is called Eshelby's tensor. He also demonstrated that the Eshelby's tensor is a constant tensor in the case of an ellipsoidal inclusion enclosed in an infinite and homogeneous medium. It only depends on the inclusion property and geometry, and the stress and eigenstrain inside the inclusion is uniform. However, in some particular cases, as will be shown later, it is a function of coordinate in space.

An inhomogeneity is defined as a sub-volume V_0 in an infinite large linear elastic

solid body V with its elastic property L'_{ijkl} different from matrix L_{ijkl} as shown in Figure 4.3. In order to investigate the stress-strain state inside the inhomogeneity when it is subjected to a permanent deformation with eigenstrain $\varepsilon^{*'}_{ij}$, an Eshelby's equivalent inclusion approach is used. In this method, a proper eigenstrain of the inclusion is chosen in order to satisfy the condition that the elastic stress and strain fields inside the inhomogeneity are equal to the corresponding elastic stress and strain fields inside the equivalent inclusion.

Inside of the inhomogeneity, the stress is expressed as:

$$\sigma^{I'}_{ij} = \sigma^{p'}_{ij} - \sigma^{*'}_{ij} = L'_{ijkl}(\varepsilon^{p'}_{kl} - \varepsilon^{*'}_{kl}) \tag{4. 2}$$

which equals the stress inside the equivalent inclusion:

$$\sigma^{I}_{ij} = \sigma^{p}_{ij} - \sigma^{*}_{ij} = L_{ijkl}(\varepsilon^{p}_{kl} - \varepsilon^{*}_{kl}) \tag{4. 3}$$

Since the total strain inside the inhomogeneity is equal to that inside the equivalent inclusion, which gives:

$$\varepsilon^{p'}_{kl} = \varepsilon^{p}_{kl} \tag{4. 4}$$

Combine Eq. (4.1) and Eq. (4.2), and substitute to Eq. (4.3) gives:

$$L'_{ijkl}(\varepsilon^{p}_{kl} - \varepsilon^{*'}_{kl}) = L_{ijkl}(\varepsilon^{p}_{kl} - \varepsilon^{*}_{kl}) \tag{4. 5}$$

From Eq. (4.5), it is seen that the by applying equivalent inclusion problem and properly choosing equivalent eigenstrain, the stress strain state of inhomogeneity can be solved.

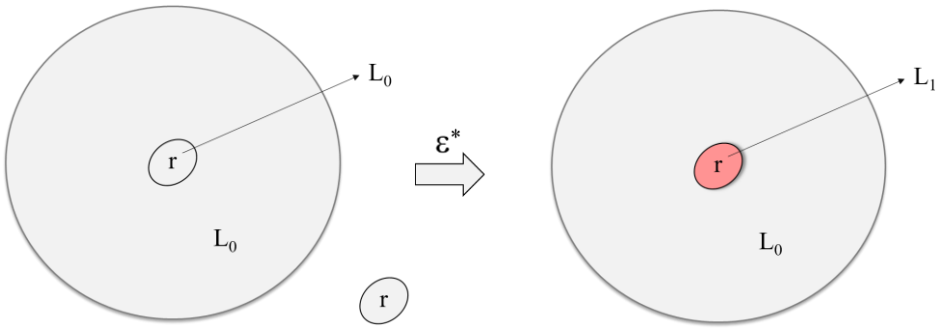

(a) Matrix without inhomogeneity (b) Matrix with the perturbation of inhomogeneity

Figure 4. 3 Eshelby's equivalent inclusion problem

Now considering another inhomogeneity problem that is widely used in micromechanics to obtain the effective stiffness for composite material. In this case, the inhomogeneity is embedded in an infinite linear elastic solid body, instead of undergo an eigenstrain, a uniform external load is applied to the whole body. The stress inside the inhomogeneity is the superposition of two responses: the first is the response to the external load:

$$\sigma_{ij}^{0'} = L_{ijkl}^{'} \varepsilon_{kl}^{0'} \tag{4. 6}$$

where $\sigma_{ij}^{0'}$ and $\varepsilon_{kl}^{0'}$ denote the stress and strain of the inhomogeneity under the external load without considering the perturbation effect.

The second response considers the perturbation effect of inhomogeneity, whereas

the perturbed stress can be expressed as:

$$\sigma_{ij}^{p'} = L_{ijkl}^{'} \varepsilon_{kl}^{p'} \tag{4. 7}$$

Since no eigenstrain is involved inside the inhomogeneity, the total elastic stress inside the inhomogeneity can be expressed as:

$$\sigma_{ij}^{I'} = \sigma_{ij}^{0'} + \sigma_{ij}^{p'} = L_{ijkl}^{'} (\varepsilon_{kl}^{0'} + \varepsilon_{kl}^{p'}) \tag{4. 8}$$

where $\sigma_{ij}^{I'}$ denotes the stress in the inhomogeneity.

On the other hand, by applying the equivalent inclusion method, the stress-strain state inside the equivalent inclusion can expressed as:

$$\sigma_{ij}^{I} = \sigma_{ij}^{0} + \sigma_{ij}^{p} - \sigma_{ij}^{*} = L_{ijkl} (\varepsilon_{kl}^{0} + \varepsilon_{kl}^{p} - \varepsilon_{kl}^{*}) \tag{4. 9}$$

where σ_{ij}^{0}, σ_{ij}^{p}, and σ_{ij}^{*} denote the stresses due to external applied load, perturbation effect of inhomogeneity, and equivalent eigenstrain, respectively; ε_{kl}^{0}, ε_{kl}^{p}, and ε_{kl}^{*} denote the strains due to external applied load, perturbation effect of inhomogeneity, and equivalent eigenstrain, respectively.

Similar to the previous inhomogeneity case, the stress and strain inside the inhomogeneity and equivalent inclusion should be equal, which gives:

$$L_{ijkl}^{'} (\varepsilon_{kl}^{0'} + \varepsilon_{kl}^{p'}) = L_{ijkl} (\varepsilon_{kl}^{0} + \varepsilon_{kl}^{p} - \varepsilon_{kl}^{*}) \tag{4. 10}$$

and

$$\varepsilon_{kl}^{0'} + \varepsilon_{kl}^{p'} = \varepsilon_{kl}^{0} + \varepsilon_{kl}^{p} \tag{4. 11}$$

And as discussed above, it was further demonstrated by Eshelby that

$$\varepsilon_{ij}^{p} = S_{ijkl} \varepsilon_{kl}^{*} \tag{4. 12}$$

where S_{ijkl} is a fourth order tensor called Eshelby's tensor.

4.1.2 Representative Volume Elements (RVEs) under Homogeneous Boundary Conditions

Representative volume elements (RVEs) is frequently used in studying the mechanics of composite material, when the composite material (1) is geometrically entirely typical of the whole material; (2) is large enough comparing to the microstructure scale, and includes a sufficient number of inhomogeneity or inclusions. An RVE is the element that retains and represents the material's apparent property of the composite because RVE does not depend on boundary values of displacement and traction when the materials are uniform in the macro scale [143]. In this work, RVE will be properly chosen for FGPMs and the RVE method will be used in the analytical model derivation and numerical modeling.

4.1.3 Stress-strain Relationships for Elastic Materials

The Hooke's law for elastic material used for RVEs is expressed as:

$$\sigma_{ij} = L_{ijkl}\varepsilon_{kl} \tag{4. 13}$$

where σ_{ij} denotes the stress component, ε_{kl} denotes the strain component, and L_{ijkl} denotes the elastic stiffness of the material.

Alternatively, the generalized Hooke's law relating strain to stress can be expressed as:

$$\varepsilon_{ij} = M_{ijkl}\sigma_{kl} \tag{4. 14}$$

where M_{ijkl} denotes the compliance tensor of the material, which is the inverse of the stiffness matrix L_{ijkl} .

Due to the existence of strain energy density, both the stiffness and compliance tensor are symmetric. Therefore, for the orthotropic material that has different material properties in three different perpendicular directions, the constitutive model is given by:

$$\begin{bmatrix} \varepsilon_{11} \\ \varepsilon_{22} \\ \varepsilon_{33} \\ 2\varepsilon_{23} \\ 2\varepsilon_{13} \\ 2\varepsilon_{12} \end{bmatrix} = \begin{bmatrix} C_{11} & C_{12} & C_{13} & 0 & 0 & 0 \\ C_{12} & C_{22} & C_{23} & 0 & 0 & 0 \\ C_{13} & C_{23} & C_{33} & 0 & 0 & 0 \\ 0 & 0 & 0 & C_{44} & 0 & 0 \\ 0 & 0 & 0 & 0 & C_{55} & 0 \\ 0 & 0 & 0 & 0 & 0 & C_{66} \end{bmatrix} \times \begin{bmatrix} \sigma_{11} \\ \sigma_{22} \\ \sigma_{33} \\ \tau_{23} \\ \tau_{13} \\ \tau_{12} \end{bmatrix} \tag{4. 15}$$

where C_{ij} denotes nonzero elastic constants. For orthotropic material, nine independent nonzero constants are needed to fully define the stiffness matrix. Alternatively, Eq. (4.15) can be rewritten in form of compliance tensor relating the strain and stress:

$$\begin{bmatrix} \varepsilon_{11} \\ \varepsilon_{22} \\ \varepsilon_{33} \\ 2\varepsilon_{23} \\ 2\varepsilon_{13} \\ 2\varepsilon_{12} \end{bmatrix} = \begin{bmatrix} \frac{1}{E_{11}} & -\frac{\nu_{21}}{E_{22}} & -\frac{\nu_{31}}{E_{33}} & 0 & 0 & 0 \\ -\frac{\nu_{12}}{E_{11}} & \frac{1}{E_{22}} & -\frac{\nu_{32}}{E_{33}} & 0 & 0 & 0 \\ -\frac{\nu_{13}}{E_{11}} & -\frac{\nu_{23}}{E_{22}} & \frac{1}{E_{33}} & 0 & 0 & 0 \\ 0 & 0 & 0 & \frac{1}{G_{23}} & 0 & 0 \\ 0 & 0 & 0 & 0 & \frac{1}{G_{13}} & 0 \\ 0 & 0 & 0 & 0 & 0 & \frac{1}{G_{12}} \end{bmatrix} \times \begin{bmatrix} \sigma_{11} \\ \sigma_{22} \\ \sigma_{33} \\ \tau_{23} \\ \tau_{13} \\ \tau_{12} \end{bmatrix} \quad (4.16)$$

where E_{ii} denotes the Young's modulus in i th direction, G_{ij} denotes the shear modulus in i - j direction, and ν_{ij} denotes Poisson's ratio which is negative ratio of transverse strains in the j th direction to the axial strain in i th direction when load is applied in the i th direction.

In this work, FGPMs described in Section 3 can be considered as orthotropic material, and the final results of analytical model for obtaining their effective modulus will be in the form of Eq. (4.15). For the graded material, it will be a combination of term for effective modulus and term for graded porosity.

4.1.4 Averaging Strain and Stress Theorem

For an RVE of composite subjected to macroscopically homogeneous stress or strain, the volume average stress and strain are expressed by:

$$\bar{\sigma}_{ij} = \frac{1}{V}\int_V \sigma_{ij} dV \tag{4. 17}$$

$$\bar{\varepsilon}_{ij} = \frac{1}{V}\int_V \varepsilon_{ij} dV \tag{4. 18}$$

where V is the volume of the RVE.

The average strain theorem shows that the average strain $\bar{\varepsilon}_{ij}$ is equal to macroscopic strain ε_{ij}^0 that applied on material for homogeneous boundary condition [144]. The strain – displacement relation is given by:

$$\varepsilon_{ij} = \frac{1}{2}(u_{i,j} + u_{j,i}) \tag{4. 19}$$

where u_i denotes the displacement in i direction.

Combine Eq. (4.18) and Eq. (4.19) based on two constituents yields:

$$\bar{\varepsilon}_{ij} = \frac{1}{2V}[\int_{V_1}(u_{i,j}^1 + u_{j,i}^1)dV + \int_{V_2}(u_{i,j}^2 + u_{j,i}^2)dV] \tag{4. 20}$$

where "1" and "2" refers to constituent 1 and constituent 2 of the composite, and V_1, V_2 denotes the volume of two phases. The well-known Gauss theorem is given by:

$$\int_V u_{i,j} dV = \int_S u_i n_j dS \tag{4. 21}$$

where n_j is the face normal in j direction.

Substitute Eq. (4.21) into Eq. (4.20) yields:

$$\bar{\varepsilon}_{ij} = \frac{1}{2V}[\int_{S_1}(u_i^1 n_j + u_j^1 n_i)dS + \int_{S_2}(u_i^2 n_j + u_j^2 n_i)dS] \tag{4. 22}$$

where S_1, S_2 are the boundary of constituent 1 and 2, respectively. On the interface of the two phases S_{12}, assuming a perfect contact, it follows:

$$u_i^1 = -u_i^2 \tag{4. 23}$$

Therefore in Eq. (4.22), the contributions from S_{12} in the two integrals on the right side cancel each other, which yields:

$$\bar{\varepsilon}_{ij} = \frac{1}{2V}\int_S (u_i n_j + u_j n_i) dS \tag{4. 24}$$

For composite subjected to homogeneous displacement boundary condition:

$$u_i(S) = \varepsilon_{ij}^0 x_j \tag{4. 25}$$

Substitute Eq. (4.25) into Eq. (4.24) gives:

$$\bar{\varepsilon}_{ij} = \varepsilon_{ij}^0 \tag{4. 26}$$

Similarly, the above derivation can be used to show that [144]:

$$\bar{\sigma}_{ij} = \sigma_{ij}^0 \tag{4. 27}$$

4.1.5 Effective Elastic Moduli

For composite material, the effective stiffness matrix L_{ijkl}^* and effective compliance matrix M_{ijkl}^* are defined as [144]:

$$\bar{\sigma}_{ij} = L_{ijkl}^* \bar{\varepsilon}_{kl} \tag{4. 28}$$

$$\bar{\varepsilon}_{kl} = M_{ijkl}^* \bar{\sigma}_{ij} \tag{4. 29}$$

For a multiple-phases composite with perfect contact, the average stress and strain follows:

$$\bar{\varepsilon}_{ij} = v_1 \bar{\varepsilon}^1_{ij} + v_2 \bar{\varepsilon}^2_{ij} \tag{4. 30}$$

$$\bar{\sigma}_{ij} = v_1 \bar{\sigma}^1_{ij} + v_2 \bar{\sigma}^2_{ij} \tag{4. 31}$$

where $\bar{\varepsilon}_{ij}$, $\bar{\varepsilon}^1_{ij}$, and $\bar{\varepsilon}^2_{ij}$ denote the average strains of the overall material, the matrix, and the inhomogeneity, respectively; v_1 and v_2 denote the volume fractions of the matrix and the inhomogeneity, respectively; and $\bar{\sigma}_{ij}, \bar{\sigma}^1_{ij}$, and $\bar{\sigma}^2_{ij}$ denote the average stresses of the overall material, the matrix, and the inhomogeneity, respectively. In Eq. (4.30), $\bar{\varepsilon}^a_{ij}$ satisfy Eq. (4.24) with the integral on phase a (where $a = 1, 2$ for the matrix and inhomogeneous, respectively).

4.1.6 Mori-Tanaka's Model

The well-known Mori-Tanaka's model [112, 113] is an effective field approximation based on Eshelby's model. It can be classified as a mean field micromechanics model that is used to obtain the effective stiffness of the composites in dilute or non-dilute condition. A fourth-order strain concentration tensor is used to relate the average overall macroscopic strain (or applied strain) to the average strain in inhomogeneity [112].

The method starts with considering an average uniform macroscopic strain of the overall material, since for two phases system, the average strain is expressed as shown in Eq. (4.30).

For composites, it follows that:

$$L^{*}_{ijkl}\bar{\varepsilon} = L^{1}_{ijkl}\bar{\varepsilon} + v_2(L^{2}_{ijkl} - L^{1}_{ijkl})\bar{\varepsilon}^{2} \tag{4. 32}$$

$$M^{*}_{ijkl}\bar{\sigma} = M^{1}_{ijkl}\bar{\sigma} + v_2(M^{2}_{ijkl} - M^{1}_{ijkl})\bar{\sigma}^{2} \tag{4. 33}$$

Eq. (4.32) and Eq. (4.33) can be in a simplified form by introducing T and B that:

$$L^{*}_{ijkl} = L^{1}_{ijkl} + v_2(L^{2}_{ijkl} - L^{1}_{ijkl})T \tag{4. 34}$$

$$\bar{\varepsilon}^{2} = T\bar{\varepsilon} \tag{4. 35}$$

and

$$M^{*}_{ijkl} = M^{1}_{ijkl} + v_2(M^{2}_{ijkl} - M^{1}_{ijkl})B \tag{4. 36}$$

$$\bar{\sigma}^{2} = B\bar{\sigma} \tag{4. 37}$$

where T and B are the strain concentration tensor and stress concentration tensor, which can be obtained using eigenstrain inside of inclusion and the Eshelby's tensor.

The Mori-Tanka model was initially derived for dilute problem, and was further generalized to non-dilute problem in which the interaction between inclusions or inhomogeneity cannot be ignored. In solving this problem, Mori-Tanaka model assumes the average strain $\bar{\varepsilon}^{2}$ in the non-dilute composite can be approximated as one inhomogeneity in an infinite matrix undergoing the average matrix strain $\bar{\varepsilon}^{1}$. In this way, the strain concentration tensor was modified as [51, 144]:

$$A = (v_1 I + v_2 T)^{-1} T \tag{4. 38}$$

and the effective stiffness can be expressed as:

$$L^*_{ijkl} = L^1_{ijkl} + v_2 \left(L^2_{ijkl} - L^1_{ijkl} \right) (v_1 I + v_2 T)^{-1} T \tag{4. 39}$$

Similarly, the effective compliance matrix can be expressed by:

$$M^*_{ijkl} = M^1_{ijkl} + v_2 \left(M^2_{ijkl} - M^1_{ijkl} \right) (v_1 I + v_2 B)^{-1} B \tag{4. 40}$$

The Mori-Tanka scheme was originally derived for inhomogeneity – matrix type composites with dilute or uniform non-dilute condition, however, in this work, the functionally graded porous material is considered, which means that the porosity is changing over the volume in a linear or polynomial varying fashion. In addition, for graded porous material, either the pore size is gradually changing, or the number of pores is varying, or both could occur. As such, adoption of Mori-Tanaka scheme directly by applying the volume average porosity to obtain the effective stiffness of FGPMs would cause inaccurate results.

In addition, Mori-Tanaka method was initially derived for a linear elastic solid body with distributed inhomogeneity, which indicates that no interconnected inhomogeneity are involved. While in this work, both open cell and closed cell structures are considered. In open cell materials, the interconnected pores would affect the stress and strain field of each other. This interaction between the adjacent pores, however, is not considered in the original Mori-Tanaka method. Therefore, inaccurate predictions

could occur when adopting the method to model the effective stiffness of open cell structures.

In this work, the derivation of analytical model for FGPMs uses RVE approach (as described in Section 4.1.2). The volume average stress and strain of RVEs (as described in Section 4.1.4) and the stress-strain relationship for elastic materials (as described in Section 4.1.3) are considered in order to obtain the effective elastic moduli (as described in Section 4.1.5) of FGPMs. Mori-Tanaka's model (as described in Section 4.1.6) is extended to the cases of graded and porous material and open cell structure. The method is based on Eshelby's tensor (as described in Section 4.1.1).

4.1.7 Preliminary Study on the Prediction Accuracy of Mori-Tanaka Model on FGPMs

A preliminary study on the discrepancy between the Mori-Tanaka scheme and finite element models in predicting the effective stiffness of FGPMs were carried out. In this study, specimens with three different overall average porosities were examined. For each configuration, eight different layers with different porosities were built up to form an open cell structure, and the pores are cuboid with their size varied for different layers. The base material property was set as 2400 MPa for elastic modulus and 0.34 for Poisson's ratio. Table 4.2 shows the average porosity of each configuration and the

specimen is depicted in Figure 4.4. For each specimen, Direction 3 is the layer stacking direction, and Direction 1&2 are the in plane directions.

Table 4. 2 Average porosity of each configuration

	Average porosity
Specimen Configuration 1	0.25
Specimen Configuration 2	0.49
Specimen Configuration 3	0.72

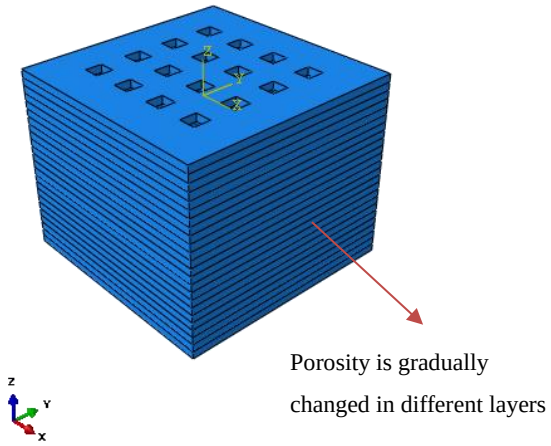

Figure 4. 4 The specimen for studying the discrepancy between the Mori-Tanaka scheme and Finite element model

The comparison between the results from Mori-Tanaka scheme and those from finite element models in predicting the effective stiffness of FGPMs for specimens

described above is demonstrated in Figure 4.5.

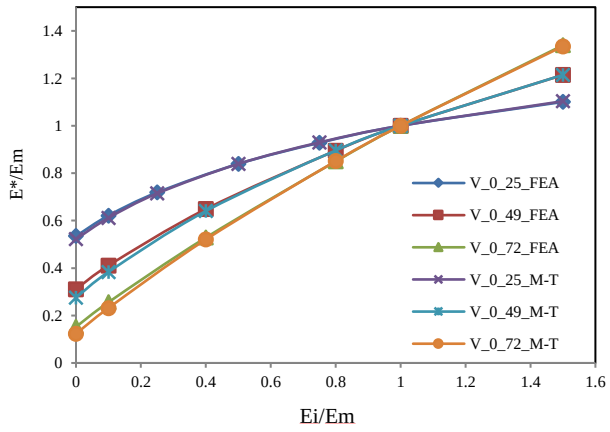

(a) Discrepancy between the Mori-Tanaka scheme and FEA models for E_{33}

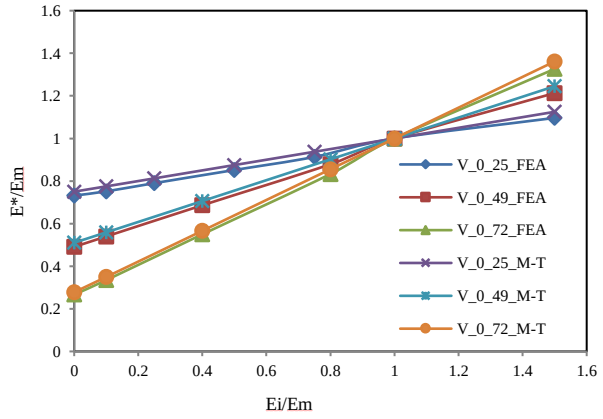

(b) Discrepancy between the Mori-Tanaka scheme and FEA models for E_{11} & E_{22}

Figure 4. 5 The discrepancy between Mori-Tanaka and FEA models for different specimen configurations

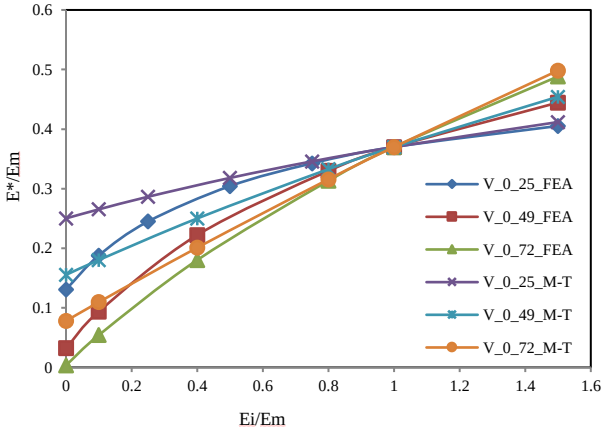

(c) Discrepancy between the Mori-Tanaka scheme and FEA models for G_{12}

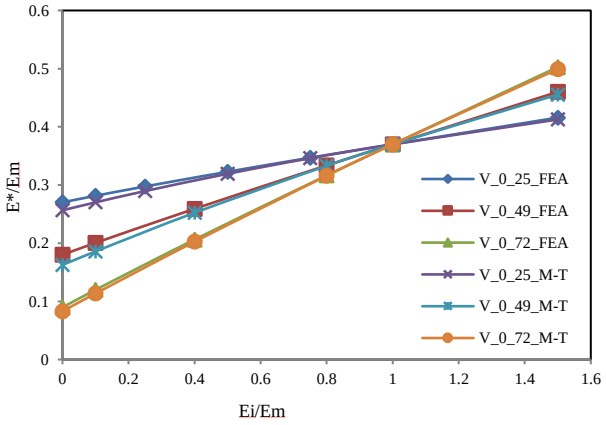

(d) Discrepancy between the Mori-Tanaka scheme and FEA models for G_{23}&G_{31}

Figure 4.5 Continued

In Figure 4.5, the *x*-axis E_i/E_m refers to the elastic modulus ratio of the inhomogeneity and the matrix where x=0 indicates the inhomogeneity becomes a void.

The *y*-axis E^*/E_m denotes the normalized effective modulus of the overall material predicted either by Mori-Tanaka scheme or FEA model. It is observed that there is some discrepancy between the two predictions, and the discrepancy increases with the higher volume fraction of inhomogeneity. This is due to the fact that there is a graded field of stress and strain due to graded porosity over the volume, while Mori-Tanaka's scheme used volume average porosity, and will result in discrepancy. In addition, the interaction between the interconnected pores is not considered. The above results imply that a generalized Mori-Tanaka model for FGPMs is needed to better predict their overall stiffness. An extension to the open cell structure is also necessary when deal with interconnected pore structures.

4.2 A Generalization of Mori-Tanaka's Model to FGPMs

An extension of Mori-Tanaka's Model to FGPMs will be discussed in this section. Section 4.2.1 discusses the overall basic idea of the derivation. In Section 4.2.2, the perturbation of one cavity embedded in an infinite large matrix is discussed. Section 4.2.3 deals with the polynomial varying boundary condition by assuming the matrix is undergo a gradient strain field. In Section 4.2.4, the varying perturbed strain field under graded applied matrix strain is presented. The strain concentration tensor of FGPMs is

demonstrated in Section 4.2.5. Finally, the overall effective stiffness matrix of FGPMs is presented in Section 4.2.6.

4.2.1 Basic Ideas

To model FGPMs based on Mori-Tanaka's method, the derivation starts with considering a single void in an infinite matrix. Assuming the matrix is incompressible, the model derivation addresses the perturbed field caused by the void as well as the compressibility of void. The problem is then generalized to "graded and porous" case. This more generalized case with polynomial varying porosity of voids embedded in a linear elastic solid body is investigated and the corresponding polynomial varying stress and strain fields of the material are derived. The developed relation is then applied to Mori-Tanaka's scheme to obtain the overall effective stiffness for FGPMs.

4.2.2 The Perturbation of One Cavity in Matrix

Consider a single void embedded in a linear elastic body as shown in Figure 4.6, and the whole material undergoes a remote externally applied stress σ_{kl}^{0}. The total strain of the body is the superposition of responses due to two effects: the first is the strain

caused by the external stress σ_{kl}^{0} without considering the perturbation of void,

$$\varepsilon_{ij}^{1} = M_{ijkl}^{1}\sigma_{kl}^{0} \tag{4. 41}$$

where σ_{kl}^{0} and ε_{ij}^{1} denote the external applied stress and the corresponding strain under the external load without considering the perturbation effect of void, respectively; and M_{ijkl}^{1} denotes the compliance tensor of the matrix.

The second response considers the perturbation effect due to the involvement of the void ε_{ij}^{2}, whereas the perturbed strain is a linear function of applied stress:

$$\varepsilon_{ij}^{2} = H_{ijkl}\sigma_{kl}^{0} \tag{4. 42}$$

where ε_{ij}^{2} denotes the perturbation strain due to void, and H_{ijkl} is a fourth rank tensor which is called a cavity compliance tensor [127]. Eq. (4.42) shows that the response of perturbation strain to external applied stress is linear. And for 3-D case, the expression of this cavity compliance tensor depends on the applied strain and the geometry of the cavity.

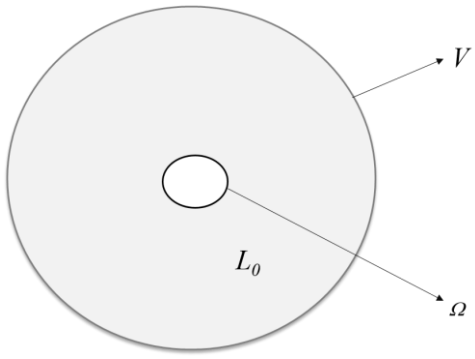

Figure 4. 6 A single void embedded in a linear elastic medium

Therefore, the total strain in the matrix subjected to a remotely applied stress can be expressed as [127]:

$$\varepsilon_{ij} = \varepsilon_{ij}^{1} + \varepsilon_{ij}^{2} \tag{4. 43}$$

where ε_{ij} denotes the overall effective strain subjected to external stress. Eq. (4.42) can be further specified using Eq. (4.24) [143]:

$$\varepsilon_{ij}^{2} = -\frac{1}{2V}\int_{\Omega}(u_i n_j + u_j n_i)d\Omega \tag{4. 44}$$

where V denotes the total volume of overall material including the cavity; u_i is the displacement of the cavity boundary Ω; n_i is the normal direction point inward of the cavity.

Substitute Eq. (4.22) into Eq. (4.21), it gives:

$$M_{ijkl}^{*}\sigma_{kl}^{0} = M_{ijkl}^{1}\sigma_{kl}^{0} - \frac{1}{2V}\int_{\Omega}(u_i n_j + u_j n_i)d\Omega \tag{4. 45}$$

where M_{ijkl}^{*} denotes the overall effective compliance matrix of overall material.

4.2.3 Polynomial Varying Boundary Conditions

The mechanical behavior of FGPMs can be investigated using an extension of Mori-Tanka's method. Since the porosity is graded in the built-up direction, the strain field due to the perturbation of voids is also graded. Similar to the generalization from the dilute case to the non-dilute case in Mori-Tanaka model [122], the interaction

between voids can be treated as follows: the problem of one void embedded in a finite matrix which contains a lot of graded voids can be approximated as the problem in which a single void embedded in an infinite homogeneous matrix, while the matrix undergoes a graded strain field which is exactly the same as the original porosity graded field. Furthermore, it is also assumed that the graded strain field of the matrix is caused by external graded boundary condition applied on the matrix. Therefore, it is necessary to study the stress-strain relationship under the graded varying applied boundary condition.

For a polynomial varying boundary condition applied to a homogeneous body in i direction, the strain field follows:

$$\varepsilon_i(x) = \varepsilon_0(1 + a_1 x_i + a_2 {x_i}^2 + a_3 {x_i}^3 + \cdots) = \varepsilon_0(1 + \sum_{n=1}^{N} a_n {x_i}^n) \qquad (4.46)$$

where $\varepsilon_i(x)$ denotes the strain field of the material and is a polynomial function of coordinate x, ε_0 denotes the volume average strain, and a_n is a series of constants which define the polynomial gradient of strain field.

Thus, by integral Eq. (4.46), the displacement field follows:

$$u_i(x) = \varepsilon_0(x_i + \frac{1}{2} a_1 {x_i}^2 + \frac{1}{3} a_2 {x_i}^3 + \frac{1}{4} a_3 {x_i}^4 + \cdots) = \varepsilon_0[x_i + \sum_{n=1}^{N} (\frac{1}{n+1} a_n {x_i}^{n+1})] \qquad (4.47)$$

where $u_i(x)$ denotes the displacement field of the material and is a polynomial function of coordinate x.

Therefore, the polynomial varying stress field is:

$$\sigma_{ij}(x) = L_{ijkl}\varepsilon_{kl} + L_{inkl}\varepsilon_{kl}(a_{kln1}x_n + a_{kln2}x_n{}^2 + a_{kln3}x_n{}^3 + ...)$$

$$= L_{ijkl}\varepsilon_{kl} + L_{inkl}\varepsilon_{kl}\sum_{n=1}^{N} a_n x^n \qquad (4.48)$$

The equilibrium equation follows:

$$\sigma_{ij,j} + b_i = 0 \qquad (4.49)$$

where b_i is the body force in the x_i direction, and σ_{ij} is defined in Eq. (4.48).

4.2.4 Varying Perturbed Strain Field

Now instead of the problem described in Section 4.2.2 which discusses the problem of a single void embedded in matrix, consider a series of voids embedded in a linear elastic solid body, and the porosity gradually changes over the layer built-up direction as in FGPMs. A polynomial function is used to describe the variation of porosity field with the coordinate in the gradient direction as shown in Eq. (4.50).

$$f(x) = b_0(1 + a_1x + a_2x^2 + a_3x^3 + \cdots) = b_0(1 + \sum_{n=1}^{N} a_n x^n) \qquad (4.50)$$

where the porosity distribution field $f(x)$ is a function of coordinate *x* in the pore gradient direction, a_n are a series of constants, and b_0 denotes the average porosity over the volume.

As discussed in the previous section, for the problem of FGPMs with graded voids embedded in a matrix and the porosity distribution field is a polynomial function $f(x)$ defined in Eq. (4.50), the perturbation strain field due to the graded voids has the same degree of polynomial as that in $f(x)$. Thus, in Eq. (4. 43) ε_{ij}^2 is also a polynomial function. Assuming the porosity gradient is in the i direction, the resulting perturbation strain field in the i direction is expressed as:

$$\varepsilon_i^{\,2}(x) = \varepsilon_0^2(1 + a_1 x + a_2 x^2 + a_3 x^3 + ...)$$

$$= \varepsilon_0^2(1 + \sum_{n=1}^{N} a_n x_j^{\,n}) \qquad (4.\ 51)$$

where $\varepsilon_0^{\,2}$ denotes the perturbed strain due to cavity at $x = 0$ in the gradient direction, x_i is the position in the i direction.

Similarly, the perturbed strain field is given by modifying Eq. (4.51):

$$\varepsilon_{ij}^2(x) = \varepsilon_0^{\,2}[1 + \sum_{j=1}^{3}(\sum_{n=1}^{N} a_n x_j^{\,n})] \qquad (4.\ 52)$$

where the summation of $j = 1, 2, 3$ takes into account the perturbed strain in the x_1, x_2, and x_3 directions.

It can be seen that the cavity compliance tensor H_{ijkl} in Eq. (4.42), which reflects how the perturbed strain due to cavity responses to the externally applied stress, is dependent on geometry and dimension of the void. The cavity compliance tensor is a constant under the condition of cavities with same geometry. For FGPMs, where the

cavities gradually varied over the volume, H_{ijkl} is not a constant over the volume. By introducing the polynomial graded perturbation field, for one direction graded material, Eq. (4.42) can be expressed as:

$$\varepsilon_i^2 = H_{ijkl}^0 \sigma_{ij}^0 + \sum_{n=1}^{n} (a_n x_j{}^n) H_{ijkl}^0 \sigma_{ij}^0 \tag{4. 53}$$

Similarly, the polynomial graded perturbation field can be expressed as:

$$\varepsilon_{ij}^2 = H_{ijkl}^0 \sigma_{ij}^0 + \sum_{i=1}^{3}\sum_{j=1}^{3}[\sum_{n=1}^{n} (a_n x_j{}^n H_{ijkl}^0) \sigma_{ij}^0] \tag{4. 54}$$

where the summation in $i = 1, 2, 3$ and $j = 1, 2, 3$ consider the perturbed strain field in the x_1, x_2, and x_3 directions.

Eq. (4.54) implies that, similar to porosity gradient field that consists of a constant term and polynomial gradient term, the perturbation field due the cavities is also composed of a constant term and a polynomial varying gradient term. In addition, it also shows that for graded porous material, the cavity compliance tensor is not a constant matrix, rather it is different for different layers, and the graded field follows the porosity graded field. In Eq. (4.54), the constant term and graded term can be separated, which yields:

$$\varepsilon_0^2 = H_{ijkl}^0 \sigma_{ij}^0$$

$$k_1 = \sum_{j=1}^{3}[\sum_{n=1}^{n} (a_n x_j{}^n H_{ijkl}^0) \sigma_{1j}]$$

$$k_2 = \sum_{j=1}^{3}[\sum_{n=1}^{n}(a_n x_j{}^n H_{ijkl}^0)\sigma_{2j}] \qquad (4.55)$$

$$k_3 = \sum_{j=1}^{3}[\sum_{n=1}^{n}(a_n x_j{}^n H_{ijkl}^0)\sigma_{3j}]$$

where H_{ijkl}^0 is a 6×6 matrix, ε_0^2, k_1, k_2, and k_3 are all 6×1 vector, ε_0^2 denotes the constant term of the perturbed strain field, and k_1, k_2, and k_3 denote the varying gradient term of the perturbed strain field in the 1, 2, and 3 direction, respectively. In this way, the total perturbation strain field can be written in the form of:

$$\varepsilon_{ij}^2 = \begin{Bmatrix} \varepsilon_0^2 \\ k_1 \\ k_2 \\ k_3 \end{Bmatrix} \qquad (4.56)$$

where ε_{ij}^2 in Eq. (4.56) is a 24×24 matrix.

4.2.5 Strain Concentration Tensor

As discussed in Section 4.2.3, a void embedded in a finite matrix filled with porosity-graded voids where interaction between voids cannot be ignored could be approximated as the void embedded in an infinite large homogeneous matrix undergo an externally applied graded boundary condition. Therefore, it is necessary to determine the matrix strain field under that graded boundary condition.

Now consider a single void embedded in an infinite homogeneous matrix, and

the matrix is subjected to a remotely applied polynomial varying boundary field as given by:

$$\varepsilon_{ij}^{1}(x) = \varepsilon_{0}^{1} + \sum_{j=1}^{3}(\sum_{n=1}^{n} a_n x_j^{\,n})\varepsilon_{0}^{1} \tag{4. 57}$$

where $\varepsilon_{ij}^{1}(x)$ is 6×1 matrix denoting the matrix varying strain field that consists of a constant and a varying strain vector. The summation of $j = 1, 2, 3$ takes into account the varying strains in the x_1, x_2, and x_3 directions.

From the above discussion, it is demonstrated that without the involvement of cavities, the strain field in the matrix is defined as in Eq. (4.57). However, there are voids present, and the perturbed the strain field is defined by Eq. (4.52). Thus, the strain field on the boundary of cavity is a superposition of the polynomial varying applied strain field and the polynomial varying perturbed strain field given by:

$$\varepsilon_{ij}(x) = \varepsilon_{ij}^{2}(x) + \varepsilon_{ij}^{1}(x) \tag{4. 58}$$

By substitute Eq. (4.52) and Eq. (4.57) into Eq. (4.58), it yields:

$$\varepsilon_{ij}(x) = \varepsilon_{0}^{1}[1 + \sum_{j=1}^{3}(\sum_{n=1}^{n} a_n x_j^{\,n})] + \varepsilon_{0}^{2}[1 + \sum_{j=1}^{3}(\sum_{n=1}^{n} a_n x_j^{\,n})] \tag{4. 59}$$

Eq. (4.59) can be also written as below:

$$\varepsilon_{ij}(x) = M\varepsilon_{0}^{1} + N\varepsilon_{0}^{2} \tag{4. 60}$$

where
$$M = I + \sum_{j=1}^{3}(\sum_{n=1}^{n} a_n x_j^{\,n})I\,, \tag{4. 61}$$

$$N = I + \sum_{j=1}^{3}(\sum_{n=1}^{n} a_n x_j{}^n)I \tag{4. 62}$$

and *I* is the unit vector. Eq. (4.60) shows that for FGPMs, the strain field at boundary of the cavity over the volume is also graded, and the degree of polynomial follows the same degree of polynomial in porosity distribution function.

Since the stress-strain relation follows $\varepsilon_{ij}^1 = M_{ijkl}^1 \sigma_{kl}^0$ for the matrix and $\varepsilon_{ij}^2 = H_{ijkl}\sigma_{kl}^0$ for the cavities as shown in Eqs. (4.39) and (4.40), combining the two equations gives:

$$\varepsilon_{ij}^2 = H_{ijkl}\varepsilon_{ij}^1 L_{ijkl} \tag{4. 63}$$

In Eq. (4.63), let

$$\varepsilon_{ij}^2 = \beta\varepsilon_{ij}^1 \tag{4. 64}$$

where
$$\beta = H_{ijkl}L_{ijkl} \tag{4. 65}$$

Eqs. (4.64) and (4.65) show how the perturbation field due to presence of cavities varies with the matrix strain field due to the externally applied varying boundary condition. Note that in Eq. (4.65), β is not a constant over the volume. As discussed in the previous section, the cavity compliance tensor H_{ijkl} is graded, corresponding to graded porosity field. Therefore, β is also graded.

Substituting (4.64) into (4.61), the equation becomes:

$$\varepsilon_{ij}(x) = (M + N\beta)\varepsilon_0^1 \tag{4. 66}$$

where M , N and β are defined in Eqs. (4.61), (4.62), and (4.65).

Rearranging Eq. (4.66) results in:

$$\varepsilon_{ij}(x) = T\varepsilon_0^1 \tag{4. 67}$$

where

$$T = (M + N\beta) \tag{4. 68}$$

and T can be called the strain concentration tensor as it is extended and derived from Mori-Tanaka model for FGPMs. The strain concentration tensor relates the strain field at the cavity boundary to that of the matrix applied boundary condition.

From the above derivation, it can be observed that the strain concentration tensor is dependent on porosity varying field, the stiffness of matrix, and the cavity compliance tensor that relates to geometry and dimension of cavities.

4.2.6 The Overall Effective Stiffness Matrix of FGPMs

Now consider a RVE for FGPMs consists of m different layer ($m \geq 1$) and n different cavities ($n \geq 1$) where the interaction between cavities cannot be ignored. The previous section deals with the problem of one single cavity embedded in a finite matrix with graded varying cavities. For general FGPMs case, different cavities need to be considered. Assume the overall materials can be divided into $n+1$ sub-volumes, where the first sub-volume stands for base material, while the rest of the sub-volumes stand for the pores for each layer. The overall volume average strain can be expressed as [49]:

$$\bar{\varepsilon} = \frac{1}{V}\int_V \varepsilon(x)dV = \sum_{r=1}^{n+1}\frac{V_r}{V}\frac{1}{V_r}\int_{V_r}\varepsilon(x)dV = \sum_{r=1}^{n+1} v^r \bar{\varepsilon}_{ij}^r \tag{4. 69}$$

where $\bar{\varepsilon}$ denotes the volume average strain of FGPMs; V and V_r denote the volume of the overall material and r[th] sub-volume, respectively; n is the total number of sub volumes; v^r is volume fraction of r[th] sub-volume; $\bar{\varepsilon}_{ij}^r$ denotes the volume average strain of r[th] sub-volume; $\bar{\varepsilon}_{ij}^1$ is the strain of base material; and $\bar{\varepsilon}_{ij}^r$ is the strain at the cavity boundary of r[th] sub-volume. Thus, the average stress and strain of FGPMs follows that:

$$\bar{\varepsilon} = \sum_{r=1}^{n+1} v_r \bar{\varepsilon}_{ij}^r \tag{4. 70}$$

and similarly,

$$\bar{\sigma} = \sum_{r=1}^{n+1} v_r \bar{\sigma}_{ij}^r \tag{4. 71}$$

where $\bar{\sigma}$ and $\bar{\sigma}_{ij}^r$ denote the volume average stress of overall FGPMs and r[th] sub-volume, respectively.

Consider a variety of porosity – polynomial varied cavities embedded in the matrix, the overall material is subjected to a remotely applied strain $\bar{\varepsilon}$, and the strain fields of the material are polynomial functions. Substitute Eq. (4.67) into Eq. (4.70):

$$\bar{\varepsilon} = (v_1 + \sum_{r=2}^{n+1} v^r T_r)\varepsilon_0^1 \tag{4. 72}$$

Note that the1[st] sub-volume refers to the base material phase, e.g. v_1 in Eq. (4.72) denotes the volume fraction of base material. T_r is the partial strain concentration tensor for the r[th] sub-volume.

Rewriting Eq. (4.72), it gives:

$$\varepsilon_0^1 = (v_1 + \sum_{r=2}^{n+1} v^r T_r)^{-1} \bar{\varepsilon} = A\bar{\varepsilon} \tag{4. 73}$$

where

$$A = (v_1 + \sum_{r=2}^{n+1} v^r T_r)^{-1} \tag{4. 74}$$

Eq. (4.73) shows how the matrix applied strain related to the volume average applied strain. Note the matrix applied strain is used to study the interaction between the cavities, and volume average applied strain is the real strain that applied to FGPMs.

Substituting Eq. (4.73) to Eq. (4.64) yields

$$\varepsilon_{ij}^2 = AT_r \bar{\varepsilon} \tag{4. 75}$$

In Eq. (4.75), AT_r can be considered as the strain concentration tensor of the material as defined in Mori-Tanaka's model and it relates the strain at the cavity boundary to the volume average applied strain.

Substitute Eq. (4.75) to Mori-Tanaka's model in Eq. (4.34) and Eq. (4.70), it can be obtained that:

$$L_{ijkl}^* \bar{\varepsilon} = \sum_{r=1}^{n+1} v_r L_{ijkl}^1 \bar{\varepsilon}_{ij}^r \tag{4. 76}$$

where L_{ijkl}^* and L_{ijkl}^1 denote the stiffness of the overall material and that of the matrix, respectively; L_{ijkl}^* is 24×24 matrix that contains constant term and graded term, $\bar{\varepsilon}$ and $\bar{\varepsilon}_{ij}^r$ denote the volume average applied strain and volume average strain of rth sub-volume, $\bar{\varepsilon}$ and $\bar{\varepsilon}_{ij}^r$ is 24×1 matrix that contains constant term and graded term which similar to

Eq. (4.57). Substitute Eq. (4.75) into Eq. (4.76):

$$L^{*}_{ijkl}\,\bar{\varepsilon} = \sum_{r=1}^{n+1} v_r L^{1}_{ijkl}\,(AT_r\,\bar{\varepsilon}) \tag{4. 77}$$

$$L^{*}_{ijkl} = \sum_{r=1}^{n+1} v_r L^{1}_{ijkl} AT_r \tag{4. 78}$$

Rewriting Eq. (4.78), it can be shown that:

$$L^{*}_{ijkl} = L^{1}_{ijkl}[I + \sum_{r=2}^{n+1} v_r \beta]A \tag{4. 79}$$

where β is defined in Eq. (4.65). From Eqs. (4.78) and (4.79), it is observed that the overall stiffness of the material depends on strain concentration tensor, the geometry of each sub-volume, and the stiffness of the base material.

4.3 An Extension of Mori-Tanaka's Scheme to Open Cell Structure

In the previous section, the analytical model for FGPMs is derived by generalizing Mori-Tanaka's scheme with the consideration of the effects of graded porosity field. Since Mori-Tanaka's model was initially developed for composites, i.e. fiber reinforced materials, when used for porous material, it is more appropriate for closed cell porous materials. However, for the case of open cell structures or interconnected pores, the interaction between two connected pores needs to be taken into

account because of the disturbed stress field will affect each other. Thus, an extension of Mori-Tanaka's model to interconnected pores or open cell structure is needed.

In Section 4.3.1, the approach of extending Mori-Tanaka's method to open cell structure is described where the disturbed stress field between interconnect pores is considered. In Section 4.3.2, the extension of Mori-Tanaka's model to open cell structure is implemented. Sections 4.3.3 and 4.3.4 provide the analytical solution for disturbed stress field of cavity, where Section 4.3.3 discusses the disturbed stress field of cavity just outside the inclusion, Section 4.3.4 shows the disturbed stress field of cavities with different shapes, i.e. ellipsoid and cuboid cavities, for isotropic and anisotropic materials.

4.3.1 The Approach to Extend Mori-Tanaka's Model to Open Cell Structure

Assume that two interconnected cavities, Cavity 1 and Cavity 2, are embedded in a matrix as shown in Figure 4.7. In the absence of Cavity 2, the presence of Cavity 1 will generate perturbed stress and strain field to the matrix as discussed in the previous section. However, the existence of Cavity 2, which also cause perturbation to the elastic field, will disturb the perturbation stress field of Cavity 1.

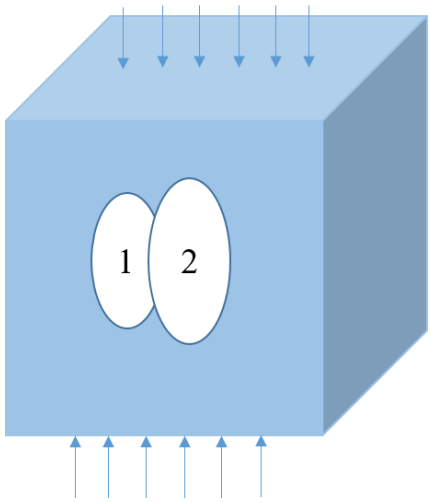

Figure 4. 7 Two interconnected pores embedded in a matrix

In order to solve the problem, the following approach proposed by Zhao and Taya [145] is adopted here: the perturbation stress and strain fields as well as eigenstrains caused by Cavity 1 and Cavity 2 will be considered separately first, and later the two interconnected pores will be put together and reach an overall stress strain field and an overall eigenstrain. In the first step, the perturbation stress $\sigma_{ij}^{2(1)}$ and strain $\varepsilon_{ij}^{2(1)}$ and eigenstrain $\varepsilon_{ij}^{*(1)}$ due to the presence of the Cavity 1 in the matrix undergo externally applied stress σ_{ij}^{0} is considered. The disturbance of Cavity 2 will not be considered here, but Mori-Tanaka's mean field approach will be considered for obtaining the interaction between Cavity 1 and Cavity 2. The next step involves obtaining the eigenstrain $\varepsilon_{ij}^{*(2)}$ due to both the presence of Cavity 2 which can be obtained

by Mori-Tanaka's mean field approach, and the disturbed [146] stress field $\sigma_{ij}^{d1}(x)$ caused by the perturbed stress of Cavity 1. The third step is to obtain the weighted average eigenstrain ε_{ij}^{**} from of $\varepsilon_{ij}^{*(1)}$ and $\varepsilon_{ij}^{*(2)}$ as the eigenstrain for the two interconnected cavities. In this step, the two interconnected cavities is treated as "one cavity", and the weighting is based on the dimension of the pores.

In [145], the disturbed stress caused by cavities is simplified by only considering the difference between stress just outside and inside of the inclusion. However, in this work, the stress fields of cavities with different shapes embedded in isotropic and anisotropic materials are considered.

4.3.2 Implementation of Extension of Mori-Tanaka Model to Open Cell Structure

As discussed above, the first step is to determine the eigenstrain $\varepsilon_{ij}^{*(1)}$ for Cavity 1, and the disturbance from Cavity 2 is not considered. Thus, the eigenstrain can be expressed as:

$$\varepsilon_{ij}^{*(1)} = \frac{1}{v_1}(S_{ijkl} - I_{ijkl})^{-1} M_{ijkl}^{1} \sigma_{ij}^{0} \tag{4. 80}$$

where $\varepsilon_{ij}^{*(1)}$ denotes the eigenstrain due to Cavity 1, v_1 denotes the volume fraction of the matrix, S_{ijkl} denotes the Eshelby's tensor, I_{ijkl} denotes the unit vector, M_{ijkl}^{1} denotes the compliance tensor of the matrix, and σ_{ij}^{0} denotes the externally applied stress.

The second step involves obtaining the eigenstrain $\varepsilon_{ij}^{*(2)}$ by taken into account of the perturbation due to Cavity 2 and the disturbed stress caused by Cavity 1. The latter is the perturbation stress field outside of Cavity 1. The total stress in cavity can be expressed as [145]:

$$\sigma_{ij}^{t(2)} = \sigma_{ij}^{0} + \sigma_{ij}^{2(2)} + \sigma_{ij}^{d1} = 0 \tag{4. 81}$$

where $\sigma_{ij}^{t(2)}$ denotes the overall stress field at the boundary of Cavity 2; $\sigma_{ij}^{2(2)}$ denotes the perturbation of stress due to the presence of cavity; and σ_{ij}^{d1} denotes the disturbed stress field outside the cavity. In general, $\sigma_{ij}^{d1}(x)$ is a disturbed stress field that changed with the coordinate. The solution of $\sigma_{ij}^{d1}(x)$ depends on the property of base material, the geometry and dimension of cavity, which will be discussed in Sections 4.3.3 to 4.3.4.

The expression of $\sigma_{ij}^{2(2)}$ in Eq. (4.81) can be expressed as:

$$\sigma_{ij}^{2(2)} = v_1 L_{ijkl}^{1}(S_{ijkl} - I_{ijkl})\varepsilon_{ij}^{*(2)} \tag{4. 82}$$

where L_{ijkl}^{1} denotes the stiffness tensor of the matrix.

Once the externally applied stress σ_{ij}^{0} is given, and $\sigma_{ij}^{2(2)}$ and $\sigma_{ij}^{d1}(x)$ are solved, $\sigma_{ij}^{t(2)}$ at a particular location can be found. Therefore, $\varepsilon_{ij}^{*(2)}$ can be obtained.

In the last step, a weighted average eigenstrain ε_{ij}^{**} for open cell is obtained by:

$$\varepsilon_{ij}^{**} = c_1\varepsilon_{ij}^{*(1)} + c_2\varepsilon_{ij}^{*(2)} \tag{4. 83}$$

where is c_1 and c_2 are constants used to calculate the weighted average eigenstrain, which are directly related to the dimension of the two interconnected open cells, and

$$c_1 + c_2 = 1 \tag{4. 84}$$

Once ε_{ij}^{**} is obtained for each pair of interconnected open cells, it can be used in Mori-Tanaka's method as discussed above to predict the effective modulus of the overall material.

4.3.3 Disturbed Stress Field of Cavity Just Outside the Inclusion

As discussed in the above section, in order to apply Mori-Tanaka's scheme on open cell structure, it is required to obtain the stress field of a cavity thus the disturbed stress σ_{ij}^{d1} in Eq. (4.81) can be derived. The process of deriving the expression of the stress fields of an elliptical cavity and a cuboid cavity embedded in both isotropic and anisotropic materials will be demonstrated. In a special case, the explicit solution of stress difference just outside and inside of the cavity is given as well.

General solution for stress field outside of cavity

The general solution for elastic field, i.e. displacement field, strain field, and stress field, due to an inclusion are given as below. Eqs. (4.85) to (4.91) follows the derivation of [146].

$$u_i(\hat{x}) = -i(2\pi)^{-3}\int_{-\infty}^{\infty}\int_{\Omega} C_{jlmn}\varepsilon^*_{mn}(\hat{x}')\xi_l N_{ij}(\hat{\xi})\times D^{-1}(\hat{\xi})$$

$$\times\exp\{i\hat{\xi}\cdot(\hat{x}-\hat{x}')\}d(\hat{\xi})d(\hat{x}') \qquad (4.85)$$

where in this work, a variable with a hat denotes a vector, i.e. $\hat{x}$ and $\hat{\xi}$ refer to $(x_1, x_2, x_3)^T$ and $(\xi_1, \xi_2, \xi_3)^T$. $\hat{x}$ denotes the coordinate of a particular point which is to be investigated, $\hat{x}'$ denotes the coordinate in the inclusion space, u_i denotes the displacement in the i direction, $\varepsilon^*_{mn}(\hat{x}')$ denotes the eigenstrain of inclusion, since the eigenstrain ε^*_{mn} is originally given as a wave vector $\varepsilon^*_{ij}(\hat{x}) = \bar{\varepsilon}^*_{ij}(\hat{\xi})\exp(i\hat{\xi}\cdot\hat{x})$, $\hat{\xi}$ denotes the wave vector within the given period of wave, C_{jlmn} denotes the stiffness of base material, Ω denotes the domain of inclusion, $N_{ij}(\hat{\xi})$ and $D(\hat{\xi})$ are the cofactor and determinant of :

$$K_{11}\bar{u}_1 + K_{12}\bar{u}_2 + K_{13}\bar{u}_3 = X_1$$

$$K_{21}\bar{u}_1 + K_{22}\bar{u}_2 + K_{23}\bar{u}_3 = X_2 \qquad (4.86)$$

$$K_{31}\bar{u}_1 + K_{32}\bar{u}_2 + K_{33}\bar{u}_3 = X_3$$

where $\quad K_{ik}(\bar{\xi}) = C_{ijkl}\xi_j\xi_l, \quad X_i = -iC_{ijkl}\bar{\varepsilon}^*_{kl}\xi_j \qquad (4.87)$

and the solution of displacement u_i in Eq. (4.86) is given by $\bar{u}_i(\hat{\xi}) = X_j N_{ij}(\hat{\xi}) / D(\hat{\xi})$.

(4. 88)

Note that

$$\int_{-\infty}^{\infty} d(\hat{\xi}) = \int_{-\infty}^{\infty} d\xi_1 \int_{-\infty}^{\infty} d\xi_2 \int_{-\infty}^{\infty} d\xi_3 \ , \ \int_{-\infty}^{\infty} d(\hat{x}) = \int_{-\infty}^{\infty} dx_1 \int_{-\infty}^{\infty} dx_2 \int_{-\infty}^{\infty} dx_3 \qquad (4.89)$$

The strain field of $\varepsilon_{ij}(\hat{x})$ is given by the derivative of the displacement field $u_i(\hat{x})$ in Eq. (4.85):

$$\varepsilon_{ij}(\hat{x}) = (2\pi)^{-3}\int_{-\infty}^{\infty}\int_{\Omega}(1/2)C_{klmn}\varepsilon_{mn}^{*}(\hat{x}')\xi_l\{\xi_j N_{ik}(\hat{\xi}) + \xi_i N_{jk}(\hat{\xi})\}$$

$$\times D^{-1}(\hat{\xi})\exp\{i\hat{\xi}\cdot(\hat{x}-\hat{x}')\}d(\hat{\xi})d(\hat{x}') \tag{4. 90}$$

The stress field can be obtained using Eshelby's inclusion problem as given by:

$$\sigma_{ij}(\hat{x}) = C_{ijkl}\{(2\pi)^{-3}\int_{-\infty}^{\infty}\int_{\Omega}C_{pqmn}\varepsilon_{mn}^{*}(\hat{x}')\xi_q\xi_l N_{kp}(\hat{\xi})D^{-1}(\hat{\xi})$$

$$\times\exp\{i\hat{\xi}\cdot(\hat{x}-\hat{x}')\}d(\hat{\xi})d(\hat{x}') - \varepsilon_{kl}^{*}(\hat{x})\} \tag{4. 91}$$

where $\varepsilon_{kl}^{*}(\hat{x})$ is the eigenstrain.

Define Green's function $G_{ij}(x-x')$ as:

$$G_{ij}(x-x') = (2\pi)^{-3}\int_{-\infty}^{\infty}N_{ij}(\hat{\xi})\times D^{-1}(\hat{\xi})\exp\{i\hat{\xi}\cdot(\hat{x}-\hat{x}')\}d(\hat{\xi}) \tag{4. 92}$$

where generally the elastic Green's function $G_{ij}(x,x')$ can be used to solve the problem when a point force is at x' and the displacement at x is known [142].

Therefore, substitute Eq. (4.92) into Eqs. (4.85), (4.90)-(4.91), the elastic field can be expressed as:

$$u_i(\hat{x}) = -\int_{\Omega}C_{jlmn}\varepsilon_{mn}^{*}(\hat{x}')G_{ij,l}(\hat{x}-\hat{x}')d(\hat{x}') \tag{4. 93}$$

$$\varepsilon_{ij}(\hat{x}) = -(1/2)\int_{\Omega}C_{klmn}\varepsilon_{mn}^{*}(\hat{x}')\{G_{ik,lj}(\hat{x}-\hat{x}') + G_{jk,li}(\hat{x}-\hat{x}')\}d(\hat{x}') \tag{4. 94}$$

$$\sigma_{ij}(\hat{x}) = -C_{ijkl}\{\int_{\Omega}C_{pqmn}\varepsilon_{mn}^{*}(\hat{x}')G_{kp,ql}(\hat{x}-\hat{x}')d(\hat{x}') + \varepsilon_{kl}^{*}(\hat{x})\} \tag{4. 95}$$

It is known that the displacement and traction field should be continuous throughout the material and across the interface of the inhomogeneity and the matrix. Therefore, the displacement and traction field at the interface can be expressed as:

$$[u_i] = u_i(out) - u_i(in) = 0 \tag{4. 96}$$

$$[\sigma_{ij}]n_j = \{\sigma_{ij}(out) - \sigma_{ij}(in)\}n_j = 0 \tag{4. 97}$$

where $u_i(out)$ and $u_i(in)$ denote the displacement of material just outside and just inside the inclusion, respectively; $\sigma_{ij}(out)$ and $\sigma_{ij}(in)$ denote the stress of material just outside and just inside the inclusion, respectively; n_j denotes the normal direction point outside of the inclusion.

However, the strain field, unlike the displacement and stress field, can be discontinuous across the inclusion-matrix boundary. Thus,

$$[u_{i,j}] = u_{i,j}(out) - u_{i,j}(in) \neq 0 \tag{4. 98}$$

And according to [146], the Eq. (4.98) can be explicitly solved as:

$$[u_{i,j}] = -C_{lkmn}\varepsilon^*_{mn}n_k n_j N_{il}(\hat{n}) / D(\hat{n}) \tag{4. 99}$$

where n_k and n_j are the unit normals point to the outside of the inclusion, and $N_{il}(\hat{n})$ and $D(\hat{n})$ are defined in Eq. (4.86) and (4.87). And for stress just outside and inside of the inclusion, it gives:

$$[\sigma_{ij}] = C_{ijkl}\{-C_{pqmn}\varepsilon^*_{mn}n_q n_l N_{kp}(\hat{n}) / D(\hat{n}) + \varepsilon^*_{kl}\} \tag{4. 100}$$

In [145], the stress field of porous material is simplified by only considering the difference between stress just outside and inside of the inclusion as shown in Eq. (4.100). However, in this work, the stress fields of cavities with different shapes embedded in isotropic and anisotropic materials are considered.

4.3.4 Disturbed Stress Field of Cavities with Different Shapes

The disturbed stress field of cavities with different shapes is shown in this section, and for generality, anisotropic material will be considered first, and the solution to isotropic material case can be obtained as a special case of anisotropic material.

Ellipsoidal cavity

From the elastic displacement field of an inclusion shown in Eq. (4.85), it can be observed that for anisotropic material, the Green's function is not only a function of coordinate, but also varied in different directions, i.e. for transversely isotropic material where direction 1 and 2 have the same property but different from direction 3, $G_{11} \neq G_{33}$. In Eq. (4.85), the integration with respect to $x_1^{'}$, $x_2^{'}$, and $x_3^{'}$ is within Ω domain.

After transformations, Eq. (4.85) is simplified as:

$$u_i(\hat{x}) = -\frac{a_1 a_2 a_3}{8\pi^2}\int_{-1}^{1} dz \int_0^{2\pi} d\phi \int_0^R r dr \int_{S^2} C_{klmn}\varepsilon_{nm}^{*}(\hat{x}^{'}) N_{ik}(\hat{\bar{\xi}}) \times D^{-1}(\hat{\bar{\xi}})\bar{\xi}_l \delta^{'}(\varsigma\hat{\varsigma}\cdot\hat{y} - \varsigma z) dS(\hat{\bar{\xi}}) \quad (4.101)$$

where $R = (1-z^2)^{1/2}$ has to be a real number in order to do integration [146].

From the displacement field shown in Eq. (4.85), the strain field $u_{i,j}(\hat{x})$ is given as:

$$u_{i,j}(\hat{x}) = -\frac{a_1 a_2 a_3}{8\pi^2}\int_{-1}^{1} dz \int_0^{2\pi} d\phi \int_0^R r dr \int_{S^2} C_{klmn}\varepsilon^*_{nm}(\hat{x}')N_{ik}(\hat{\bar{\xi}})$$
$$\times D^{-1}(\hat{\bar{\xi}})\bar{\xi}_l\bar{\xi}_j\delta''(\varsigma\hat{\varsigma}\cdot\hat{y}-\varsigma z)dS(\hat{\bar{\xi}}) \qquad (4.\ 102)$$

When investigating the elastic field inside the inclusion, $\hat{x}$ lies inside the inclusion, and $\hat{y}$ is inside the unit sphere, R is a real number. When investigating the elastic field outside the inclusion, $\hat{x}$ lies outside the inclusion, and $\hat{y}$ is outside the unit sphere, only for some $\hat{\varsigma}$ will result in a real number R. Therefore, for $\hat{x}$ lies outside the inclusion, the integral respect to S^2 might not be the whole surface of the unit sphere; rather, it is only a part of the surface of the unit sphere.

In order to obtain the stress field outside the inclusion as discussed in Section 4.3.2, the case that $\hat{x}$ lies outside the inclusion is considered here. Since:

$$dS(\hat{\varsigma}) = a_1 a_2 a_3 \varsigma^{-3} dS(\hat{\bar{\xi}}) \qquad (4.\ 103)$$

Substitute Eq. (4.103) into Eqs. (4.93) and (4.94), the displacement and strain field can be expressed as:

$$u_i(\hat{x}) = 8\pi^2\int_{-1}^{1} dz \int_0^{2\pi} d\phi \int_0^R r dr \int_{S^2} C_{klmn}\varepsilon^*_{nm}(\hat{x}')N_{ik}(\hat{\bar{\xi}})$$
$$\times D^{-1}(\hat{\bar{\xi}})\bar{\xi}_l\varsigma^2\frac{\partial}{\partial z}\delta'(\varsigma\hat{\varsigma}\cdot\hat{y}-\varsigma z)dS(\hat{\bar{\xi}}) \qquad (4.\ 104)$$

$$u_{i,j}(\hat{x}) = -(8\pi^2)^{-1}\int_0^{2\pi} d\phi[\int_0^R r dr \frac{\partial^2}{\partial z^2}\varepsilon^*_{nm}(\hat{x}') - (\hat{\varsigma}\cdot\hat{y})\{\frac{\partial}{\partial z}\varepsilon^*_{nm}(\hat{x}')\}_{r=R}$$
$$-(\hat{\varsigma}\cdot\hat{y})\frac{\partial}{\partial z}\{\varepsilon^*_{nm}(\hat{x}')\}_{r=R} - \varepsilon^*_{nm}(\hat{x}')]_{z=\hat{\varsigma}\cdot\hat{y}} \times C_{klmn}\int_{S^*} N_{ik}(\hat{\bar{\xi}})\times D^{-1}(\hat{\bar{\xi}})\bar{\xi}_l\bar{\xi}_j dS(\hat{\bar{\xi}})$$
$$-(2\pi)^{-1}\iint_{L^+}\{\varepsilon^*_{nm}(\hat{x}')\}_{z=\hat{\varsigma}\cdot\hat{y}=1} y^{-1}C_{klmn}N_{ik}(\hat{\bar{\xi}})D^{-1}(\hat{\bar{\xi}})\bar{\xi}_l\bar{\xi}_j d\theta(\hat{\varsigma})$$

(4. 105)

Further simplify Eq. (4.105) where $\varepsilon^*_{nm}(\hat{x}')$ is a constant, it gives:

$$u_{i,j}(\hat{x}) = -(8\pi^2)^{-1}[-2\pi\varepsilon^*_{nm}(\hat{x}')\times C_{klmn}]\int_0^{2\pi} d\theta(\hat{\bar{\xi}})\int_{-1/y}^{1/y} N_{ik}(\hat{\bar{\xi}})D^{-1}(\hat{\bar{\xi}})\bar{\xi}_l\bar{\xi}_j d\bar{\varsigma}_3'$$
$$-(2\pi)^{-1}[\varepsilon^*_{nm}(\hat{x}')C_{klmn}]\int_0^{2\pi} N_{ik}(\hat{\bar{\xi}})D^{-1}(\hat{\bar{\xi}})\bar{\xi}_l\bar{\xi}_j y^{-1} d\theta(\hat{\bar{\varsigma}}) \quad (4.106)$$

Since $d\bar{\varsigma}_3' = d\bar{\xi}_3'$, and let

$$g_{ijkl}(\hat{\bar{\xi}}) = N_{ik}(\hat{\bar{\xi}})D^{-1}(\hat{\bar{\xi}})\bar{\xi}_l\bar{\xi}_j \quad (4.107)$$

Combine Eq. (4.106) and Eq. (4.107), the strain field can be expressed that:

$$u_{i,j}(\hat{x}) = (4\pi)^{-1}\varepsilon^*_{nm}(\hat{x}')C_{klmn}\int_0^{2\pi} d\theta(\hat{\bar{\varsigma}})\int_{-1/y}^{1/y} g_{ijkl}(\hat{\bar{\xi}})d\bar{\xi}_3'$$
$$-(2\pi)^{-1}\varepsilon^*_{nm}(\hat{x}')C_{klmn}\int_0^{2\pi} g_{ijkl}(\hat{\bar{\xi}})y^{-1}d\theta(\hat{\bar{\varsigma}}) \quad (4.108)$$

For anisotropic material, $g_{ijkl}(\hat{\bar{\xi}})$ in Eq. (4.107) is different, i.e. the material property in direction 1 is different from that in direction 2, $g_{1111}(\hat{\bar{\xi}}) \neq g_{2222}(\hat{\bar{\xi}})$. As discussed in the previous sections, $N_{ik}(\hat{\xi})$ and $D(\hat{\xi})$ are the cofactor and the determinant of $K_{ij}(\xi)$ matrix, where $K_{ij}(\xi) = C_{ijkl}\xi_l\xi_j$. The expression for $N_{ik}(\hat{\xi})$ and $D(\hat{\xi})$ are provided in [146].

From Eq. (4.108), the stress field is obtained as:

$$\sigma_{ij}(\hat{x}) = C_{ijkl}\{(4\pi)^{-1}\varepsilon^*_{nm}(\hat{x}')C_{klmn}\int_0^{2\pi} d\theta(\hat{\bar{\varsigma}})\int_{-1/y}^{1/y} g_{ijkl}(\hat{\bar{\xi}})d\bar{\xi}_3'$$
$$-(2\pi)^{-1}\varepsilon^*_{nm}(\hat{x}')C_{klmn}\int_0^{2\pi} g_{ijkl}(\hat{\bar{\xi}})y^{-1}d\theta(\hat{\bar{\varsigma}}) - \varepsilon^*_{kl}(\hat{x})\} \quad (4.109)$$

where $\sigma_{ij}(\hat{x})$ shown in Eq. (4.109) is exact the same as $\sigma^{d1}_{ij}(x)$ in Eq. (4.81). With $\sigma^{d1}_{ij}(x)$ obtained, the overall stress field at the boundary of Cavity 2 $\sigma^{t(2)}_{ij}$ can be obtained.

In the special case of disturbed stress field of cavity embedded in isotropic material, an explicit solution can be obtained as below:

$$8\pi(1-\nu)S_{ijkl}(\hat{x}) = \delta_{ij}\delta_{kl}[2\nu I_i(\lambda) - I_k(\lambda) + a_i^2 I_{ik}(\lambda)] +$$
$$(\delta_{ik}\delta_{jl} + \delta_{jk}\delta_{il})\{a_i^2 I_{ij}(\lambda) - I_j(\lambda) + (1-\nu)[I_k(\lambda) + I_l(\lambda)] +$$
$$2\nu\delta_{kl}x_i I_{i,j}(\lambda) + (1-\nu)\{\delta_{ij}x_k I_{k,j}(\lambda) + \delta_{jl}x_k I_{k,i}(\lambda) + \delta_{ik}x_l I_{l,j}(\lambda)$$
$$+\delta_{jk}x_l I_{l,i}(\lambda)\} - (\delta_{ij}x_k + \delta_{ik}x_j + \delta_{jk}x_i)[I_j(\lambda) - a_i^2 I_{ij}(\lambda)]_{,l} -$$
$$(\delta_{il}x_j + \delta_{jl}x_i)[I_j(\lambda) - a_i^2 I_{ij}(\lambda)]_{,k} - x_j x_i[I_j(\lambda) - a_i^2 I_{ij}(\lambda)]_{,lk} \qquad (4.\ 110)$$

where
$$I(\lambda) = 2\pi a_1 a_2 a_3 \int_\lambda^\infty \frac{ds}{\Delta(s)} \qquad (4.\ 111)$$

$$I_i(\lambda) = 2\pi a_1 a_2 a_3 \int_\lambda^\infty \frac{ds}{(a_i^2 + s)\Delta(s)} \qquad (4.\ 112)$$

$$I_{ij}(\lambda) = 2\pi a_1 a_2 a_3 \int_\lambda^\infty \frac{ds}{(a_i^2 + s)(a_j^2 + s)\Delta(s)} \qquad (4.\ 113)$$

where
$$\Delta(s) = \{(a_1^2 + s)(a_2^2 + s)(a_3^2 + s)\}^{1/2} \qquad (4.\ 114)$$

and λ is the largest solution of
$$\frac{x_1^2}{(a_1^2 + \lambda)} + \frac{x_2^2}{(a_2^2 + \lambda)} + \frac{x_3^2}{(a_3^2 + \lambda)} = 1 \qquad (4.\ 115)$$

Eq. (4.110) is identical to the solution given in [146]. Eq. (4.109) can be used to obtain the disturbed stress field of open cell FGPMs with round disk shape and graded porosity, and Eq. (110) can be used to obtain the solution for open cell structure with round disk shape with constant porosity.

Cuboid cavity

In this section, open cell structure with interconnected cuboid inclusions or inhomogeneity are considered. Figure 4.8 shows two interconnected cuboid cavities embedded in matrix, and it is of great interest to obtain the disturbed stress field generated by cuboidal cavity in order to develop analytical model for open cell FGPMs with cuboid cavities. The displacement, stress, and strain fields due to inclusion and inhomogeneity are shown in Eqs. (4.85), (4.90) and (4.91).

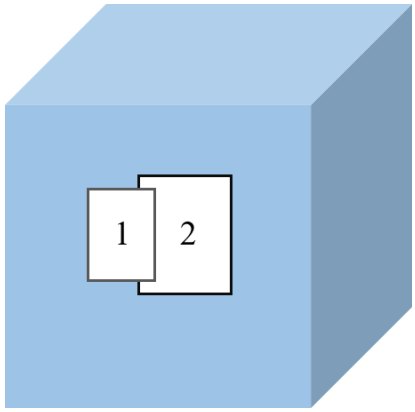

Figure 4. 8 Two interconnected cuboid in matrix

Again, assuming the eigenstrain inside the inclusion or at the boundary of cavity is a constant, where:

$$\varepsilon^{*}_{mn}(\hat{x}^{'}) = \varepsilon^{*0}_{mn} \tag{4. 116}$$

Integrating with respect to $\hat{x}^{'}$ in Eq. (4.90) results in [147]:

$$u_{i,q}(\hat{x}) = i(2\pi)^{-3}\varepsilon^{*0}_{mn}\sum_{p=1}^{8}(-1)^{p}\int_{-\infty}^{\infty} C_{jlmn}\xi_l\xi_q N_{ij}(\hat{\xi})\{\xi_1\xi_2\xi_3 D(\hat{\xi})\}^{-1}\exp\{i\hat{\xi}\cdot\hat{c}_p\}d(\hat{\xi}) \tag{4. 117}$$

where

$$\begin{aligned}
\hat{c}_1 &= (x_1 - a_1, x_2 - a_2, x_3 - a_3)\\
\hat{c}_2 &= (x_1 + a_1, x_2 - a_2, x_3 - a_3)\\
\hat{c}_3 &= (x_1 + a_1, x_2 + a_2, x_3 - a_3)\\
\hat{c}_4 &= (x_1 - a_1, x_2 + a_2, x_3 - a_3)\\
\hat{c}_5 &= (x_1 - a_1, x_2 + a_2, x_3 + a_3)\\
\hat{c}_6 &= (x_1 - a_1, x_2 - a_2, x_3 + a_3)\\
\hat{c}_7 &= (x_1 + a_1, x_2 - a_2, x_3 + a_3)\\
\hat{c}_8 &= (x_1 + a_1, x_2 + a_2, x_3 + a_3)
\end{aligned} \tag{4. 118}$$

An auxiliary equation is defined as follows:

$$f_{ij,kkmm} = \varepsilon^{*}_{mn} \tag{4. 119}$$

After simplification, Eq. (4.117) can be expressed as:

$$u_{i,q}(\hat{x}) = (2\pi)^{-3}\varepsilon^{*0}_{mn}C_{jlmn}\sum_{p=1}^{8}(-1)^{p}J_{iqmm}\int_{\Omega} N_{ik}(\hat{\bar{\xi}})D^{-1}(\hat{\bar{\xi}})\bar{\xi}_l\bar{\xi}_j d(\hat{\bar{\xi}}) \tag{4. 120}$$

where $J_{iqmm}(\hat{c}) = (\partial^4 / \partial x_i\partial x_j\partial x_k\partial x_l)\int_{-\infty}^{\infty} i\exp(i\hat{\xi}\cdot\hat{c})[\xi_1\xi_2\xi_3(\xi_1^2+\xi_2^2+\xi_3^2)]^{-1} d(\hat{\xi})$

(4. 121)

In this work, the problem of two interconnected cuboid cavities is considered, and the solution of disturbed stress field outside a cuboid cavity needs to be obtained.

Define: $$g_{ijkl}(\hat{\bar{\xi}}) = N_{ik}(\hat{\bar{\xi}})D^{-1}(\hat{\bar{\xi}})\bar{\xi}_l\bar{\xi}_j \tag{4. 122}$$

Eq. (4.120) is simplified as:

$$u_{i,q}(\hat{x}) = (2\pi)^{-3}\varepsilon^{*0}_{mn}C_{jlmn}\sum_{p=1}^{8}(-1)^p D_{iqmm}\int_{\Omega} g_{ijkl}(\hat{\bar{\xi}})d(\hat{\bar{\xi}}) \tag{4. 123}$$

$$\sigma_{ij}(\hat{x}) = C_{ijkl}\{(2\pi)^{-3}\varepsilon^{*0}_{mn}C_{jlmn}\sum_{p=1}^{8}(-1)^p D_{iqmm}\int_{\Omega} g_{ijkl}(\hat{\bar{\xi}})d(\hat{\bar{\xi}}) - \varepsilon^{*}_{kl}(\hat{x})\} \tag{4. 124}$$

Eq. (4.124) can be used to obtain the disturbed stress field for open cell structure with square disk void.

4.4 Application of Derived Analytical Model to FGPMs

The extension of Mori-Tanaka's model to "graded" and "porous" FGPMs and open cell structure as discussed in the previous sections is implemented here. Section 4.4.1 listed the Eshelby's tensor for inclusion with different geometries, i.e. spherical inclusion, round disk inclusion, cylindrical inclusion, and cuboidal inclusion. In Section 4.4.2, the Eshelby's tensor under polynomial varying eigenstrain was demonstrated. The application of the above analytical model to FGPMs case will be discussed in Section 4.4.3.

4.4.1 Eshelby's Tensor for Inclusion with Different Geometries in Isotropic Material

When the eigenstrain field is uniform inside the inclusion and the base material is considered as isotropic, Eshelby's tensor has explicit solutions for inclusion with various geometries for direct uses.

Eshelby's tensor has the form as:

$$S_{ijkl} = \begin{bmatrix} S_{1111} & S_{1122} & S_{1133} & 0 & 0 & 0 \\ S_{2211} & S_{2222} & S_{2233} & 0 & 0 & 0 \\ S_{3311} & S_{3322} & S_{3333} & 0 & 0 & 0 \\ 0 & 0 & 0 & 2S_{2233} & 0 & 0 \\ 0 & 0 & 0 & 0 & 2S_{3311} & 0 \\ 0 & 0 & 0 & 0 & 0 & 2S_{1122} \end{bmatrix} \tag{4. 125}$$

For sphere inclusion since $a_1 = a_2 = a_3 = a$, where a_i specify the size of the ellipsoid, and a is the radius of sphere. The expression of Eshelby's tensor was derived as [106]:

$$\begin{aligned} S_{1111} &= S_{2222} = S_{3333} = \frac{7-5\nu}{15(1-\nu)} \\ S_{1212} &= S_{2323} = S_{3131} = \frac{4-5\nu}{15(1-\nu)} \\ S_{1122} &= S_{2233} = S_{3311} = S_{1133} = S_{2211} = S_{3322} = \frac{5\nu-1}{15(1-\nu)} \end{aligned} \tag{4. 126}$$

where ν denotes the Poisson's ratio of the base material.

For elliptic cylinder case where $a_3 \to \infty$,

$$S_{1111} = \frac{1}{2(1-\nu)}\{\frac{a_2^2 + 2a_1a_2}{(a_1+a_2)^2} + (1-2\nu)\frac{a_2}{a_1+a_2}\}$$

$$S_{2222} = \frac{1}{2(1-\nu)}\{\frac{a_1^2 + 2a_1a_2}{(a_1+a_2)^2} + (1-2\nu)\frac{a_1}{a_1+a_2}\}$$

$$S_{1122} = \frac{1}{2(1-\nu)}\{\frac{a_2^2}{(a_1+a_2)^2} - (1-2\nu)\frac{a_2}{a_1+a_2}\}$$

$$S_{2211} = \frac{1}{2(1-\nu)}\{\frac{a_1^2}{(a_1+a_2)^2} - (1-2\nu)\frac{a_1}{a_1+a_2}\}$$

$$S_{1212} = \frac{1}{2(1-\nu)}\{\frac{a_1^2 + a_2^2}{2(a_1+a_2)^2} + \frac{1-2\nu}{2}\}$$

$$S_{2323} = \frac{a_1}{2(a_1+a_2)}\ ,\ S_{3131} = \frac{a_2}{2(a_1+a_2)}$$

$$S_{3333} = 0\ ,\ S_{3311} = 0\ ,\ S_{3322} = 0$$

$$S_{1133} = \frac{1}{2(1-\nu)}\frac{2\nu a_2}{(a_1+a_2)}$$

$$S_{2233} = \frac{1}{2(1-\nu)}\frac{2\nu a_1}{(a_1+a_2)} \qquad (4.\ 127)$$

For penny-shaped inclusion where $a_1 = a_2 >> a_3$,

$$S_{1111} = S_{2222} = \frac{13-8\nu}{32(1-\nu)}\pi\frac{a_3}{a_1}\ ,\ S_{3333} = 1 - \frac{1-2\nu}{1-\nu}\frac{\pi}{4}\frac{a_3}{a_1}$$

$$S_{1122} = S_{2211} = \frac{8\nu-1}{32(1-\nu)}\pi\frac{a_3}{a_1}\ , S_{1133} = S_{2233} = \frac{2\nu-1}{8(1-\nu)}\pi\frac{a_3}{a_1}$$

$$S_{3311} = S_{3322} = \frac{\nu}{1-\nu}(1 - \frac{4\nu+1}{8\nu}\pi\frac{a_3}{a_1}) \qquad (4.\ 128)$$

$$S_{1212} = \frac{7-8\nu}{32(1-\nu)}\pi\frac{a_3}{a_1},\ S_{1313} = S_{2323} = \frac{1}{2}(1+\frac{\nu-2}{1-\nu}\frac{\pi}{4}\frac{a_3}{a_1})$$

For cuboidal inclusion where side lengths are $2a_1$, $2a_2$, and $2a_3$ respectively, Garlekin vector method were used to obtain the stress and strain fields inside the inclusion embedded in isotropic material.

Under isotropic material condition, $D(\hat{\xi})$ and $N_{ij}(\hat{\xi})$ can be expressed as:

$$D(\hat{\xi}) = \mu^2(\lambda+2\mu)\xi^6 \tag{4. 129}$$

$$N_{ij}(\hat{\xi}) = \mu^2\xi^2\{(\lambda+2\mu)\delta_{ij}\xi^2 - (\lambda+\mu)\xi_i\xi_j\} \tag{4. 130}$$

where λ and μ are Lame constants.

Therefore, Eqs. (4.117-4.118) can be reduced to:

$$u_{i,q}(\hat{x}) = (2\pi)^{-3}\sum_{p=1}^{8}(-1)^p[\frac{\nu}{1-\nu}\varepsilon_{kk}^{*}D_{iqmm}(\hat{c}_n) + 2\varepsilon_{ij}^{*}D_{iqmm}(\hat{c}_n) - \frac{1}{1-\nu}\varepsilon_{mj}^{*}D_{iqmm}(\hat{c}_n) \tag{4. 131}$$

where ε_{kk}^{*} denotes the volumetric eigenstrain, ε_{ij}^{*} denotes the deviatoric eigenstrain component, p denotes as vertices of cuboid, and D_{iqmm} is given in [147].

4.4.2 Eshelby's Tensor under Polynomial Varying Eigenstrain Field

For a general case, Eshelby's tensor can be calculated as [144]:

$$S_{1111} = \frac{3}{8\pi(1-\nu)} a_1^2 I_{11} + \frac{1-2\nu}{8\pi(1-\nu)} I_1$$

$$S_{1122} = \frac{1}{8\pi(1-\nu)} a_2^2 I_{12} - \frac{1-2\nu}{8\pi(1-\nu)} I_1 \qquad (4.\ 132)$$

$$S_{1133} = \frac{1}{8\pi(1-\nu)} a_3^2 I_{13} - \frac{1-2\nu}{8\pi(1-\nu)} I_1$$

$$S_{1212} = \frac{a_1^2 + a_2^2}{16\pi(1-\nu)} I_{12} + \frac{1-2\nu}{16\pi(1-\nu)} (I_1 + I_1)$$

Other components can be obtained by the cyclic permutation of the above equations.

For Eshelby's tensor with polynomial eigenstrain, the I-integral are given as shown in Eq. (133) [148]:

$$I_1 = 4\pi a_1 a_2 a_3 (a_1^2 - a_2^2)^{-1} (a_1^2 - a_3^2)^{-1/2} \{F(\theta,k) - E(\theta,k)\}$$

$$I_2 = 4\pi a_1 a_2 a_3 \{(a_1^2 - a_3^2)^{1/2} (a_1^2 - a_2^2)^{-1} (a_2^2 - a_3^2)^{-1} E(\theta,k)$$

$$-(a_1^2 - a_2^2)^{-1} (a_1^2 - a_3^2)^{-1/2} F(\theta,k)$$

$$-(a_2^2 - a_3^2)^{-1} (\lambda + a_3^2)^{1/2} (\lambda + a_1^2)^{-1/2} (\lambda + a_2^2)^{-1/2}\}$$

$$I_3 = 4\pi a_1 a_2 a_3 (a_1^2 - a_3^2)^{-1/2} (a_2^2 - a_3^2)^{-1} \{(a_2^2 + \lambda)^{1/2}$$

$$\times (a_1^2 - a_3^2)^{-1/2} (a_3^2 + \lambda)^{-1/2} (a_1^2 + \lambda)^{-1/2} - E(\theta,k)\}$$

$$3I_{11} = 4\pi a_1^2 a_2^2 a_3^2 / (a_1^2) - I_{12} - I_{13}$$

$$I_{12} = (I_2 - I_1) / (a_1^2 - a_2^2)$$

$$I_{13} = (I_{13} - I_{11}) / (a_1^2 - a_3^2) \qquad (4.\ 133)$$

where $F(\theta,k)$, $E(\theta,k)$, θ, and k are defined below:

$$F(\theta,k)=\int_0^{\theta}\frac{dw}{(1-k^2\sin^2 w)^{1/2}} \tag{4. 134}$$

$$E(\theta,k)=\int_0^{\theta}(1-k^2\sin^2 w)^{1/2}dw \tag{4. 135}$$

$$\theta=\sin^{-1}(1-a_3^2/a_1^2)^{1/2} \tag{4. 136}$$

$$k=\{(a_1^2-a_2^2)/(a_1^2-a_3^2)\}^{1/2} \tag{4. 137}$$

4.4.3 Analytical Model Applied to FGPMs Cases

To show to application of the derived model, consider the case of FGPMs with linearly varying porosity; and according to the above derivation, the stress, strain fields, and the perturbation fields are also linearly varying fields. Thus, Eq. (4.52) is simplified to:

$$\Delta\varepsilon=\Delta\varepsilon_0+\sum_{j=1}^{3}(x_j-\overline{x}_j)g_j^{\Delta} \tag{4. 138}$$

$$\Delta\varepsilon=H_0\sigma+\sum_{i=1}^{3}\sum_{j=1}^{3}(x_j-\overline{x}_j)R_{ij}\sigma \tag{4. 139}$$

where $\Delta\varepsilon_0$ denotes the average strain applied, x_j is the position in j direction, $\overline{x}_j$ is the centroid of the cavity, g_j^{Δ} is the perturbed strain gradient, and R_{ij} is the cavity compliance gradient tensor (a 6×6 matrix). Thus, Eq. (4.55) becomes:

$$\begin{aligned}
\Delta\varepsilon_0 &= H_0\sigma_0 \\
k_1 &= R_{11}\sigma_{ij} + R_{12}\sigma_{ij} + R_{13}\sigma_{ij} \\
k_2 &= R_{21}\sigma_{ij} + R_{22}\sigma_{ij} + R_{23}\sigma_{ij} \\
k_3 &= R_{31}\sigma_{ij} + R_{32}\sigma_{ij} + R_{33}\sigma_{ij}
\end{aligned} \tag{4. 140}$$

where $\Delta\varepsilon_0$, k_1, k_2, and k_3 are all 6×1 vectors, and k_1, k_2, and k_3 denote the varying gradient term of the perturbed strain field.

Similarly, the strain field on the boundary of cavity is a combination of the linearly varying applied strain field and the corresponding linearly varying perturbation strain field as shown in Eq. (4.141):

$$\varepsilon^{(1)}(x) = \varepsilon_0^{(0)} + \sum_{i=1}^{3} x_i g^{(0)}(x) + \Delta\varepsilon_0 + \sum_{j=1}^{3} (x_j - \overline{x_j}) g_j^{(\Delta)}(x) \tag{4. 141}$$

Eq. (4.141) can be written as $\varepsilon_{ij}^{(1)}(x) = M\varepsilon^{(0)} + N\Delta\varepsilon$ (4. 142)

where

$$\begin{aligned}
M &= I + \sum_{i=1}^{3} x_i g^{(0)}(x) / \varepsilon_0^{(0)} I \\
N &= I + \sum_{j=1}^{3} (x_j - \overline{x_j}) g_j^{(\Delta)}(x) / \Delta\varepsilon_0 I
\end{aligned} \tag{4. 143}$$

where *I* is the unit vector.

Thus, Eq. (4.141) retains in the linearly varying porosity field case, with

$$T = M + N\beta \tag{4. 144}$$

where *M*, *N* are defined in Eq. (4.143) and β is defined in Eq. (4.65).The effective stiffness of FGPMs with linearly varying porosity field can be derived as:

$$L^{*} = L^{(0)}[I + \sum_{r=2}^{N} c_r \beta]A \tag{4. 145}$$

with A defined in Eq. (4.79).

The FGPMs with linearly varying porosity are commonly used, and the above derived equations can be used to obtain their effective stiffness. For slightly non-linearly gradient FGPMs, the above equations could still be used if their porosity fields can be approximated as linear distribution.

The derived analytical model was implemented to obtain the effective stiffness of the experimentally fabricated FGPMs. The stiffness and Poisson's ratio of base material is assumed to be $L^{(0)}$ and ν, respectively.

For 3-D case, the integral of Eq. (4.45) can be obtained in terms of Eshelby's tensor:

$$\varepsilon_{ij} - S_{ijkl}\Delta\varepsilon = L^{(0)}\sigma_0 \tag{4. 146}$$

where ε_{ij} and $\Delta\varepsilon$ denote the strain field at the cavity boundary and the perturbation strain field due to the presence of cavities, respectively, S_{ijkl} denotes Eshelby's tensor, and σ_0 denotes the applied stress.

The displacement u at the cavity boundary in Eq. (4.45) follows $u_i = \varepsilon_{ij} x$ where x is the position coordinate, and the integral in Eq. (4.45) can be obtained from [127]:

$$H_{ijkl} = \frac{V_p}{V}\frac{1}{E_0}\begin{bmatrix} H_{1111} & H_{1122} & H_{1133} & 0 & 0 & 0 \\ H_{2211} & H_{2222} & H_{2233} & 0 & 0 & 0 \\ H_{3311} & H_{3322} & H_{3333} & 0 & 0 & 0 \\ 0 & 0 & 0 & H_{2323} & 0 & 0 \\ 0 & 0 & 0 & 0 & H_{3131} & 0 \\ 0 & 0 & 0 & 0 & 0 & H_{1212} \end{bmatrix} \quad (4.\ 147)$$

where V_p and V denote total volume of the cavities and overall material, respectively, E_0 denotes the Young's modulus of the base material, and H_{ijkl} can be obtained in terms of Eshelby's tensor.

The overall effective stiffness of FGPMs was obtained through homogenization process using the above analytical model. The normalized effective stiffness obtained will later be compared with the results from numerical simulation in order to verify the prediction accuracy.

4.5 Numerical Modeling of FGPMs

Finite element analysis is carried out using commercial software Abaqus in order to (1) investigate the mechanical response and stress distribution of the FGPMs for both closed and open cell structures, (2) obtain the effective stiffness of overall material. The results from numerical model are used to compare with experimental results and analytical results.

In section 4.5.1, the periodic boundary condition (PBC) for FGPMs under normal stress (or strain) and shear stress (or strain) are described. Section 4.5.2 discusses the details about the numerical model for FGPMs and the implementation of PBC on an RVE.

4.5.1 Periodic Boundary Condition for FGPMs

In order to predict the material property of FGPMs, a representative volume element (RVE) is modeled and a periodic boundary condition (PBC) is applied [149]. RVE should be chosen properly such that its size is sufficiently large enough for representing all the geometry information but also relative small enough to be investigated analytically and numerically. For composite material that can be considered as heterogeneous material, the stress and strain fields of RVE should be identical to that of the overall material.

The procedure of obtaining effective elastic property using FEA is listed as follows: (1) a proper RVE should be chosen, and corresponding PBC should be determined and applied, i.e. in Abaqus, it is applied through “constraint” module using “equation” function. (2) the non-homogeneous stress and strain fields should be transformed to volume-average stress and strain using:

$$\bar{\sigma}_{ij} = \frac{1}{V}\int_V \sigma_{ij}(x,y,z)dV \tag{4. 148}$$

$$\bar{\varepsilon}_{ij} = \frac{1}{V}\int_V \bar{\varepsilon}_{ij}(x,y,z)dV \tag{4. 149}$$

Alternatively, in Abaqus, a short programming can be used to calculate the volume average stress/strain. (3) Now that the stress-strain, and load-displacement relationships are obtained, the corresponding effective modulus can also be determined.

Periodic boundary conditions under normal stress or strain

In order to acquire the effective elastic modulus, the response of the material under externally applied normal load and displacement needs to be obtained. Figure 9 shows a typical 3-D cuboidal unit cell, the lengths of edge in x, y, and z direction are $2a_0$, $2b_0$, and $2c_0$, respectively. The origin of the coordinate lies at (0, 0, 0). In order to obtain the effective modulus E_x^* in x direction, the displacement boundary condition for the pair of plane $x = a_0$ and $x = -a_0$ can be applied as:

$$\begin{aligned} u\big|_{x=a_0} - u\big|_{x=-a_0} &= 2\varepsilon_x a_0 \\ v\big|_{x=a_0} - v\big|_{x=-a_0} &= 0 \\ w\big|_{x=a_0} - w_{x=-a_0} &= 0 \end{aligned} \tag{4. 150}$$

for the pair of plane $y = b_0$ and $y = -b_0$

$$
\begin{aligned}
u\big|_{x=a_0} - u\big|_{x=-a_0} &= 0 \\
v\big|_{x=a_0} + v\big|_{x=-a_0} &= 0 \\
w\big|_{x=a_0} - w_{x=-a_0} &= 0
\end{aligned}
\tag{4. 151}
$$

for the pair of plane $z = c_0$ and $z = -c_0$

$$
\begin{aligned}
u\big|_{x=a_0} - u\big|_{x=-a_0} &= 0 \\
v\big|_{x=a_0} - v\big|_{x=-a_0} &= 0 \\
w\big|_{x=a_0} + w_{x=-a_0} &= 0
\end{aligned}
\tag{4. 152}
$$

Alternatively, if consider the plane of symmetry of the RVE, when an RVE subjected to a macroscopic externally applied stress σ_x^0, the boundary conditions of three pairs opposite planes are given by [150]:

$$u\big|_{x=0} = 0 \text{ and } u\big|_{x=a_0} = \varepsilon_x a_0 \quad \text{(Applied displacement)} \tag{4. 153}$$

$$u\big|_{y=0} = 0 \text{ and } u\big|_{y=b_0} = \varepsilon_y b_0 \quad \text{(Free to flow)} \tag{4. 154}$$

$$u\big|_{z=0} = 0 \text{ and } u\big|_{x=c_0} = \varepsilon_c c_0 \quad \text{(Free to flow)} \tag{4. 155}$$

where Eq. (4.153) is the externally applied displacement boundary condition, and the second terms in Eqs. (4.154) and (4.155) should be left free in order to satisfy the uniaxial stress state.

Thus, for the problem of displacement input as $u\big|_{x=a_0}(x, y, z) = u(2\varepsilon_x a_0, y, z)$, and the boundary conditions shown in Eqs. (4.154) and (4.155), the solution in terms of

stress field can be obtained from Abaqus simulation. Once the volume average stress $\bar{\sigma}_x$ is calculated, the effective modulus E_x^* is obtained by:

$$E_x^* = \frac{\bar{\sigma}_x}{2\varepsilon_x} \tag{4. 156}$$

Similarly, the same principle and procedure can be used to obtain the effective elastic modulus in other two directions.

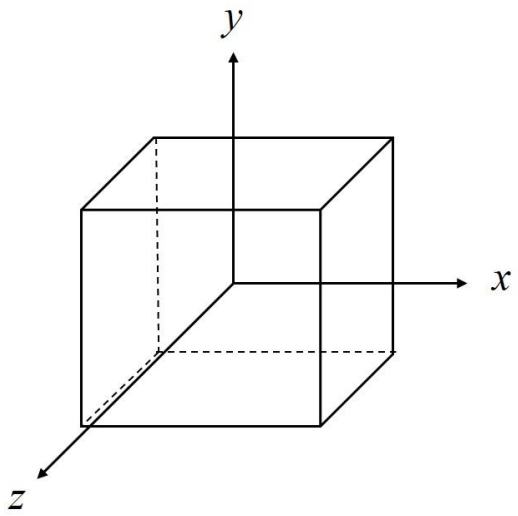

Figure 4. 9 A cuboid RVE

Periodic boundary conditions under shear stress or strain

Considering a cuboid RVE as shown in Figure 4.9 subjected to externally applied shear stress τ_{xy}^0 . In order to obtain the effective modulus G_{xy}^* in x-y direction, the

displacement boundary conditions for the pair of plane perpendicular to x direction can be expressed as below:

On the plane where $x=0$ and $x=a_0$ it follows:

$$v\big|_{x=0}=0 \text{ and } w\big|_{x=0}=0 \tag{4. 157}$$

$$v\big|_{x=a_0}=b_0\gamma_{xy} \text{ and } w\big|_{x=a_0}=0 \tag{4. 158}$$

On the plane where $y=0$ and $y=b_0$ it follows:

$$u\big|_{y=0}=0 \text{ and } w\big|_{y=0}=0 \tag{4. 159}$$

$$u\big|_{y=b_0}=a_0\gamma_{xy} \text{ and } w\big|_{y=b_0}=0 \tag{4. 160}$$

On the plane where $z=0$ and $z=c_0$ it follows:

$$w\big|_{z=0}=0 \tag{4. 161}$$

$$w\big|_{z=c_0}=0 \tag{4. 162}$$

Note the above boundary conditions is different from [150], where it sets $v\big|_{x=a_0}=0$ on the plane of $x=a_0$. Here $v\big|_{x=a_0}$ is not zero; it either equals $b_0\gamma_{xy}$ or can be set free since it is also subjected to externally applied shear stress τ_{xy}^0.

Once the solution in terms of strain field is obtained from Abaqus simulation and volume average strain $\overline{\gamma}_{xy}$ is calculated, the effective modulus E_x^* is obtained by:

$$G_{xy}^*=\frac{\tau_{xy}^0}{\overline{\gamma}_{xy}} \tag{4. 163}$$

4.5.2 Finite Element Analysis for FGPMs

The compression test and shear test simulations of the developed FGPMs are conducted using ABAQUS in order to investigate the overall material behavior under different loading conditions. The simulation follows exactly the same geometry of the specimen and the same loading condition.

3-D RVE models are built to simulate the compression and shear tests of FGPMs for each configuration. Figure 4.10 demonstrates the RVE model for Configuration 7 (open cell with round disk void and graded porosity). The 8 single layers with different pore sizes were built up to simulate the same material tested in experiments. Perfect bonding between the layers were assumed and the implicit analysis was used in both the compression and shear tests. The element type was set as 3D stress quadratic tetrahedral (Tet) C3D10 for configurations with round disk shaped void in order to generate equal mesh on the opposite faces to apply PBC. The element type of linear 3D stress and reduced integration C3D8R was utilized for configurations with square disk. In all the simulations, displacement control was used. Two dimensional PBC was used since the FGPMs are periodic in x and y direction as shown in Figure 4.10. And the PBC was used based on “Equation” function and was implemented by an input Python code. In the compression test simulation, the displacement in x, y, and z directions were fixed on one

face and allowing the opposite face to flow freely. In the shear test simulation the pure shear testing condition was used in order to obtain the shear moduli.

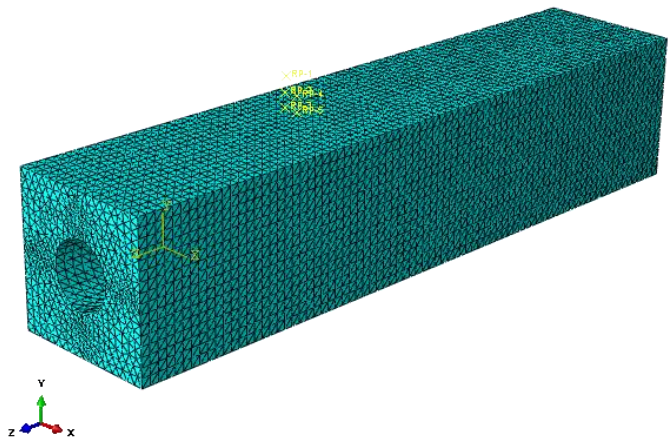

Figure 4. 10 3D RVE model for Configuration 7

Simulations were conducted on 3-D printed Polylactic acid (PLA) materials, and the material property input in the simulation was obtained from experimental compression test. The elastic modulus of PLA is 986.27 MPa, and Poisson's ratio is 0.34. The base materials were considered as isotropic and incompressible. The volume average stress data was collected after the simulation, and the effective moduli were obtained using the volume average stress divided by volume average strain.

5. ANALYTICAL AND NUMERICAL RESULTS

In Section 5, the results for analytical and numerical model derived in Section 4 are presented. The models are validated by experimental results, and the prediction accuracy is evaluated.

In Section 5.1, analytical and numerical results for predicting effective Young's moduli are shown, a comparison with experimental results and a discussion of prediction accuracy based on different factors is provided. Section 5.2 presents the analytical and numerical results for effective shear moduli.

5.1 Analytical and Numerical Results for Effective Young's Moduli

In Section 5.1.1, the analytical and numerical results are presented. Sections 5.1.2 to 5.1.4 provide a detailed discussion of the effects of geometry, porosity distributions, and cell structures (open cell/closed cell) on the prediction accuracy of analytical models.

5.1.1 Effective Young's Moduli from Analytical and Numerical Model

The effective Young's moduli for each configuration were obtained through numerical modeling using RVE based periodic boundary condition (PBC). Python programming was used to generate PBC. Taking Configuration 7 as an example, Figure 5.1 demonstrates the section view of the stress contour of the RVE for a graded, open cell structure with round disk voids subjected to σ_{33}. It is observed that near the round disk void, the stress level is higher while further away from it the stress level becomes the average stress. With an increase in the size of void, the stress level also increases as can be seen by comparing the right part of the specimen with the left side where the size of the void is smaller. Similarly, the trend can be seen from Figure 5.2 which depicts the section view of the stress contour of the RVE for a graded, open cell structure with round disk voids (Configuration 7) subjected to σ_{22}. The effective modulus was obtained by the volume average stress divided by volume average strain.

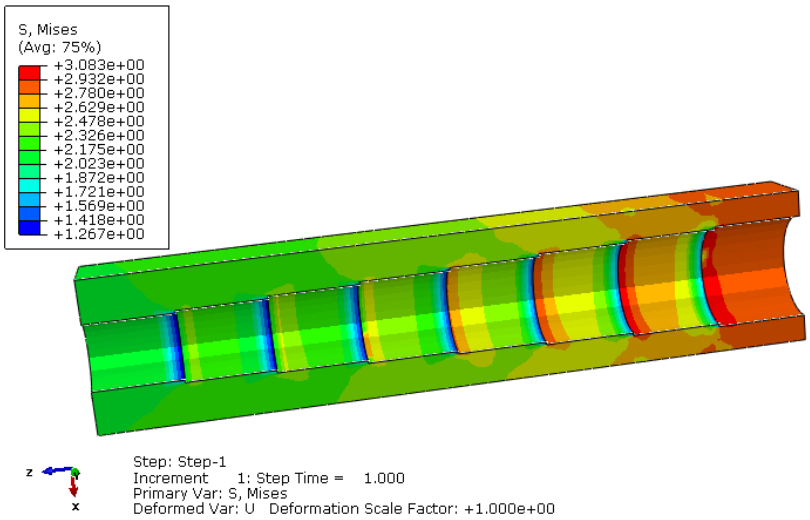

Figure 5. 1 Stress contour of σ_{33} for a graded, open cell structure with round disk voids (section view)

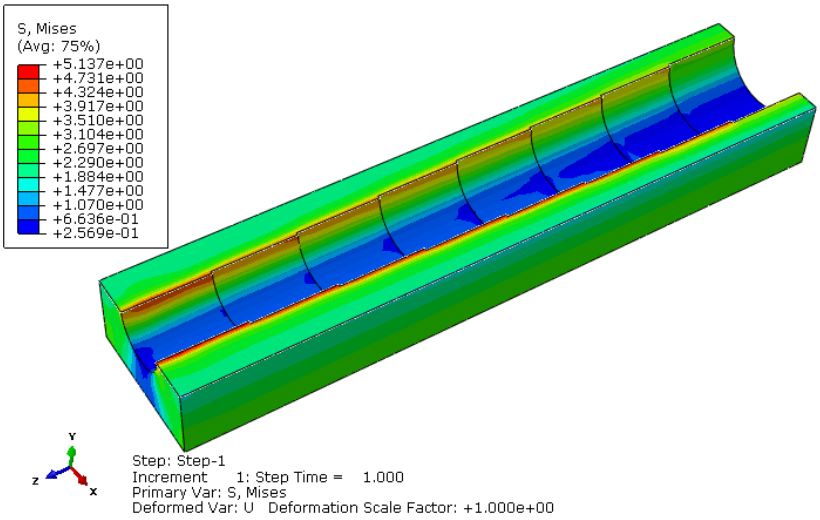

Figure 5. 2 Stress contour plot of σ_{22} for graded, open cell structure with round disk voids (section view)

The extension of Mori-Tanaka's model to closed cell graded porous material and open cell graded porous material was implemented, and the results are compared with experimental and numerical results as a validation. Figures 5.3 and 5.4 show the comparison of normalized effective moduli from experimental, analytical, and numerical results for closed cell structures, i.e. Configurations 1,3, 5, and 7. The normalized effective modulus is defined as the effective modulus divided by modulus of base material (in this work, it is 986.27 MPa), where the normalized effective modulus falls in the range (0, 1]. It is observed that a good agreement was achieved among the experimental, analytical, and numerical results, indicating that the analytical model and numerical model can predict the material response of FGPMs with good accuracy. Note that overall, the experimental data are lower than analytical and numerical results, this is due to the porous nature of 3-D printing specimens, which might have lower porosity than the input 3D model. The effect of this issue on verifying the prediction accuracy of analytical and numerical model will be further discussed in Section 5.1.2.

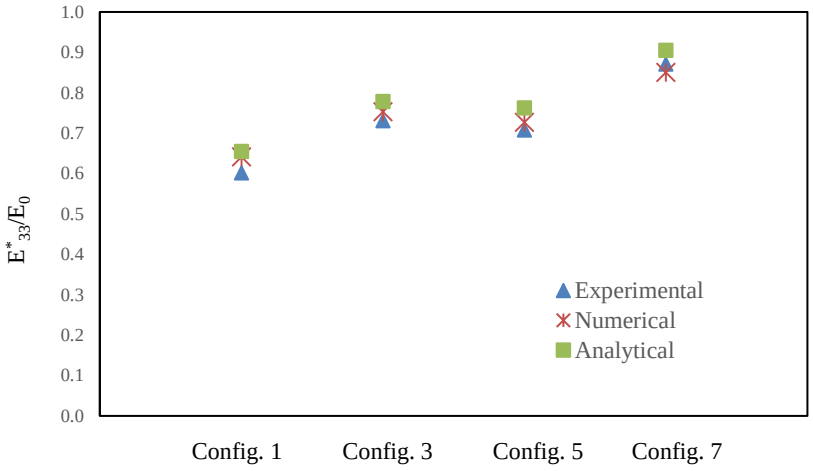

Figure 5. 3 Comparison for E_{33} for closed cell structure

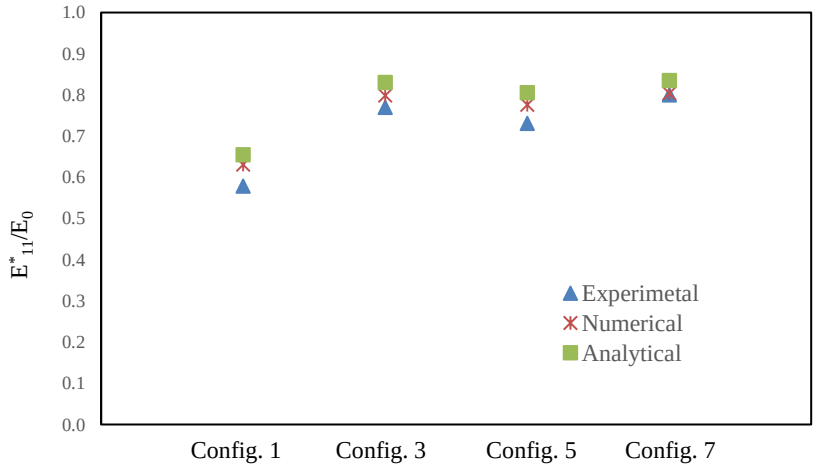

Figure 5. 4 Comparison for E_{11} for closed cell structure

Figures 5.5 and 5.6 show the comparison of normalized effective moduli from experimental, analytical, and numerical results for open cell structures, i.e.

Configurations 2, 4, 6, and 8. As can be seen, a good agreement was achieved which indicates that the analytical model with an extension of Mori-Tanaka's scheme to open cell porous structure can accurately predict its mechanical property.

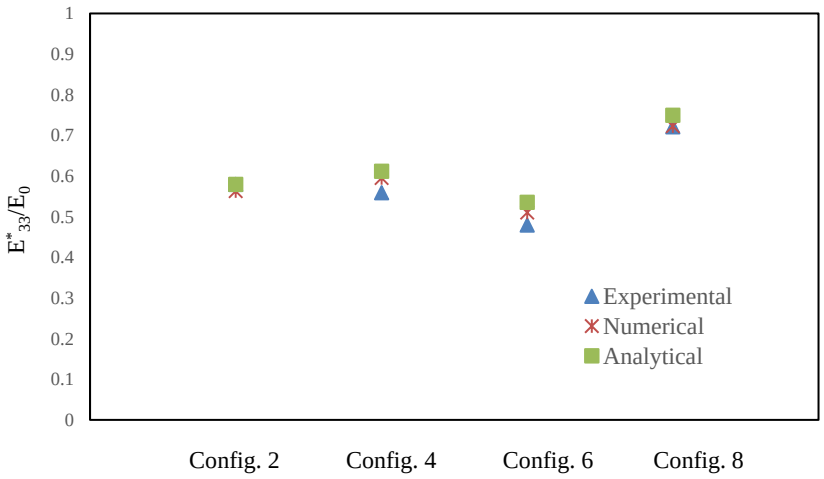

Figure 5. 5 Comparison for E_{33} for open cell structure

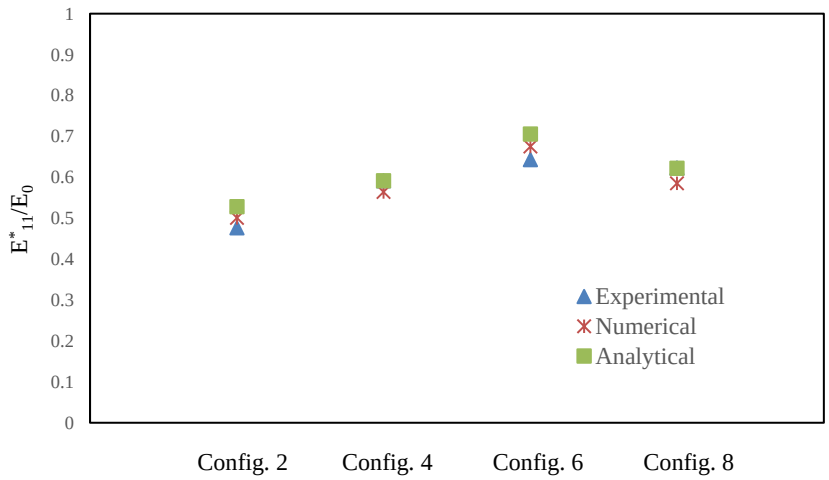

Figure 5. 6 Comparison for E_{11} for open cell structure

Tables 5.1 and 5.2 show experimental data of closed cell structure and open cell structures, respectively. E_{eff} and E_{normal} denote the effective modulus and normalized effective modulus, respectively. The discrepancy between analytical and numerical results and experimental data were calculated and tabulated. It was observed that the discrepancy between analytical and numerical results with experimental data is larger for round disk shape compared to square disk shape for almost all the configurations. This is due to the nature of FDM 3-D printed round shape feature. It is hard to achieve 100% of infill and it will leave some space unfilled, comparing to printing a square shape feature. It is also found that the discrepancy for analytical and numerical results compared to experimental data is generally smaller for graded material than that for constant material.

Table 5. 1 Comparison of experimental, analytical, and numerical

for closed cell structure

Round disk_constant_closed cell								
	Experimental		Analytical			Numerical		
	E_{eff} (Mpa)	E_{normal}	E_{eff} (Mpa)	E_{normal}	Discrepancy with experiment	E_{eff} (Mpa)	E_{normal}	Discrepancy with experiment
E33	593.298	0.602	645.892	0.655	8.865%	632.506	0.641	6.608%
E11	571.156	0.579	646.345	0.655	13.164%	622.527	0.631	8.994%
Round disk_graded_closed cell								
	Experimental		Analytical			Numerical		
	E_{eff} (Mpa)	E_{normal}	E_{eff} (Mpa)	E_{normal}	Discrepancy with experiment	E_{eff} (Mpa)	E_{normal}	Discrepancy with experiment
E33	721.160	0.731	768.193	0.779	6.522%	742.843	0.753	3.007%
E11	759.170	0.770	819.068	0.830	7.890%	787.856	0.799	3.779%
Square disk_constant_closed cell								
	Experimental		Analytical			Numerical		
	E_{eff} (Mpa)	E_{normal}	E_{eff} (Mpa)	E_{normal}	Discrepancy with experiment	E_{eff} (Mpa)	E_{normal}	Discrepancy with experiment
E33	698.366	0.708	752.224	0.763	7.712%	717.169	0.727	2.692%
E11	721.235	0.731	794.268	0.805	10.126%	765.382	0.776	6.121%
Square disk_graded_closed cell								
	Experimental		Analytical			Numerical		
	E_{eff} (Mpa)	E_{normal}	E_{eff} (Mpa)	E_{normal}	Discrepancy with experiment	E_{eff} (Mpa)	E_{normal}	Discrepancy with experiment
E33	859.310	0.871	893.260	0.906	3.951%	838.925	0.851	-2.372%
E11	788.952	0.800	823.560	0.835	4.387%	793.322	0.804	0.554%

Table 5. 2 Comparison of experimental, analytical, and numerical

for open cell structure

Round disk_constant_open cell								
	Experimental		Analytical			Numerical		
	E_{eff} (Mpa)	E_{normal}	E_{eff} (Mpa)	E_{normal}	Discrepancy with experiment	E_{eff} (Mpa)	E_{normal}	Discrepancy with experiment
E33	571.384	0.579	571.789	0.580	0.071%	555.658	0.563	-2.752%
E11	469.948	0.476	520.896	0.528	10.841%	494.480	0.501	5.220%
Round disk_graded_open cell								
	Experimental		Analytical			Numerical		
	E_{eff} (Mpa)	E_{normal}	E_{eff} (Mpa)	E_{normal}	Discrepancy with experiment	E_{eff} (Mpa)	E_{normal}	Discrepancy with experiment
E33	551.488	0.559	603.256	0.612	9.387%	586.860	0.595	6.414%
E11	583.844	0.592	583.246	0.591	-0.102%	556.977	0.565	-4.602%
Square disk_constant_open cell								
	Experimental		Analytical			Numerical		
	E_{eff} (Mpa)	E_{normal}	E_{eff} (Mpa)	E_{normal}	Discrepancy with experiment	E_{eff} (Mpa)	E_{normal}	Discrepancy with experiment
E33	472.926	0.480	528.249	0.536	11.698%	503.028	0.510	6.365%
E11	634.676	0.644	696.548	0.706	9.749%	665.924	0.675	4.924%
Square disk_graded_open cell								
	Experimental		Analytical			Numerical		
	E_{eff} (Mpa)	E_{normal}	E_{eff} (Mpa)	E_{normal}	Discrepancy with experiment	E_{eff} (Mpa)	E_{normal}	Discrepancy with experiment
E33	711.312	0.721	739.286	0.750	3.933%	713.306	0.723	0.280%
E11	614.837	0.623	613.906	0.622	-0.151%	577.587	0.586	-6.059%

5.1.2 Discussion: the Prediction Accuracy Comparison of Different Geometries

As mention above, the effective modulus of FGPMs not only depends on overall porosity, but is also closely related to porosity distribution, the shape of voids, and their location. On the experimental side, the printing accuracy of FDM is also affected by the geometry of the model. When printing single layers of round shape void, due to the trajectory of the nozzle, it is observed that at some locations, the space is not fully filled by the filament material as shown in Figure 5.7. As such, the real porosity of the FGPMs specimen is higher than that of the designed porosity. Therefore, the effective moduli of the FGPMs specimens can be lower than that of the model predictions.

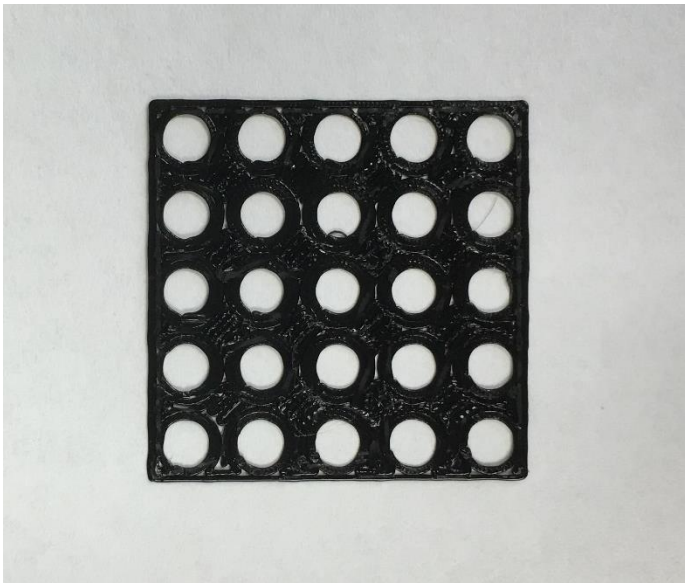

Figure 5. 7 Single layer with round shape void

In order to better evaluate the prediction accuracy of analytical model, the discrepancy between analytical results and numerical results for each configuration were calculated as shown in Tables 5.3 to 5.6. Comparing Table 5.3 with Table 5.4, and Table 5.5 with Table 5.6, it can be observed that the discrepancy between analytical results and numerical results for square shaped void is higher than that for round shape void. This could be due to the accuracy of Eshelby's tensor for inclusions with different shapes. It is known that Eshelby's tensor was initially derived from ellipsoidal shaped inclusion (in which the strain inside the inclusion is uniform) with very good prediction. The Eshelby's tensor was then derived for different shapes, e.g. elliptical cylinder, penny-shaped spheroid, oblate spheroid, prolate spheroid, cuboid, and polygonal shapes, where the initial "condition" for ellipsoidal inclusion becomes an "approximation" for some geometries.

Table 5. 3 Comparison of numerical and analytical results for closed cell round disk

	Round disk_constant_closed cell			Round disk_graded_closed cell		
	Numerical	Analytical	Discrepancy with Numerical	Numerical	Analytical	Discrepancy with Numerical
E33	0.641	0.655	2.116%	0.753	0.779	3.413%
E11	0.631	0.655	3.826%	0.799	0.830	3.962%

Table 5. 4 Comparison of numerical and analytical results for

closed cell square disk

	Square disk_constant_closed cell			Square disk_graded_closed cell		
	Numerical	Analytical	Discrepancy with Numerical	Numerical	Analytical	Discrepancy with Numerical
E33	0.727	0.763	4.888%	0.851	0.906	6.477%
E11	0.776	0.805	3.774%	0.804	0.835	3.812%

Table 5. 5 Comparison of numerical and analytical results for

open cell round disk

	Round disk_constant_open cell			Round disk_graded_open cell		
	Numerical	Analytical	Discrepancy with Numerical	Numerical	Analytical	Discrepancy with Numerical
E33	0.563	0.580	2.903%	0.595	0.612	2.794%
E11	0.501	0.528	5.342%	0.565	0.591	4.716%

Table 5. 6 Comparison of numerical and analytical results for

open cell square disk

	Square disk_constant_open cell			Square disk_graded_open cell		
	Numerical	Analytical	Discrepancy with Numerical	Numerical	Analytical	Discrepancy with Numerical
E33	0.510	0.536	5.014%	0.723	0.750	3.642%
E11	0.675	0.706	4.599%	0.586	0.622	6.288%

In order to confirm this idea or explanation, the comparison of analytical and numerical results for closed cell spherical void, which is the exactly condition how Eshelby's tensor was derived initially [106], is demonstrated in Table 5.7. It can be seen that the discrepancy is within 3%, indicating an accurate solution of Eshelby's tensor for ellipsoidal inclusion. However, for cuboidal inclusion, the analytical solution to Eshelby's tensor was obtained through Galerkin method, which can be considered as an approximated solution. On the other hand, singularity exists for certain edges and corners of the cuboid, which will also cause discrepancy. Under this condition, the prediction of mechanical behavior of FGPMs with round disk void can be more accurate than that with square disk void. However, as can be seen from Tables 5.4 and 5.6, the discrepancy is within 7%, which is quite accurate.

Table 5. 7 Comparison of numerical and analytical results for closed cell spherical void

	Sphere_constant_closed cell			Sphere_graded_closed cell		
	Numerical	Analytical	Discrepancy with numerical	Numerical	Analytical	Discrepancy with numerical
E33	802.175	786.225	-1.988%	725.108	710.805	-1.972%
E11	802.175	786.225	-1.988%	744.358	724.321	-2.692%

5.1.3 Discussion: the Prediction Accuracy Comparison of Constant and Graded Configurations

For graded specimens (Configurations 3, 4, 7, and 8), it can be observed that the predication discrepancy between analytical model and numerical model is within 7%, indicating that the analytical model derived in Section 4 can predict material property well. However, when considering the constant porosity case and graded porosity case, as can be observed from Tables 5.3 to 5.7, the discrepancy of graded porosity case is generally higher than that of constant porosity case. This could partially due to the fact that there are variations of the solution to Eshelby's tensor under polynomial varied eigenstrain condition (as discussed in Section 4.4.2) that leads to some inaccurate results. This could also due to the fact that the Mori-Tanaka's model is a better prediction tool for composite with relative low volume fraction of inclusions or inhomogeneity. However, as discussed by Christensen [51], this model might not be able to yield accurate prediction for high concentration of inclusion or inhomogeneity case since the strain concentration tensor for high concentration of inclusion/inhomogeneity case is obtained by "matrix operations." Therefore, when the porosity of FGPMs is high, the accuracy of model prediction could decrease.

5.1.4 Discussion: the Prediction Accuracy Comparison of Closed Cell and Open Cell Structure

An extension of Mori-Tanaka's scheme to open cell FGPMs is discussed in Section 4, and as can be seen from Tables 5.5 and 5.6, the analytical model yields good prediction accuracy. The idea of the derivation is to find an "equivalent eigenstrain" of the interconnected voids through obtaining the individual eigenstrain for each voids with the consideration of disturbed stress field outside each void. However, comparing the discrepancy in Tables 5.5 and 5.6 to that in Tables 5.3 and 5.4, there is slight but still observable larger discrepancy for open cell structures. This could be due to that the equivalent eigenstrain of the interconnected voids was obtained from approximation. It is known that Mori-Tanaka's scheme is first derived from closed cell and dilute inclusion/inhomogeneity case, while the derived "equivalent eigenstrain" of the interconnected voids is an effective method to obtain the material property of open cell structures, discrepancy might be introduced in the extension of the original model.

5.2 Analytical and Numerical Results for Effective Shear Moduli

Besides effective moduli in normal direction, effective shear moduli for each configuration were obtained through analytical and numerical model. In Section 5.2.1, the analytical and numerical modeling results of effective shear moduli are presented. A discussion is provided in Section 5.2.2.

5.2.1 Effective Shear Moduli from Analytical and Numerical Model

As mention above, the specimens for each configuration were designed as pseudo-transversely isotropic material, thus $G_{31} = G_{32} \neq G_{12}$, where Direction 3 is the layer build-up direction, and Directions 1 and 2 are perpendicular to Direction 3. In numerical simulations, effective shear moduli of G_{31} and G_{12} for each configuration were obtained. Taking Configuration 7 as an example, Figure 5.8 demonstrates the section view of stress contour of RVE for graded open cell structure with round disk voids subjected to pure shear stress σ_{12}. The porosity is gradually becoming higher along +z direction (from left to right in Figure 5.8). It is observed that with a higher porosity, the stress σ_{12} is lower, indicating lower shear stress for higher porosity layers. The stress level is highest near the round disk void, while lower when further away from the void.

The effective modulus was obtained by the volume average stress divided by volume average strain.

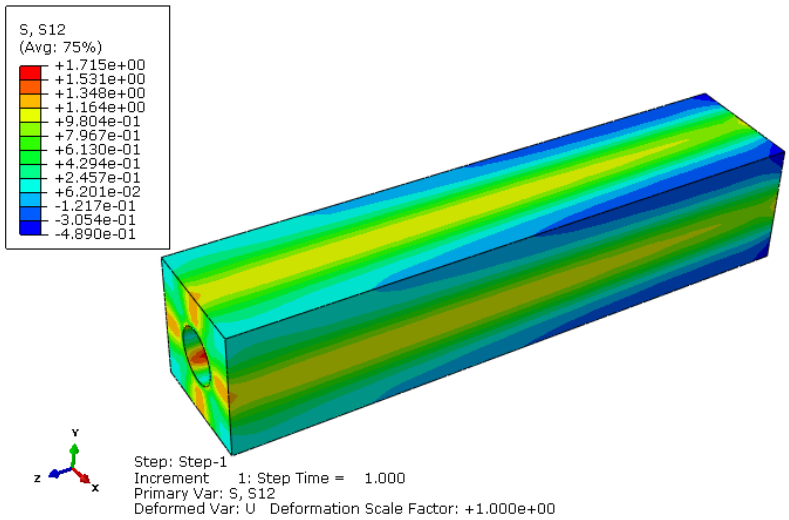

Figure 5. 8 Stress contour plot of σ_{12} for graded open cell structure with round disk voids

Tables 5.8-5.11 show the comparison of effective shear moduli from numerical and analytical results for each configuration. The normalized effective shear modulus is defined as the effective shear modulus divided by shear modulus of base material (in this case, it is 368 MPa), where the normalized effective shear modulus falls in the range of (0, 1]. It is observed that a good agreement was achieved between numerical and analytical results, indicating that the analytical model can predict the shear behavior of FGPMs with good accuracy.

Table 5. 8 Comparison of numerical and analytical results of normalized effective shear moduli for closed cell round disk

	Round disk_constant_closed cell			Round disk_graded_closed cell		
	Numerical	Analytical	Discrepancy with Numerical	Numerical	Analytical	Discrepancy with Numerical
G31	0.543	0.588	8.325%	0.524	0.578	10.321%
G12	0.620	0.657	5.987%	0.568	0.610	7.385%

Table 5. 9 Comparison of numerical and analytical results of normalized effective shear moduli for closed cell square disk

	Square disk_constant_closed cell			Square disk_graded_closed cell		
	Numerical	Analytical	Discrepancy with Numerical	Numerical	Analytical	Discrepancy with Numerical
G31	0.556	0.622	11.762%	0.524	0.574	9.513%
G12	0.704	0.764	8.557%	0.655	0.691	5.421%

Table 5. 10 Comparison of numerical and analytical results of normalized effective shear moduli for open cell round disk

	Round disk_constant_open cell			Round disk_graded_open cell		
	Numerical	Analytical	Discrepancy with Numerical	Numerical	Analytical	Discrepancy with Numerical
G31	0.467	0.512	9.697%	0.484	0.538	11.300%
G12	0.541	0.581	7.493%	0.437	0.477	9.223%

Table 5. 11 Comparison of numerical and analytical results of normalized effective shear moduli for open cell square disk

	Square disk_constant_open cell			Square disk_graded_open cell		
	Numerical	Analytical	Discrepancy with Numerical	Numerical	Analytical	Discrepancy with Numerical
G31	0.331	0.363	9.648%	0.487	0.542	11.382%
G12	0.521	0.563	8.080%	0.380	0.403	6.103%

5.2.2 Discussions

It can be observed from Tables 5.8-5.11 that prediction discrepancy between analytical and numerical model for G31 is higher than G12. Since Direction 3 is the layer build-up direction and the geometry along Direction 3 is more complicated than

that along Directions 1 and 2, it might be difficult for the analytical model to capture all the geometrical information, i.e. the location of each void. Thus, it might lead to a higher discrepancy for G31.

Comparing the discrepancy between analytical model and numerical model for effective shear moduli (Tables 5.8-5.11) to that of effective Young's moduli (Tables 5.3-5.6), it is observed that overall, the former is larger than the latter. This could be partially due to that, unlike Young's modulus E_{33} and E_{11}, the geometries of the structures, i.e. the location of voids and the porosity distribution have significant effects on the shear property of the material. Since the analytical model might not be able to capture the location information of voids, it is understandable that a larger discrepancy in predicting effective shear moduli was found compared to that in effective Young's moduli.

6. CONCLUSIONS AND FUTURE WORK

6.1 Conclusions

The fabrication of porous material received great attention. This work developed a new technique to use the thermo-bonding lamination process to fabricate porous material. In this approach, the single layers were first fabricated and then bonded by polymer self-adhesion using a heating and compression machine. The technique is capable of creating both open cell and closed cell structures. The approach is convenient, efficient, and cost-effective. The factors which influence the bonding shear strength was investigated. It was also demonstrated that the bonding shear strength can be controlled by properly setting the heating temperature, applied pressure, and processing time.

Analytical models were derived for FGPM in order to better understand its material behavior and predict the mechanical response under different loading conditions. A generalization of Mori-Tanaka's method to model "porous" and "graded" material was derived and implemented for the FGPMs. In addition, a model deals with open cell structure was developed, and an analytical solution to the overall eigenstrain of interconnected voids were provided by considering the disturbed stress field outside of

the voids. The models can accurately predict the mechanical response of open cell and closed cell FGPMs.

Numerical model based on RVE with periodic boundary condition was developed for FGPMs material in order to investigate the mechanical behavior of the material and to obtain the effective modulus. It has been shown that the numerical model can predict the material response accurately.

In conclusion, this research demonstrated the feasibility of using the thermo-bonding lamination approach to fabricate functionally graded porous material structures. The research also resulted in analytical models and numerical techniques to accurately predict the mechanical behavior of developed materials.

6.2 Future Work

While this work has achieved the research objectives of developing a feasible approach to fabricate FGPMs, a powerful analytical model and numerical model to predict their mechanical properties, the following future work is suggested to further advance the knowledge in the field:

In the area of FGPM fabrication, the future work includes developing a direct relationship for the heating temperature, holding time, and applied pressure to bonding

strength; shortening the processing time to improve the efficiency; and applying this method to real industrial production.

In the area of analytical modeling, the future work includes implementing different FGPMs with different geometry and size of pores and different material property into the proposed models. The applicability of the methodology presented here in the condition of polygon void remains to be investigated. One challenge here is that the disturbed stress field outside irregular polygon voids embedded in anisotropic material might be necessary have analytical solution, therefore, other alternative solution method needs to be figure out.

In the area of numerical modeling, the future work including: (1) to investigate that under the same porosity gradient level, how the geometry of pores (in terms of the number of pores, and the shape and size of pores) will affect the material properties such stiffness, and damping property; (2) for the FGPMs with the same overall porosity, the effects of porosity distribution over the volume (e.g. discrete distribution, linear distribution, non-linear distribution) on the overall material property will be investigated.

The developed FGPMs can potentially be used as mechanical filter, damping material, bone scaffold, and core of the sandwich panel. Future work will also include the evaluation of the requirements for such applications.

REFERENCES

[1] V. Birman, L.W. Byrd, Modeling and Analysis of Functionally Graded Materials and Structures, Applied Mechanics Reviews, 60 (2007) 195.

[2] A.J. Markworth, K.S. Ramesh, W.P. Parks, Jr., Modelling studies applied to functionally graded materials, Journal of Materials Science, 30 (1995) 2183-2193.

[3] Z. Wang, C.Y. Tang, C.P. Tsui, B. Gao, Optimization Design for Graded Porous Tubular Structures, Journal of the Serbian Society for Computational Mechanics, 2 (2008) 89-90.

[4] S.J. Hollister, J.M. Brennan, N. Kikuchi, A homogenization sampling procedure for calculating trabecular bone effective stiffness and tissue level stress, Journal of Biomechanics, 27 (1994) 433-444.

[5] E.C.N. Silva, M.C. Walters, G.H. Paulino, Modeling bamboo as a functionally graded material: lessons for the analysis of affordable materials, Journal of Materials Science, 41 (2006) 6991-7004.

[6] N. Oxman, S. Keating, E. Tsai, Functionally graded rapid prototyping, in: Innovative Developments in Virtual and Physical Prototyping: Proceedings of the 5th International Conference on Advanced Research in Virtual and Rapid Prototyping, 2011, pp. 483-490.

[7] M. Ali, A. Qamhiyah, D. Flugrad, M. Shakoor, Theoretical and finite element study of a compact energy absorber, Advances in Engineering Software, 39 (2008) 95-106.

[8] P.Y. Chen, A.Y. Lin, Y.S. Lin, Y. Seki, A.G. Stokes, J. Peyras, E.A. Olevsky, M.A. Meyers, J. McKittrick, Structure and mechanical properties of selected biological materials, Journal of the mechanical behavior of biomedical materials, 1 (2008) 208-226.

[9] M. Thieme, K.P. Wieters, F. Bergner, D. Scharnweber, H. Worch, J. Ndop, T.J. Kim, W. Grill, Titanium powder sintering for preparation of a porous functionally graded material destined for orthopaedic implants, Journal of materials science. Materials in medicine, 12 (2001) 225-231.

[10] S.J. Kalita, S. Bose, H.L. Hosick, A. Bandyopadhyay, Development of controlled porosity polymer-ceramic composite scaffolds via fused deposition modeling, Materials Science and Engineering: C, 23 (2003) 611-620.

[11] L. Cui, S. Kiernan, M.D. Gilchrist, Designing the energy absorption capacity of functionally graded foam materials, Materials Science and Engineering: A, 507 (2009) 215-225.

[12] K.F. Leong, K.K. Phua, C.K. Chua, Z.H. Du, K.O. Teo, Fabrication of porous polymeric matrix drug delivery devices using the selective laser sintering techniques, Proc Instn Mech Engrs, 215 (2001) 191-201.

[13] I.-H. Oh, N. Nomura, N. Masahashi, S. Hanada, Mechanical properties of porous titanium compacts prepared by powder sintering, Scripta Materialia, 49 (2003) 1197-1202.

[14] M. Bram, C. Stiller, H.P. Buchkremer, D. Stöver, H. Baur, High-Porosity Titanium, Stainless Steel, and Superalloy Parts, Advanced Engineering Materials, 2 (2000) 196-199.

[15] J. Guan, K.L. Fujimoto, M.S. Sacks, W.R. Wagner, Preparation and characterization of highly porous, biodegradable polyurethane scaffolds for soft tissue applications, Biomaterials, 26 (2005) 3961-3971.

[16] K. Okazaki, W.H. Lee, D.K. Kim, R.A. Kopczyk, Physical characteristics of Ti-6Al-4V implants fabricated by electrodischarge compaction, Journal of Biomedical Materials Research, 25 (1991) 1417-1429.

[17] G. Ryan, A. Pandit, D.P. Apatsidis, Fabrication methods of porous metals for use in orthopaedic applications, Biomaterials, 27 (2006) 2651-2670.

[18] J. Banhart, Manufacturing routes for metallic foams, Jom-J Min Met Mat S, 52 (2000) 22-27.

[19] A.G. Mikos, A.J. Thorsen, L.A. Czerwonka, Y. Bao, R. Langer, D.N. Winslow, J.P. Vacanti, Preparation and characterization of poly(l-lactic acid) foams, Polymer, 35 (1994) 1068-1077.

[20] W.L. Murphy, R.G. Dennis, J.L. Kileny, D.J. Mooney, Salt fusion: An approach to improve pore interconnectivity within tissue engineering scaffolds, Tissue Eng, 8 (2002) 43-52.

[21] Y.S. Nam, T.G. Park, Biodegradable polymeric microcellular foams by modified thermally induced phase separation method, Biomaterials, 20 (1999) 1783-1790.

[22] D.J.Mooney, D.F. Baldwin, N.P. Suh, J.P. Vacanti, R. Langer, Novel approach to fabricate porous sponge of poly (D.L- lactic-co-glycolic acid) without the use of organica solvents, Biomaterials, 17 (1996) 1417-1422.

[23] X. Wang, W. Li, V. Kumar, A method for solvent-free fabrication of porous polymer using solid-state foaming and ultrasound for tissue engineering applications, Biomaterials, 27 (2006) 1924-1929.

[24] L. Zhu, Y. Wang, X. Yu, X. Shen, X. Xu, Controllable fabrication of graded and gradient porous polypropylene, Journal of Porous Materials, 22 (2014) 119-125.

[25] L. Podshivalov, C.M. Gomes, A. Zocca, J. Guenster, P. Bar-Yoseph, A. Fischer, Design, Analysis and Additive Manufacturing of Porous Structures for Biocompatible Micro-Scale Scaffolds, Procedia CIRP, 5 (2013) 247-252.

[26] Y.A. Jande, M. Erdal, S. Dag, Production of graded porous polyamide structures and polyamide-epoxy composites via selective laser sintering, Journal of Reinforced Plastics and Composites, 33 (2014) 1017-1036.

[27] M.A.K. Liebschner, M.A. Wettergreen, Optimization of bone scaffold engineering for load bearing applications, Topics in Tissue Engineering, Chapter 6 (2003).

[28] K. Yu, A. Ritchie, Y. Mao, M.L. Dunn, H.J. Qi, Controlled Sequential Shape Changing Components by 3D Printing of Shape Memory Polymer Multimaterials, Procedia IUTAM, 12 (2015) 193-203.

[29] M.C. Leu, L. Tang, B. Deuser, R.G. Landers, G.E. Hilmas, S.Zhang, J. Watts, Freeze form extrusion fabrication of composite structure, SFF Symposium, (2011) 111-124.

[30] E. Barnett, C. Gosselin, Weak Support Material Techniques For Alternative Additive Manufacturing Materials, Additive Manufacturing, (2015).

[31] 3D Printing Safety. http://www.cmu.edu/ehs/fact-sheets/3D-Printing-Safety.pdf; 2012 [access Jan 28, 2016].

[32] T. Himmer, T. Nakagawa, M. Anzai, Lamination of metal sheets, Comput Ind, 39 (1999) 27-33.

[33] T. Himmer, A. Techel, S. Nowotny, E. Beyer, Recent developments in metal laminated tooling by multiple laser processing, Rapid Prototyping J, 9 (2003) 24-29.

[34] B. Bahadur, J.D. Sampica, J.L. Tchon, A. Butterfield, Direct dry film optical bonding - A low-cost, robust, and scalable display lamination technology, Journal of the Society for Information Display, 19 (2011) 732.

[35] K. Singha, A Review on Coating & Lamination in Textiles: Processes and Applications, American Journal of Polymer Science, 2 (2012) 39-49.

[36] C.S. Tan, R.J. Gutmann, L.R. Reif, Wafer leverl 3-D ICs process technology.

[37] T. Shimatsu, M. Uomoto, Atomic diffusion bonding of wafers with thin nanocrystalline metal films, Journal of Vacuum Science & Technology B: Microelectronics and Nanometer Structures, 28 (2010) 706.

[38] M.G. Kamath, A. Dahiya, R.R. Hegde, Thermal bonding of nonwoven fabrics, (2004).

[39] C.-W. Tsao, D.L. DeVoe, Bonding of thermoplastic polymer microfluidics, Microfluidics and Nanofluidics, 6 (2008) 1-16.

[40] Y. Sun, Y.C. Kwok, N.-T. Nguyen, Low-pressure, high-temperature thermal bonding of polymeric microfluidic devices and their applications for electrophoretic separation, Journal of Micromechanics and Microengineering, 16 (2006) 1681-1688.

[41] M. Vaezi, S. Chianrabutra, B. Mellor, S. Yang, Multiple material additive manufacturing – Part 1: a review, Virtual and Physical Prototyping, 8 (2013) 19-50.

[42] H. Windsheimer, N. Travitzky, A. Hofenauer, P. Greil, Laminated Object Manufacturing of Preceramic-Paper-Derived Si?SiC Composites, Advanced Materials, 19 (2007) 4515-4519.

[43] S.J. Rodrigues, Solid freeform fabrication of functional silicon nitride ceramics by laminated object manufacturing, SFF Symposium, (2000).

[44] Mcortechnologies. How 3D Paper Printing Works: Printing the Prototype, http://mcortechnologies.com/how-selective-deposition-lamination-sdl-3d-paper-printing-and-rapid-prototyping-technology-works-part-2-of-3-printing-the-prototype-blog/, 2015 [accessed August 28,2015].

[45] S.S. Voyutskii, V.L. Vakula, the role of diffusion phenomena in polymer to polymer adhesion, Journal of Applied Polymer Science, 7 (1963) 475–491.

[46] H.H. Kausch, M. Tirrell, Polymer interdiffusion, Annual Review of Materials Science, 19 (1989) 341–377.

[47] S. Prager, The healing process at polymer–polymer interfaces, The Journal of Chemical Physics, 75 (1981) 5194.

[48] N. Padhye, D.M. Parks, B.L. Trout, A.H. Slocum, A new phenomenon sub Tg, solid state plasticity induced bonding in polymers, arXiv:1506.06106 [cond-mat.soft], (2015).

[49] J.R. Zuiker, Functionally graded materials: Choice of micromechanics model and limitations in property variation, Composites Engineering, 5 (1995) 807-819.

[50] T. Reiter, G.J. Dvorak, V. Tvergaard, Micromechanical models for graded composite materials, Journal of the Mechanics and Physics of Solids, 45 (1997) 1281-1302.

[51] R.M. Christensen, A critical evaluation for a class of micro-mechanics models, Journal of the Mechanics and Physics of Solids, 38 (1990) 379-404.

[52] I.E. Reimanis, Functionally Graded Materials, in: Handbook of Advanced Materials, John Wiley & Sons, Inc., 2004, pp. 465-486.

[53] G. Udupa, S.S. Rao, K.V. Gangadharan, Functionally Graded Composite Materials: An Overview, Procedia Materials Science, 5 (2014) 1291-1299.

[54] I.M. Fedorchenko, A.V. Nenakhov, I.I. Beloborodov, Sintering and some properties of porous materials from granulated bronze powder, Soviet Powder Metallurgy and Metal Ceramics, 15 724-726.

[55] K. Asaoka, N. Kuwayama, O. Okuno, I. Miura, Mechanical properties and biomechanical compatibility of porous titanium for dental implants, Journal of Biomedical Materials Research, 19 (1985) 699-713.

[56] A.J. Clemow, A.M. Weinstein, J.J. Klawitter, J. Koeneman, J. Anderson, Interface mechanics of porous titanium implants, J Biomed Mater Res, 15 (1981) 73-82.

[57] Z. Wally, W. van Grunsven, F. Claeyssens, R. Goodall, G. Reilly, Porous Titanium for Dental Implant Applications, Metals, 5 (2015) 1902.

[58] A. Greco, A. Maffezzoli, Polymer melting and polymer powder sintering by thermal analysis, Journal of Thermal Analysis and Calorimetry, 72 1167-1174.

[59] S.D. Cook, K.A. Walsh, R.J. Haddad, Jr., Interface mechanics and bone growth into porous Co-Cr-Mo alloy implants, Clinical orthopaedics and related research, (1985) 271-280.

[60] J.R. Dabrowski, Use of powder metallurgy for development of implants of Co-Cr-Mo alloy powder, Biomedizinische Technik. Biomedical engineering, 46 (2001) 106-108.

[61] P.J. Nugent, R.J. Crawford, L. Xu, Computer prediction of cycle times during rotational molding of plastics, Advances in Polymer Technology, 11 (1992) 181-191.

[62] M. Kontopoulou, M. Bisaria, J. Vlachopoulos, An Experimental Study of Rotational Molding of Polypropylene/Polyethylene Copolymers, International Polymer Processing, 12 (1997) 165-173.

[63] M. Spencer, Rotational Molding of Acrylonitrile-Butadiene-Styrene Polymers and blends, Phd. dissertation, Brigham Young University, (2003).

[64] J.M. Martell, R.H. Pierson, 3rd, J.J. Jacobs, A.G. Rosenberg, M. Maley, J.O. Galante, Primary total hip reconstruction with a titanium fiber-coated prosthesis inserted without cement, The Journal of bone and joint surgery. American volume, 75 (1993) 554-571.

[65] J.P. Li, S.H. Li, K.d. Groot, P. Layrolle, Preparation and Characterization of Porous Titanium, Key Engineering Materials, 218-220 (2002) 51-54.

[66] S. Deville, Freeze-Casting of Porous Biomaterials: Structure, Properties and Opportunities, Materials, 3 (2010) 1913.

[67] S. Deville, Freeze-Casting of Porous Ceramics: A Review of Current Achievements and Issues, Advanced Engineering Materials, 10 (2008) 155-169.

[68] H. Hahn, W. Palich, Preliminary evaluation of porous metal surfaced titanium for orthopedic implants, Journal of Biomedical Materials Research, 4 (1970) 571-577.

[69] X. Zhang, R.A. Ayers, K. Thorne, J.J. Moore, F. Schowengerdt, Combustion synthesis of porous materials for bone replacement, Biomedical sciences instrumentation, 37 (2001) 463-468.

[70] V. Shapovalov, L. Boyko, Gasar—A new Class of Porous Materials, Advanced Engineering Materials, 6 (2004) 407-410.

[71] V.I. Shapovalov, J.C. Withers, Hydrogen Technology for Porous Metals (Gasars) Production, in: B. Baranowski, S.Y. Zaginaichenko, D.V. Schur, V.V. Skorokhod, A. Veziroglu (Eds.) Carbon Nanomaterials in Clean Energy Hydrogen Systems, Springer Netherlands, Dordrecht, 2008, pp. 29-51.

[72] S. Berro, R. El Ahdab, H. Hajj Hassan, H.M. Khachfe, M. Hajj-Hassan, From Plastic to Silicone: The Novelties in Porous Polymer Fabrications, Journal of Nanomaterials, 2015 (2015) 21.

[73] H. Janik, M. Marzec, A review: Fabrication of porous polyurethane scaffolds, Materials Science and Engineering: C, 48 (2015) 586-591.

[74] T.-H. Young, L.-P. Cheng, D.-J. Lin, L. Fane, W.-Y. Chuang, Mechanisms of PVDF membrane formation by immersion-precipitation in soft (1-octanol) and harsh (water) nonsolvents, Polymer, 40 (1999) 5315-5323.

[75] M. Di Luccio, R. Nobrega, C.P. Borges, Microporous anisotropic phase inversion membranes from bisphenol-A polycarbonate: study of a ternary system, Polymer, 41 (2000) 4309-4315.

[76] N. Zhu, X. Chen, Biofabrication of Tissue Scaffolds, 2013.

[77] S. Grenier, M. Sandig, K. Mequanint, Polyurethane biomaterials for fabricating 3D porous scaffolds and supporting vascular cells, Journal of biomedical materials research. Part A, 82 (2007) 802-809.

[78] L. Draghi, S. Resta, M.G. Pirozzolo, M.C. Tanzi, Microspheres leaching for scaffold porosity control, Journal of materials science. Materials in medicine, 16 (2005) 1093-1097.

[79] 3D printing. https://en.wikipedia.org/wiki/3D_printing; 2016 [access April 24, 2016].

[80] C.-H. Chen, J.-P. Chen, M.-Y. Lee, Effects of gelatin modification on rapid prototyping PCL scaffolds for cartilage engineering, Journal of Mechanics in Medicine and Biology, 11 (2011) 993-1002.

[81] J.M. Williams, A. Adewunmi, R.M. Schek, C.L. Flanagan, P.H. Krebsbach, S.E. Feinberg, S.J. Hollister, S. Das, Bone tissue engineering using polycaprolactone scaffolds fabricated via selective laser sintering, Biomaterials, 26 (2005) 4817-4827.

[82] R.D. Goodridge, C.J. Tuck, R.J.M. Hague, Laser sintering of polyamides and other polymers, Progress in Materials Science, 57 (2012) 229-267.

[83] J.-P. Kruth, Consolidation of Polymer Powders by Selective Laser Sintering, 3rd International Conference PMI2008, (2008) 1-16.

[84] F.P.W. Melchels, J. Feijen, D.W. Grijpma, A review on stereolithography and its applications in biomedical engineering, Biomaterials, 31 (2010) 6121-6130.

[85] H. Lin, D. Zhang, P.G. Alexander, G. Yang, J. Tan, A.W. Cheng, R.S. Tuan, Application of visible light-based projection stereolithography for live cell-scaffold fabrication with designed architecture, Biomaterials, 34 (2013) 331-339.

[86] R. Sodian, M. Loebe, A. Hein, D.P. Martin, S.P. Hoerstrup, E.V. Potapov, H. Hausmann, T. Lueth, R. Hetzer, Application of stereolithography for scaffold fabrication for tissue engineered heart valves, ASAIO journal (American Society for Artificial Internal Organs : 1992), 48 (2002) 12-16.

[87] Y. Yu, Y. Zhang, I.T. Ozbolat, A Hybrid Bioprinting Approach for Scale-Up Tissue Fabrication, Journal of Manufacturing Science and Engineering, 136 (2014) 061013-061013.

[88] Selective laser sintering. https://en.wikipedia.org/wiki/Selective_laser_sintering; 2016, [accessed May 12, 2016].

[89] Stereolithography. https://en.wikipedia.org/wiki/Stereolithography; 2016, [accessed May 12, 2016].

[90] Fused deposition modeling, https://en.wikipedia.org/wiki/Fused_deposition_modeling, 2016, [accessed May 12, 2016].

[91] J. Parthasarathy, B. Starly, S. Raman, A design for the additive manufacture of functionally graded porous structures with tailored mechanical properties for biomedical applications, Journal of Manufacturing Processes, 13 (2011) 160-170.

[92] Adhesive and sealants. Water-based adhesives, http://www.adhesives.org/adhesives-sealants/adhesives-sealants-overview/adhesive-technologies/physically-hardening/water-based-adhesives; 2012 [accessed June 1, 2016].

[93] Adhesive and sealants. Physically hardening; http://www.adhesives.org/adhesives-sealants/adhesives-sealants-overview/adhesive-technologies/physically-hardening#hot; 2012, [accessed June 1, 2016].

[94] K.V. Wong, A. Hernandez, A Review of Additive Manufacturing, ISRN Mechanical Engineering, 2012 (2012) 10.

[95] C.G.J. Daufenbach, S. McMillin, Solid freeform fabrication of functional ceramic components using a laminated object manufacturing technique, Solid Freeform Fabrication, (1994) 17.

[96] M. Fahad, P. Dickens, M. Gilbert, Novel polymeric support materials for jetting based additive manufacturing processes, Rapid Prototyping J, 19 (2013) 230-239.

[97] B. Mueller, D. Kochan, Laminated object manufacturing for rapid tooling and patternmaking in foundry industry, Comput Ind, 39 (1999) 47-53.

[98] F.O. Sonmez, H.T. Hahn, Thermomechanical analysis of the laminated object manufacturing (LOM) process, Rapid Prototyping J, 4 (1998) 26-36.

[99] B.K. Paul, V. Voorakarnam, Effect of Layer Thickness and Orientation Angle on Surface Roughness in Laminated Object Manufacturing, Journal of Manufacturing Processes, 3 (2001) 94-101.

[100] Laminated object manufacturing, https://en.wikipedia.org/wiki/Laminated_object_manufacturing, 2016, [accessed June 1, 2016].

[101] S. Nemat-Nasser, M. Hori, Micromechanics Overall Properties of Heterogeneous Materials, North Holland, (1999).

[102] W. Voigt, Theoretische Studien über die Elasticitätsverhältnisse der Krystalle, 1887.

[103] A. Reuss, Berechnung der Fließgrenze von Mischkristallen auf Grund der Plastizitätsbedingung für Einkristalle, Journal of Applied Mathematics and Mechanics, 9 (1929) 49-58.

[104] Z. Hashin, On elastic behaviour of fibre reinforced materials of arbitrary transverse phase geometry, Journal of the Mechanics and Physics of Solids, 13 (1965) 119-134.

[105] Z. Hashin, The Elastic Moduli of Heterogeneous Materials, Journal of Applied Mechanics, 29 (1962) 143-150.

[106] J.D. Eshelby, The Determination of the Elastic Field of an Ellipsoidal Inclusion, and Related Problems, Proceedings of the Royal Society of London A: Mathematical, Physical and Engineering Sciences, 241 (1957) 376-396.

[107] R. Hill, A self-consistent mechanics of composite materials, Journal of the Mechanics and Physics of Solids, 13 (1965) 213-222.

[108] B. Budiansky, On the elastic moduli of some heterogeneous materials, Journal of the Mechanics and Physics of Solids, 13 (1965) 223-227.

[109] R.M. Christensen, K.H. Lo, Solutions for effective shear properties in three phase sphere and cylinder models, Journal of the Mechanics and Physics of Solids, 27 (1979) 315-330.

[110] M.L. Accorsi, S. Nemat-Nasser, Bounds on the overall elastic and instantaneous elastoplastic moduli of periodic composites, Mechanics of Materials, 5 (1986) 209-220.

[111] S. Nemat-Nasser, T. Iwakuma, M. Hejazi, On composites with periodic structure, Mechanics of Materials, 1 (1982) 239-267.

[112] T. Mori, K. Tanaka, Average stress in matrix and average elastic energy of materials with misfitting inclusions, Acta Metallurgica, 21 (1973) 571-574.

[113] Y. Benveniste, A new approach to the application of Mori-Tanaka's theory in composite materials, Mechanics of Materials, 6 (1987) 147-157.

[114] C.C. Chamis, Mechanics of composite materials past present and future, Journal of Composite Technology, 11 (1989) 3-14.

[115] J.C. Halpin, J.L. Kardos, The Halpin-Tsai Equations a review, Polymer Engineering and Science 16 (1976).

[116] G.W. Milton, Correlation of the electromagnetic and elastic properties of composites and microgeometries corresponding with effective medium approximations, AIP Conference Proceedings, 107 (1984) 66-77.

[117] A.N. Norris, A differential scheme for the effective moduli of composites, Mechanics of Materials, 4 (1985) 1-16.

[118] M. Nemat-Alla, Reduction of thermal stresses by developing two-dimensional functionally graded materials, International Journal of Solids and Structures, 40 (2003) 7339-7356.

[119] J.N. Reddy, Thermo-mechanical behavior of functionally graded materials, Final report for AFOSR Grant, (1998).

[120] T. Reiter, G.J. Dvorak, Micromechanical models for graded composite materials : ii. thermomechanical loading, Journal of the Mechanics and Physics of Solids, 46 (1998) 1655-1673.

[121] R. Pal, New models for effective Young's modulus of particulate composites, Composites Part B: Engineering, 36 (2005) 513-523.

[122] J. Zuiker, G. Dvorak, The effective properties of functionally graded composites—I. Extension of the mori-tanaka method to linearly varying fields, Composites Engineering, 4 (1994) 19-35.

[123] Y.H. Zhao, G.P. Tandon, G.J. Weng, Elastic-Moduli for a Class of Porous Materials, Acta Mech, 76 (1989) 105-130.

[124] Y.H. Zhao, G.J. Weng, Effective Elastic Moduli of Ribbon-Reinforced Composites, Journal of Applied Mechanics, 57 (1990) 158-167.

[125] R.W. Zimmerman, Compressibility of Two-Dimensional Cavities of Various Shapes, Journal of Applied Mechanics, 53 (1986) 500-504.

[126] J.B. Walsh, W.F. Brace, A.W. England, Effect of Porosity on Compressibility of Glass, Journal of the American Ceramic Society, 48 (1965) 605-608.

[127] M. Kachanov, I. Tsukrov, B. Shafiro, Effective Moduli of Solids With Cavities of Various Shapes, Applied Mechanics Reviews, 47 (1994) S151-S174.

[128] Y. Benveniste, On the Mori-Tanaka's method in cracked bodies, Mechanics Research Communications, 13 (1986) 193-201.

[129] I. Babuška, Solution of Interface Problems by Homogenization. I, SIAM Journal on Mathematical Analysis, 7 (1976) 603-634.

[130] J. Keller, Effective Behavior of Heterogeneous Media, in: U. Landman (Ed.) Statistical Mechanics and Statistical Methods in Theory and Application, Springer US, 1977, pp. 631-644.

[131] J.L. Lions, Asymptotic expansions in perforated media with a periodic structure, (1980) 125-140.

[132] S.J. Hollister, N. Kikuchi, A comparison of homogenization and standard mechanics analyses for periodic porous composites, Computational Mechanics, 10 (1992) 73-95.

[133] J. Aboudi, Generalized effective stiffness theory for the modeling of fiber-reinforced composites, International Journal of Solids and Structures, 17 (1981) 1005-1018.

[134] J. Aboudi, Micromechanical analysis of thermo-inelastic multiphase short-fiber composites, Composites Engineering, 5 (1995) 839-850.

[135] J.R. Cho, D.Y. Ha, Averaging and finite-element discretization approaches in the numerical analysis of functionally graded materials, Materials Science and Engineering: A, 302 (2001) 187-196.

[136] X.Y. Kou, S.T. Tan, A simple and effective geometric representation for irregular porous structure modeling, Computer-Aided Design, 42 (2010) 930-941.

[137] A. Ajdari, P. Canavan, H. Nayeb-Hashemi, G. Warner, Mechanical properties of functionally graded 2-D cellular structures: A finite element simulation, Materials Science and Engineering: A, 499 (2009) 434-439.

[138] V. Kouznetsova, M.W.A. Brekelmans, T.F.P. Baaijens, An approach to micro-macro modeling of heterogeneous materials, Computational Mechanics, 27 37-48.

[139] M. Kulkarni, Finite element analysis of 2-D representative volume element, Master's report, Michigan Technological University, 2012., (2012).

[140] Loctite products. Loctite super glue, http://www.loctiteproducts.com/super-glue.shtml; 2015 [accessed June 1, 2016].

[141] Y. Zhang, M.S. Mamadapur, J. Wang, Constitutive modelling for fused deposition modelling of acrylonitrile butadiene styrene (ABS) under elastic response, International Journal of Rapid Manufacturing, 5 (2015) 76-94.

[142] W.C.a.D.B. Chris Weinberger, Lecture Notes – Elasticity of Microscopic Structures, (2005).

[143] R. Hill, Elastic properties of reinforced solids: Some theoretical principles, Journal of the Mechanics and Physics of Solids, 11 (1963) 357-372.

[144] J. Aboudi, S.M. Arnold, B.A. Bednarcyk, Chapter 2 - Constituent Material Modeling, in: Micromechanics of Composite Materials, Butterworth-Heinemann, Oxford, 2013, pp. 19-85.

[145] Y. Zhao, M. Taya, Analytical Modeling for Stress-Strain Curve of a Porous NiTi, Journal of Applied Mechanics, 74 (2006) 291-297.

[146] T. Mura, Micromechanics of defects in solids, Springer Science & Business Media, (1982).

[147] Y.P. Chiu, On the Stress Field Due to Initial Strains in a Cuboid Surrounded by an Infinite Elastic Space, Journal of Applied Mechanics, 44 (1977) 587-590.

[148] R.J. Asaro, D.M. Barnett, The non-uniform transformation strain problem for an anisotropic ellipsoidal inclusion, Journal of the Mechanics and Physics of Solids, 23 (1975) 77-83.

[149] C.T. Sun, R.S. Vaidya, Prediction of composite properties from a representative volume element, Composites Science and Technology, 56 (1996) 171-179.

[150] S. Li, Boundary conditions for unit cells from periodic microstructures and their implications, Composites Science and Technology, 68 (2008) 1962-1974.